Analysis of interactions in donor-acceptor compounds and their application in organic light-emitting diodes (OLEDs)

Departament of Physical Chemistry and Technology of Polymers
Faculty of Chemistry
Silesian University of Technology

Ph.D. Student: M.Sc. Nícolas Oliveira Decarli
Supervisor: Prof. dr hab. inż. Przemysław Data
Co-supervisor: Dr inż. Piotr Pander

Contents

TABLE LIST

FIGURES LIST

List of Abbreviations:

AIE – Aggregation-induced emission

AIEE – Aggregation-induced emission enhancement or Aggregation-induced enhanced emission

DF – Delayed fluorescence

EA – Electron affinity

EBL – Electron blocking layer

EIL – Electron injection layer

EML – Emissive layer

EQE – External quantum efficiency

ETL – Electron transport layer

HBL – Hole blocking layer

HIL – Hole injection layer

HTL – Hole transport layer

HOMO – Highest occupied molecular orbital

IP – Ionization potential

IQE – Internal quantum efficiency

ISC – intersystem crossing

ITO – Indium-tin oxide

LUMO – Lowest unoccupied molecular orbital

OLED – Organic light-emitting diodes

PF – Prompt fluorescence

PLQY – Photoluminescence quantum yield

RISC – Reverse intersystem crossing

RTP – Room temperature phosphorescence

S_0 – Singlet ground state

S_1 – Singlet first excited state

SOC – Spin-orbital coupling

T_1 – Triplet first excited state

TADF – Thermally activated delayed fluorescence

ΔE_{ST} – Difference between energies of S_1 and T_1

List of Publications:

1. W. P. Silva, **<u>N. O. Decarli</u>**, L. Espíndola, K. Erfurt, A. Blacha-Grzechnik, P. Pander, M. Lapkowski and P. Data “Multifunctional Properties of D-A Luminophores Based on Acenaphtopyrido[2,3-b]pyrazine Core: Photophysics, Photochemistry, and Efficient Solution-Processed OLEDs.” *J Mater Chem C.* **2023,** 1, 3777. **doi:10.1039/D3TC02860G**

2. P. P. Abatti, **<u>N. O. Decarli</u>**, S. Gogoc, P. Data, I. H. Bechtold, E. Westphal and H. Gallardo. “Shedding Light on Highly Emissive 1,4-Dihydropyrrolo[3,2-b]pyrrole Derivatives: Synthesis and Aggregate-Dependent Emission.” *Chempluschem*, **2023**, e202300539. **doi:10.1002/cplu.202300539**

3. T. Hosono, **<u>N. O. Decarli</u>**, P. Z. Crocomo, T. Goya, L. E. de Sousa, N. Tohnai, S. Minakata, P. de Silva, P. Data and Y. Takeda. “The regioisomeric effect on the excited-state fate leading to room-temperature phosphorescence or thermally activated delayed fluorescence in a dibenzophenazine-cored donor-acceptor-donor system.” *J. Mater. Chem. C*, **2022**,10, 4905-4913 **doi:10.1039/d1tc05730h**

4. **<u>N. O. Decarli</u>**, E. Zapp, B. S. de Souza, E. R. Santana, J. P. Winiarski and I. C. Vieira. “Biosensor based on laccase-halloysite nanotube and imidazolium zwitterionic surfactant for dopamine determination.” *Biochem Eng J.,* **2022**, 186, 108565. **doi:10.1016/j.bej.2022.108565**

5. S. Goto, Y. Nitta, **<u>N. O. Decarli</u>**, L. E. de Sousa, P. Stachelek, N. Tohnai, S. Minakata, P. de Silva, P. Data and Y. Takeda. “Revealing the internal heavy chalcogen atom effect on the photophysics of the dibenzo[a,j]phenazine-cored donor-acceptor-donor triad.” *J. Mater. Chem. C*, **2021**, 9, 13942-13953. **doi:10.1039/d1tc02635f**

1. Abstract

This study explores four series of compounds with different core structures, namely **PyBTA** ([1,2,3]triazolo[4,5-b]pyridine), **NQPy** (acenaphtopyrido[2,3-b]pyrazine), **TTT** (tris([1,2,4]triazolo)[1,3,5]triazine), and **JAP** (dibenzo[a,j]phenazine), for use in OLED devices. Various combinations of donor-acceptor molecules were characterized and successfully applied. For **PyBTA** compounds were developed three different isomers by changing the position of the methyl group, each of them with three distinct donors. Some of these compounds exhibited room-temperature phosphorescence (RTP), while others showed thermally activated delayed fluorescence (TADF) properties. In the photophysics of **PyBTZ-x-PTZ** and **PyBTZ-x-PXZ** were observed contributions from different conformers in the PF and DF emissions attributed to the axial and equatorial conformers of the **PTZ** and **PXZ** donors. **NQPy** derivatives showcased multifunctional properties, exhibiting TADF, RTP or RTP/TADF, which could be modulated by the choice of donor. Additionally, they demonstrated effectiveness in singlet oxygen generation and displayed characteristics of aggregation-induced emission (AIE) and AIE enhancement (AIEE). The **TTT** series of compounds were studied with and without the addition of methyl groups at distinct locations within the molecule, leading to significant variations in their photophysics. All three derivatives employed **PTZ** as the donor, and the presence of conformers was observed in the PF and DF emissions. The inclusion of a methyl group in the donor nearly extinguished the DF properties, whereas the addition of a methyl group at the phenyl spacer reduced the DF contribution in comparison to the derivative without the methyl group, but it still had an effective DF contribution. In addition, the **TTT** derivatives also effectively showed aggregation properties, such as AIEE. The regioisomers of **JAP** compounds displayed TADF or RTP properties depending on the position and the donor. Notably, the OLED efficiencies achieved up to 15.9% for **PyBTA-2-PTZ**, 15.3% for **NQPy-DMAC**, and 12.4% for **TTT-PTZ**, all of which were fabricated using a solution processing.

2. Introduction

2.1. Organic semiconductors

Conductors are materials in which electric charges can move freely. In other words, within a conductor, the valence band and conducting bands overlap, and there is no energy gap between them.[1] In contrast, insulators are materials where electric charges do not flow easily or have extremely low conductivity due to a significant energy gap between the valence and conducting bands. On the other hand, semiconductors are materials where charges can flow, but their mobility is moderate, mainly due to a moderate energy gap between the valence and conducting bands. This difference in energy levels is referred to as the bandgap. Semiconductors play a crucial role in various technologies, such as organic light-emitting diodes (OLEDs), organic field-effect transistors (OFETs), and organic photovoltaics (OPVs).[2] In the context of organic semiconductors, the valence and conducting bands (although for single molecules, they are no longer bands but discreet energy levels) are often referred to as the highest occupied molecular orbital (HOMO) and lowest unoccupied molecular orbital (LUMO). The HOMO of a single molecule can be associated with the ionization potential (IP), which represents the energy required to remove an electron from a molecule. Conversely, the LUMO is related to the electron affinity (EA), which represents the energy required for the molecule to stabilize an additional electron.[2] There are various methods to modify the HOMO and LUMO orbitals, and one of the most effective approaches is chemically adding donor and acceptor groups to π-conjugated systems.[3] Additionally, the bandgap of organic semiconductors is closely tied to their application. For example, in OLED applications, the bandgap of the organic semiconductor is directly related to the energy absorbed and the colour of the emitted light.[3] On the other hand, in OPVs, the bandgap is critical for absorbing energy and efficiently separating charges to convert solar energy into electricity.[3] Considering the widespread use of semiconductors in everyday life, from computers and smart TVs to smartphones and more, this field of research holds immense importance and offers numerous opportunities for exploration and innovation.

2.2. OLED devices

Artificial illumination in the form of fire has been known since prehistoric times. A significant milestone was reached when the first electric bulb lamp, known as the Electric Arc lamp, was invented by Humphry Davy in 1802. It took 77 years for Thomas Edison to introduce the first commercially viable electric bulb lamp in 1879. Since then, lighting has become an integral part of people's lives. The concept of LEDs was initially reported in 1907.[4] Nowadays, it is nearly impossible to envision life without smartphones, smart TVs, and laptops. These devices have become indispensable to humanity and have played a crucial role in societal development. One of the key factors that have contributed to their popularity is their use in the displays of electronic devices. OLEDs have revolutionized electronic displays and lighting sources. OLED displays outperform traditional liquid crystal displays (LCDs) in several ways. They do not require a separate backlight system, resulting in more energy-efficient operation and vibrant colours. Additionally, OLED displays are thin and flexible, offering a sleek and adaptable profile.[5]

2.2.1. The first generation of OLEDs

The OLED was first reported in 1987 by C. W. Tang and S. A. VanSlyke, **Figure 1a**. At this point, the fabrication of such a device was itself a great discovery and had a huge impact on the field. Their device achieved, at this point, what they called a "*High external quantum efficiency of 1 % with a luminous efficiency of 1.5 lm/W and brightness upper than 1000 cd/m^2, all that with a turn-on voltage lower than 10 V*."[4] After their contribution to the field numerous researchers began to report on OLEDs with a wide range of structures and various organic emitters. The first generation of OLED devices utilized purely fluorescent emitters, which were unable to harvest triplet excited states. The chromophores in OLEDs are electrically excited through recombination of holes and electrons. Of these interactions, due to spin statistics, 25 % lead to singlet and 75 % lead to triplet excited states.[6] In a conventional fluorescent emitter, the triplet states (T_1) undergo a nonradiative process to the ground state (S_0) without emission of light, leading to a limited efficiency.[6] When the molecule is electrically excited the holes and electrons are coming from the electrodes to be recombined in the EML. When the exciton is formed there is one possibility of spin quantum number at singlet excited state ($m_s = 0$) and three possibilities of spin quantum number at triplet (m_s = 1 or 0 or -1). At this point is already possible to understand why the possibility of internal quantum yield (IQE) described before is just 25 % for fluorescent emitters because one in four excited states generated is S_1 and three are T_1. The Jabłoński diagram shown in **Figure 2** shows the Fluorescent emitter electrically excited and the OLED spin statistics.

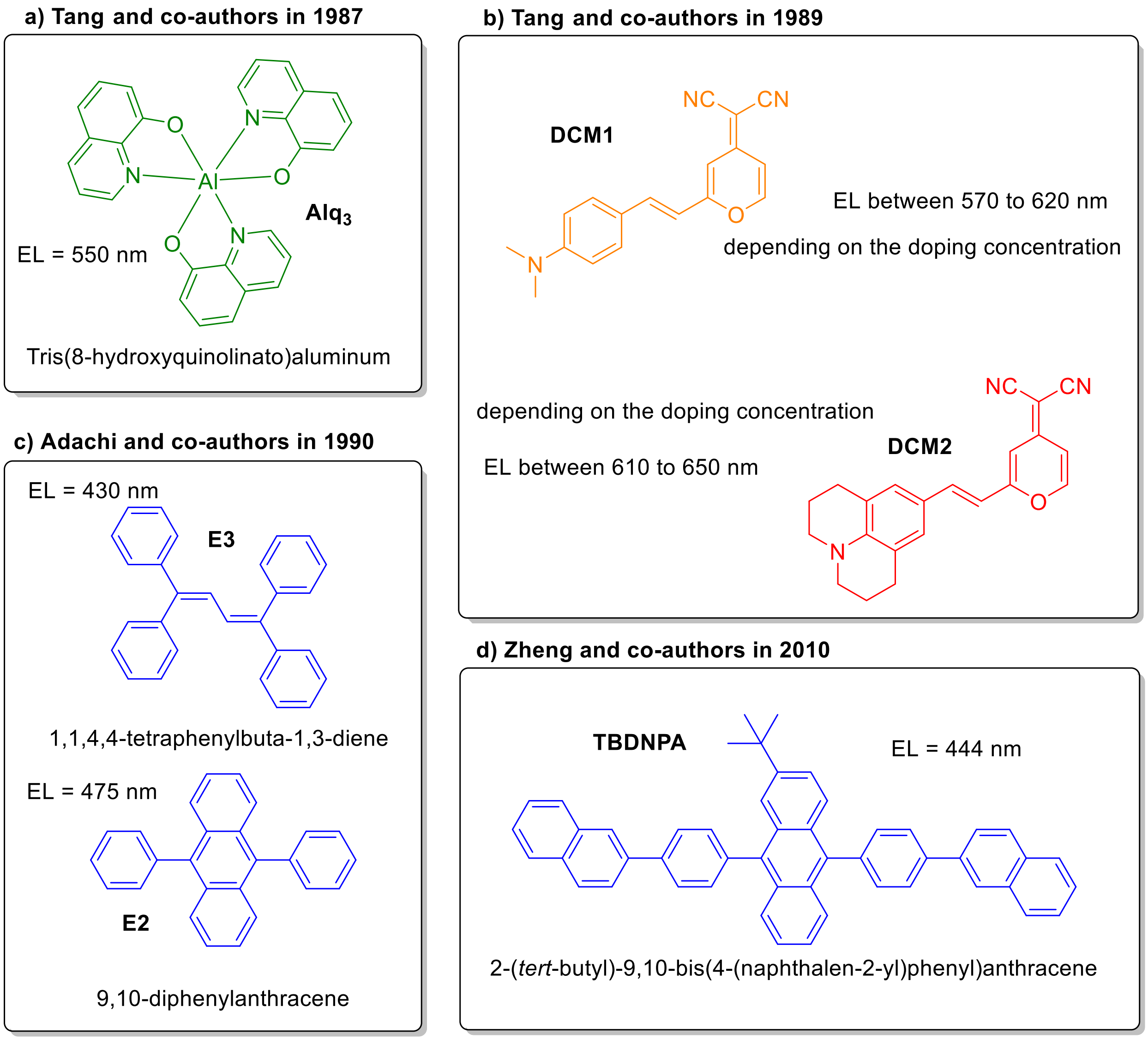
a) Tang and co-authors in 1987

b) Tang and co-authors in 1989

c) Adachi and co-authors in 1990

d) Zheng and co-authors in 2010

Figure 1. The first generation of OLED emitters: conventional fluorescent dyes.

Two years after the first OLED was reported, in 1989, the same group reported the first orange and red emitters, **Figure 1b**, by C. W. Tang, S. A. VanSlyke, and C. H. Chen.[7] With these two new compounds derived from malonitrile with different amine groups as side chains that they named DCM1 and DCM2, they achieved external quantum efficiencies (EQEs) of 2.3 % in both cases with Alq_3 as host. They observed that the concentration of the emitter in the host material was important. The emission maximum showed a dependence on the percentage of doping, changing the emission from 570 to 620 nm for the DCM1 and 610 to 650 nm for the DCM2.[7]

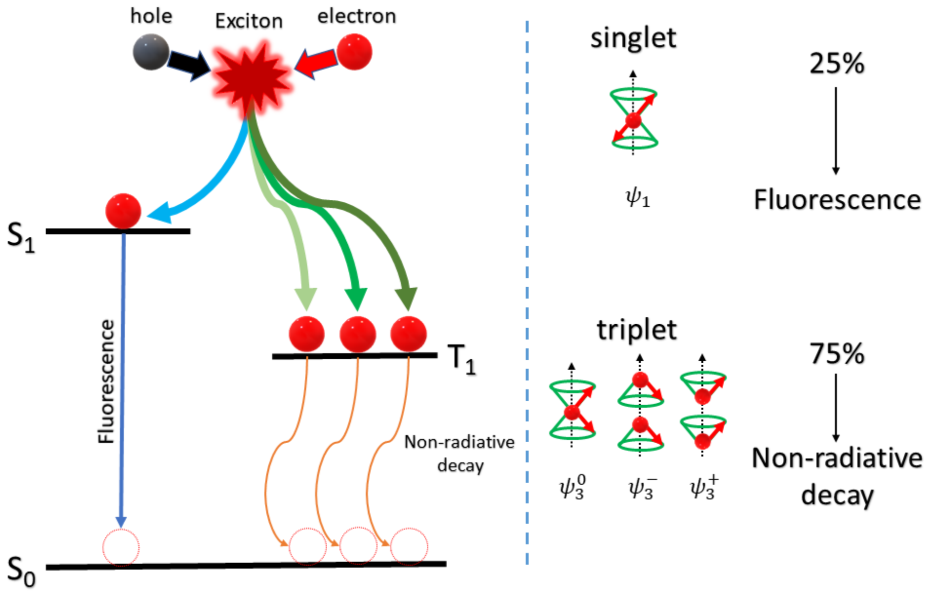

Figure 2. Electrical excitation of a fluorescent emitter and explanation of spin statistics.

Some first-generation blue emitters were reported by Adachi and co-authors in 1990, they published 15 molecules applied as emitters in OLED devices.[8] In this work, they published various anthracene derivatives substituted in 9 and 10 positions by phenyl groups, **Figure 1c**, shifting the emission to deep blue and achieving 2.82 % of EQE. In addition, the best results of their work were obtained with 1,1,4,4-tetraphenylbuta-1,3-diene named in the article as E3, **Figure 1c**, with emission at 430 nm and luminance of 700 cd cm^{-2} at current density of 100 mA cm^{-2}. This was obtained with a structure ITO/HTL (hole transporting layer)/EML(emissive layer)/ETL(electron transporting layer)/MgAg using the diamine *N*4,*N*4'-diphenyl-*N*4,*N*4'-di-*m*-tolyl-[1,1'-biphenyl]-4,4'-diamine as the HTL (hole transport layer) and the *t*-Butyl-PBD as ETL (electron transport layer).[8] In comparison, Zheng and co-authors published in 2010 a new emitter based on the anthracene core with substitutions at 9 and 10 positions that they called TBDNPA, **Figure 1d**.[9] The structure was similar to that reported by Adachi and co-authors in 1990, but they obtained with this structure an EQE maximum of 5.17 % and a maximum brightness of 6940 cd m^{-2} with an emission peak of 444 nm and full width at half maximum (FWHM) of 57 nm.[9] Nowadays new emitters based on fluorescence are not anymore the focus of OLED applications due to the low EQE achievable for these compounds.[6]

2.2.2. The second generation of OLEDs (PhOLEDs)

The problem with the first-generation OLEDs was the low maximum internal quantum efficiency (IQE) of 25 %, which resulted from the spin-statistics.[10] Trying to solve this problem the second generation of emitters was developed with room-temperature phosphorescent (RTP) materials that are able to explore the 75 % of electrons in the T_1 state, see section 2.3.2 for better understanding.[10,11] To do that the idea was to enhance the spin-orbital coupling (SOC) by the addition of heavy metals in complexes with organic ligands.[10] SOC is a relativistic effect that occurs when an electron in motion experiences a magnetic field from the electron movement in the molecule or by external voltage application.[12] This affects causing the coupling between the spin and the momentum of the electron making it possible to provide a degree of freedom for the electron spin.[12] Molecules with the presence of high atomic number atoms can provide a higher SOC due to the presence of more electrons in the closed shell structure. This effect is called as heavy atom effect and consists of the increasing of the SOC by the higher angular momentum that dominates the heavy atoms.[12] Metals such as platinum and iridium were and still are very explored in the second generation.[13,14] These complexes with higher SOC could provide the emission from T_1 reducing the nonradiative processes. In addition, they favour intersystem crossing (ISC) from the S_1 to the T_1, achieving the possibility of 100 % of IQE for these materials. These phosphorescent OLEDs are also called PhOLED.[10,11]

2.2.2.1. Iridium complexes

In 1999, Forrest and co-authors reported $Ir(ppy)_3$ [*fac*-tris(2-phenylpyridine)iridium], **Figure 3a**, as a green emitter applied as in PhOLED obtaining 8.0 % of maximum EQE with an emission peak of 510 nm. At 100 mA cm^{-2}, the EQE was 7.5 %, showing the stability of the PhOLED with increasing voltage.[15] A new derivative of iridium complex based on the same ligand phenylpyridine but now with additional ligand acetylacetonate (acac) to form the $Ir(ppy)_2(acac)$ complex (**Figure 3b**).[16] The introduction of the acac in the complex resulted in an increase in the EQE to 10.0 % at 1 mA cm^{-2} with 9,9'-(4,4'-biphenyldiyl)bis(9*H*-carbazole) (CBP) as host showing green colour emission at 525 nm published in 2001 by Lamansky and co-authors.[16] In the same year, Adachi and co-authors used a different host, 3-(biphenyl-4-yl)-5-(4-*tert*-butylphenyl)-4-phenyl-4*H*-1,2,4-triazole (TAZ), to achieve 19 % of EQE with green emission.[17] The use of 2,2,6,6-tetramethyl-3,5-heptyldione (tmd) instead of acac with tertbutyl groups in $Ir(ppy)_2(tmd)$, **Figure 3c**, increased the EQE to 32.3 % as reported by Kim and co-authors in 2014.[14] In the same work they improved OLED architectures, achieving for $Ir(ppy)_3$ and $Ir(ppy)_2(acac)$, EQEs of 26.3 % and 30.0 %, respectively.[14] The structures used by Kim and co-authors were ITO/TAPC/TCTA/TCTA:B3PYMPM: 8.4 mol% of the iridium complex/B3PYMPM/LiF/Al were the 1,1-bis-(4-bis(4-methyl-phenyl)-amino-phenyl)-cyclohexane (TAPC) was used as the hole injection layer, 4,4′,4″-tris(*N*-carbazolyl)-triphenylamine (TCTA) as the hole transporting layer (HTL) and bis-4,6-(3,5-di-3-pyridylphenyl)-2-methylpyrimidine (B3PYMPM) as the electron transporting layer (ETL).[14] In addition, the TCTA and B3PYMPM also were used as co-hosts in the EL. The emission peaks were at 513 nm, 520 nm and 524 nm for the complexes of $Ir(ppy)_3$, $Ir(ppy)_2(acac)$ and $Ir(ppy)_2(tmd)$, respectively.[14] The iridium complexes were also used in red and blue colours. Some of the most highly efficient PhOLEDs with red emission were developed by Yang and co-authors in 2018 using BPyThIr as the emitter, **Figure 3d**. BPyThIr contains three different ligands: 5-(dimesitylboranyl)-2-phenylpyridine, 2-phenylthiazole, and acac.[18] With that they achieved 28.5% EQE with an emission peak at 604 nm and a maximum luminescence of 59154 cd m^{-2}.[18] Examples of blue emitter derivatives of iridium complexes are for example Ir-1, Ir-2 and Ir-3 published in 2019 by Kim and co-authors. They achieved high EQEs of 29.0 %, 31.9 % and 19.5 %, respectively and a maximum luminance of more than 10000 cd m^{-2}. These derivatives have a complex ligand structure, shown in **Figure 3e**.[19]

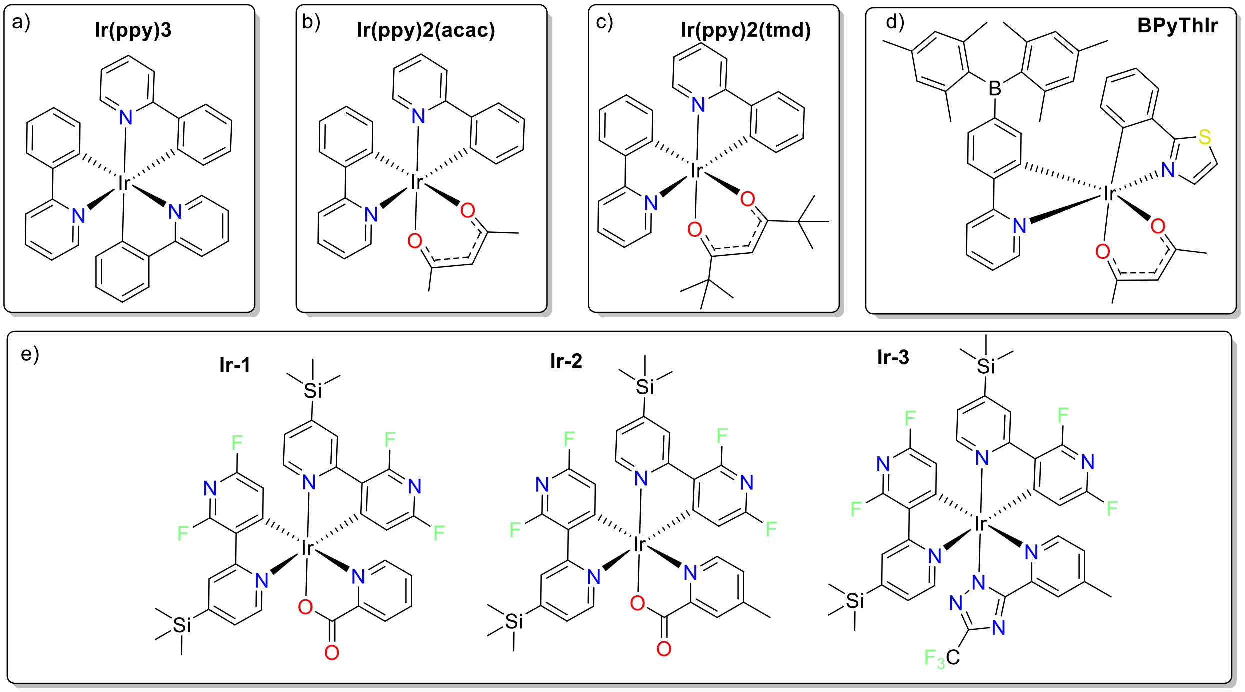

Figure 3. Iridium complexes developed for the second generation of OLED emitters.

In 2023, complexes with iridium are still being investigated with more and more articles being published. The Ir-CF$_3$, **Figure 4a**, complex developed and reported by Ou and co-authors has shown great properties when applied in PhOLEDs with a short lifetime of phosphorescence, ~1 μs, high EQE up to 32 % and extremely low-efficiency roll-off obtaining 30.8 % of EQE at 1000 cd m^{-2}. The maximum luminance obtained was 38277 cd m^{-2}.[20] Furthermore, small modifications are still being explored. Xie and co-authors investigated different phenylpyridine ligands with the addition of cyano group in different positions as shown in **Figure 4b**. They reported Ir(10-CN), Ir(4-CN) and Ir(3-CN) with EQEs of 17.2 %, 17.2 % and 25.4 % and RTP lifetime in the range between 0.79 μs and 2.08 μs. In addition, the maximum luminance obtained to Ir(3-CN) was 61340 cd m^{-2} at 8.0 V while the EQE remains high at 1000 cd m^{-2} and 10000 cd m^{-2} being 24.3 % and 19.9 %. The colours obtained varied from red to yellow, depending on the position of the cyano group.[20] These studies showcase the continuous development and improvement of iridium-based complexes for OLED applications, spanning a wide range of emission colours and achieving high EQEs and other desirable properties.

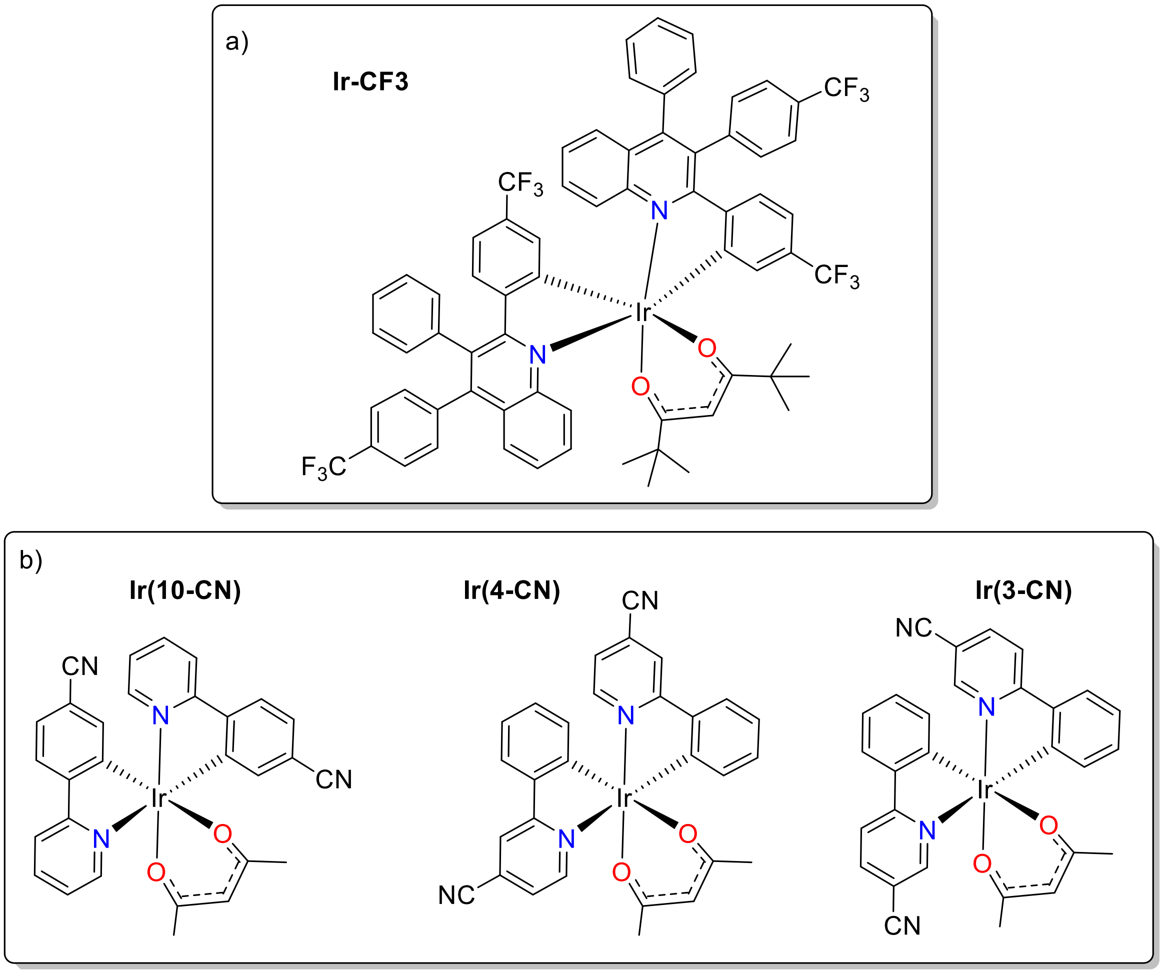

Figure 4. More examples of the second generation of emitters developed to phosphorescence OLED. Iridium complexes.

2.2.2.2. Platinum complexes

Platinum complexes were also applied in the second generation of OLED emitters. In 2008, Cocchi and co-authors reported a platinum complex that they called PtL^{2}Cl, **Figure 5a**. They have achieved EQEs up to 14.5 % and a near-infrared emission (NIR) around 700 nm.[21] They also emphasized the significance of the OLEDs' architecture, particularly concerning to the cathode. They achieved the most favourable results with a calcium electrode combined with an injection layer measuring 0.5 nm of lead oxide (PbO_2).[21] In 2017, Ly and co-authors introduced a novel class of platinum complexes, that they called Pt(fprpz)$_2$, Pt(fprpz)(fppz), and Pt(fprpz)(tbfppz), **Figure 5b**, with emissions at 740 nm, 703 nm and 673 nm achieving up to 24 % with the first compound showing a photoluminescence quantum yield (PLQY) of 81 % in thin films.[22] In 2015, Chow and co-authors reported a green Pt complex shown in **Figure 5c**.[23] They obtained a high PLQY of 99 % in DCM at room temperature and EQE up to 22.8 % for a green OLED.[23]

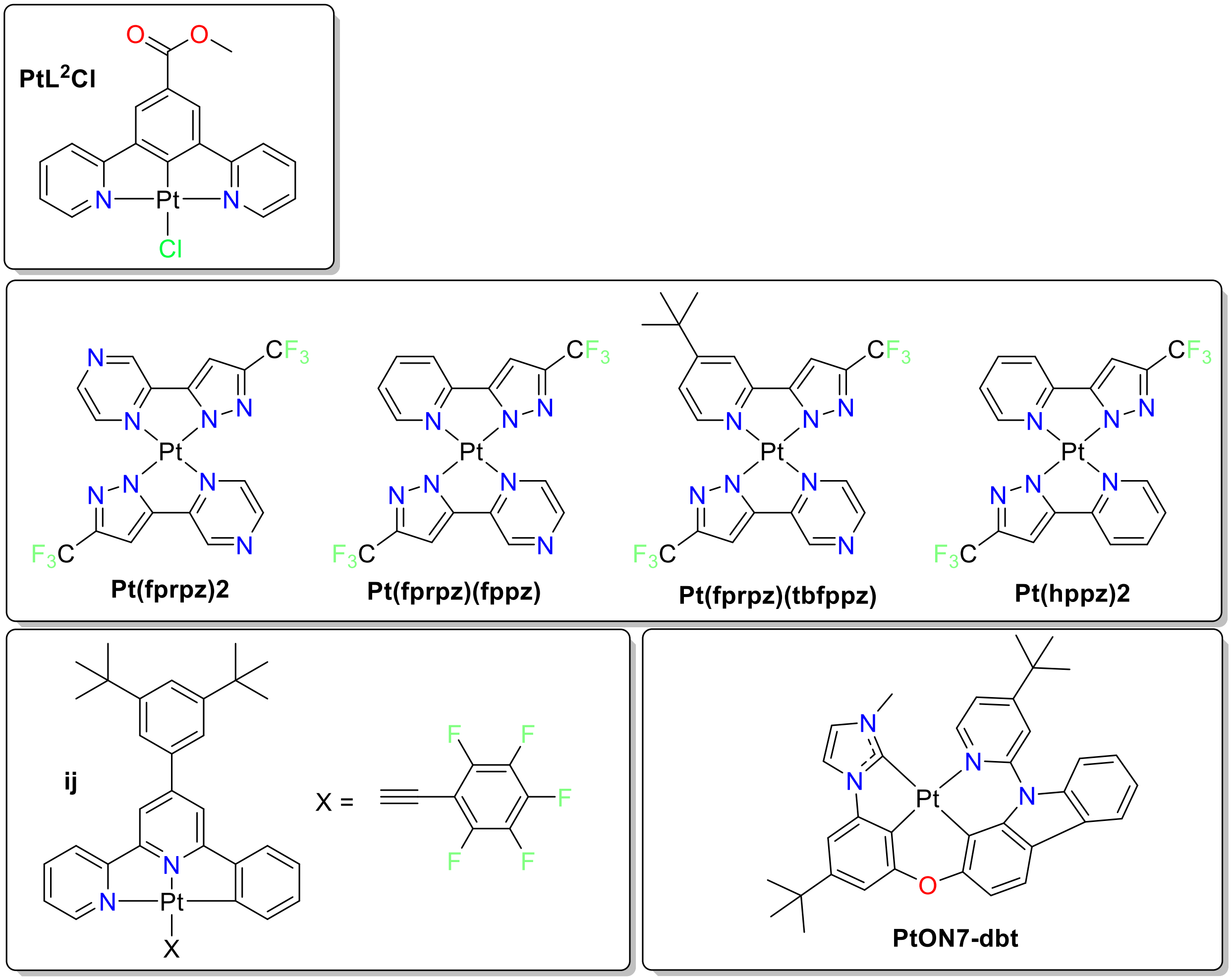

Figure 5. Platinum complexes developed for the second generation of OLED emitters.

In 2014, Fleetham and co-authors reported an efficient new blue emitter based on a phosphorescent Pt complex (PtON7-dbt), **Figure 5d**, achieving 24.8 % with very thin electroluminescent emission peak with FWHM of 29 nm and maximum emission at 451 nm.[24] Wang and co-authors reported in 2023 a high EQE of 31.8 % for emitter based on Pt complex, **Figure 5e**, in OLED devices with red electroluminescence.[25] In addition, they reported the high lifetime stability of this device being over 14000 hours showing a potential for these complexes to be commercialized.[25] In summary, these studies demonstrate significant advancements in OLED technology, with each focusing on different aspects such as emission colour, efficiency, and stability. The reported EQEs and PLQYs vary across the studies, highlighting the versatility of platinum complexes in OLED development.

2.2.2.3. Copper Complexes

Besides the complexes of iridium and platinum complexes of other heavy metals have been reported, and complexes of more abundant metals such as copper have also been investigated. Hashimoto and co-authors reported a green emitter based on a copper complex with a bidentate phosphine-based ligand with the third ligand being bromine in a trigonal planar geometry of the complex, **Figure 6a**.[26] They achieved the OLED performance of 65.3 cd A^{-1} and EQE of 21.3 % showing the promising properties of three-coordinate copper (I) complexes.[26] Kandasamy and co-authors have reported in 2023 copper-based complexes CuL^1(acacp), CuL^2(acacp) and CuL^3(acacp), **Figure 6b**, with EQE up to 22.5 %, 26.8 %, and 30.4 %, with the last one showing high maximum brightness of 22800 cd m^{-2} and maximum current efficiency of 30.5 cd A^{-1}.[27] Their study investigated the influence of the heteroatom in the ligand changing from -O- to -NH- and -S- in the heterocycle showing the versatility of complexes that can be explored not only using platinum and iridium metals but also copper or even other ones to achieve highly EQEs and highly properties in general.[27]

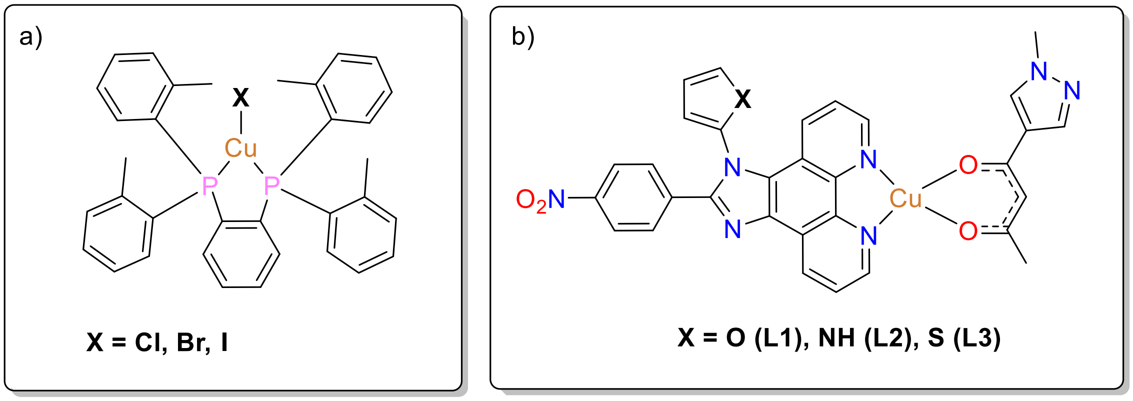

Figure 6. Copper complexes developed for the second generation of OLED emitters.

2.2.3. Third generation of OLEDs

The third generation of OLEDs consists of molecules that exhibit thermally activated delayed fluorescence (TADF) properties. Similarly to the phosphorescent counterparts, TADF materials also can show an internal quantum efficiency (IQE) of up to 100 %.[6,28] They rely on the TADF phenomenon, which is discussed in detail in section 2.3.3.[6,28] In TADF the excited triplet T_1 states are converted to the S_1 state through reverse intersystem crossing (RISC).[28] With that the emission from prompt fluorescence (PF) and TADF arrive from the same excited state and usually display the same spectral profile. The first report of a metal-free TADF molecule being applied in OLED devices was in 2011 by Endo and co-authors from the Adachi group.[29] The authors designed a molecule called PIC-TRZ, **Figure 7a**, showing a separation between the acceptor and the donor moiety splitting effectively the highest occupied molecular orbital (HOMO) and the lowest unoccupied molecular orbital (LUMO).[29] This good separation can provide a small energy gap between the S_1 and T_1 (ΔE_{ST}) states, fundamental for the TADF process, more details are in section 2.3.3.[30] With that the authors achieved EQE of 5.3 %.[29] A breakthrough publication in 2012 in Nature was published by Uoyama and others from the Adachi group.[31] They have published 6 derivatives of dicyanobenzene core using carbazole as a donor where three of them were TADF materials and applied in OLEDs the 2CzPN, 4CzIPN and 4CzTPN-Ph, **Figure 7b**.[31] These molecules showed emission colours spanning from blue to orange obtained by decorating the carbazole donor moieties with additional groups. They used CBP as a host for green and orange luminophores and 2,8-bis(diphenylphosphoryl)dibenzo[b,d]thiophene (PPT) for blue emitters.[31] The EQE reported was 19.3 % for green (4CzIPN), 11.2 % for blue (2CzPN), and 8.0% for orange (4CzTPN-Ph) OLED, significantly higher than the 5.3 % shown before.[31]

After these works many others began developing novel TADF emitters of various designs. Recent works on the topic have been reported increasing EQEs of such devices. In 2018 Wu and co-authors reported high EQEs for OLED devices of 37.8 % and 32.4 % for derivatives CzDBA and tBuCzDBA, **Figure 8a**.[32] The incorporation of boron atoms with vacant *p* orbitals provides an intriguing strategy for designing the acceptor moiety. Furthermore, a phenyl group was added as a spacer between them, with methyl groups in the ortho position to the boron, leading to increased hindrance and resulting in a twisted shape.[32] Both compounds showed green emission with PL maxima at 528 nm and 542 nm for CzDBA and tBuCzDBA respectively with FMWH of 75 nm and 82 nm.[32]

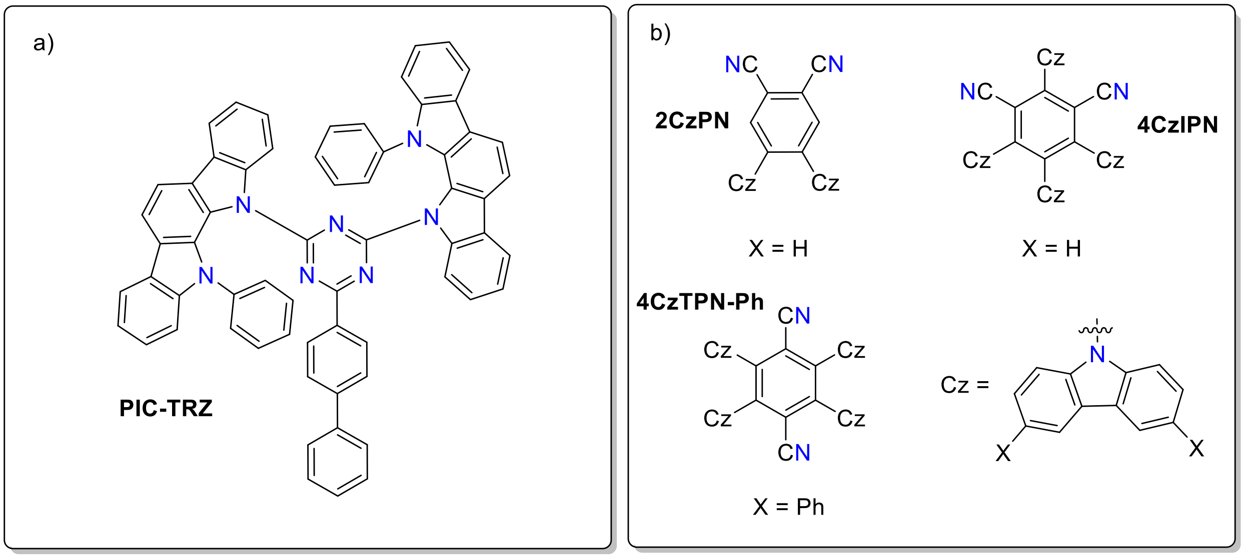

Figure 7. Third generation of emitters developed for TADF OLED applications reported by Adachi and others.

In the red/orange region, Zeng and co-authors have developed two derivatives containing *N*-(4-*tert*-butylphenyl)-1,8-naphthalimide (NAI) as the core and dimethylacrydine (DMAC) and diphenylacrydine (DPAC) as donors, NAI-DMAC and NAI-DPAC, **Figure 8b**.[33] The choice of the NAI acceptor was due to the high electron-withdrawing capability of this group associated with its high planarity. Besides that, the authors reinforce that the DMAC and DPAC are quite rigid which favours the twisted CT state.[33] The authors could achieve with this structures EQEs of 21 and 29.2 % for NAI-DMAC and NAI-DPAC.[33] The ΔE_{ST} of these compounds were 0.09 eV and 0.17 eV with lifetimes of TADF emission of 14.7 µs and 48.7 µs for NAI-DMAC and NAI-DPAC, respectively.[33] In 2015, Tsai and co-authors reported an efficient blue OLED based on a TADF emitter.[34] They used 2,4,6-triphenyl-1,3,5-triazine (TRZ) core and with DMAC as a donor, **Figure 8c**, they achieved a TADF material capable of being used as a dopant in a host for OLED and also as a non-doped OLED showing 26.5 % and 20.0% EQE, respectively.[34] The PLQY of 8 wt% of DMAC-TRZ in films with mCPCN host was 90 % with the delayed component being 34 % of this emission.[34] One year after this work, in 2016, Wu and co-authors developed other two derivatives of TRZ but now with DPAC and SpiroAC [10*H*-spiro[acridine-9,9'-fluorene]] donors, **Figure 8d**, which also give blue OLED electroluminescence.[35] The emission of these two compounds was blue shifted in relation to the DMAC-TRZ emission and the PLQY of the films were even higher for SpiroAC-TRZ achieving 100 % against 90 % for DMAC-TRZ and 82 % for DPAC-TRZ. The EQE obtained for these compounds was 36.7 % for SpiroAC-TRZ and 25.8 % for DPAC-TRZ, outperforming that reported for DMAC-TRZ.[35]

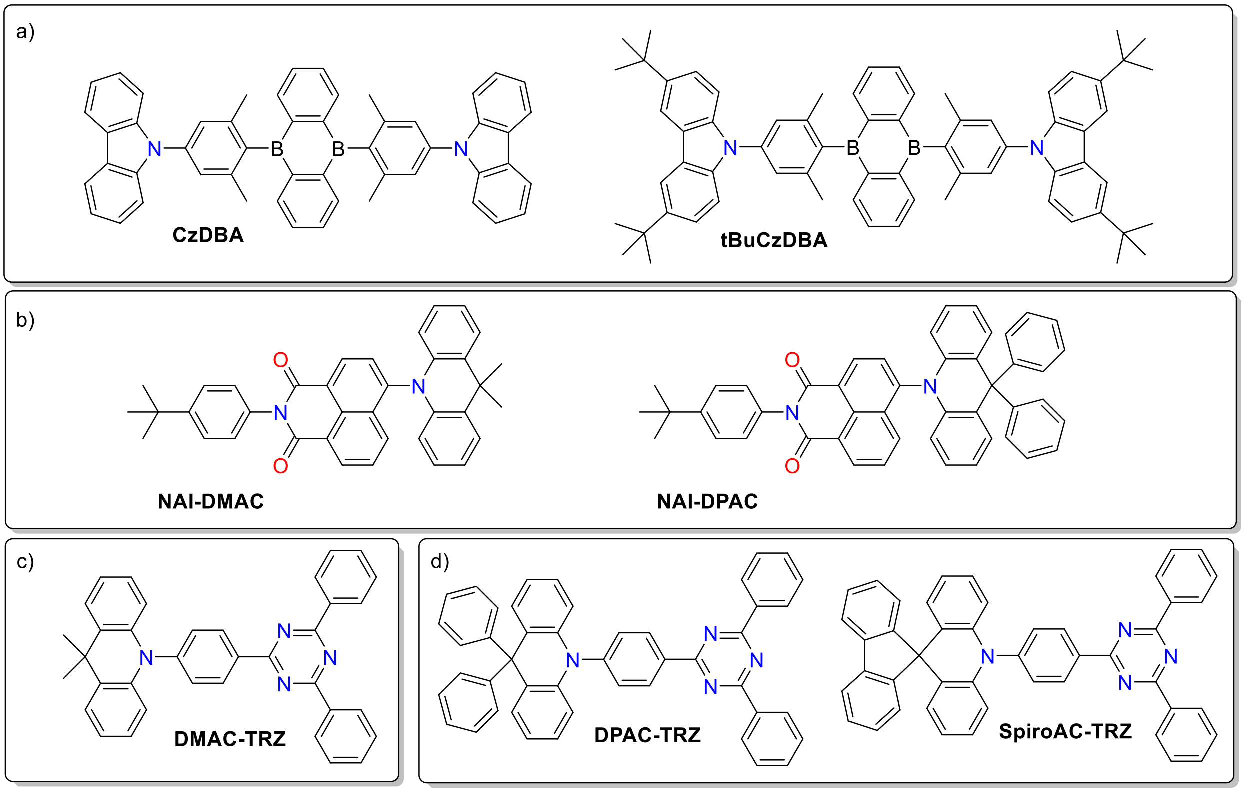

Figure 8. The third generation of emitters was developed for use in TADF OLED.

In 2019, Jayakumar and co-authors reported three new derivatives with large steric hindrance based on 2,4,6-triphenylpyridine-3,5-dicarbonitrile core and carbazole as donors resulting in the compounds 26tCzPPC, 246TCzPPC, and 35tCzPPC, **Figure 9a**.[36] The resultant blue OLED devices with 5 wt% of emitters in the mCBP host showed EQEs of 25.4 %, 29.6 % and 18.2%. The ΔE_{ST} were 0.090 eV, 0.063 eV and 0.120 eV, respectively. The PLQYs of the films of 5 wt% of emitters in mCBP were also high at 96 %, 98 % and 86%, respectively.[36] The position of the carbazole donors had a significant effect on the final luminescent properties. For example, *ortho* substitution increased the PLQY and the contribution of the DF emission in comparison with the donors in *meta* position.[36] In 2023 a new class of organic emitters was reported by Derkowski and co-authors showing a V-shaped emitter, an out-of-plane structure built around a seven-membered ring core.[37] The compounds named 4a, 4b, 4c and 4d, shown in **Figure 9b**, have presented a ratio of DF/PF at 32, 17, 10 and 0.3 in Zeonex and 4.6, 2.0, 2.0 and 0.6 in CBP matrix. They reported OLED efficiencies of up to 13.6 % for 4c.[37] In 2022, new emitters based on spiro-linked donor moieties were developed by Yi and co-authors, **Figure 9c**.[30] They observed that it was possible to regulate properties such as ΔE_{ST}, k_{RISC} and PLQY, for example, by using isomeric structures.[30] Emitters SpiroAC-PyoCN and SBAC-PyoCN show PLQY of 100 %. These compounds achieved 33.7 % and 36.1 % EQE, respectively.[30] In 2022, Xie and co-authors published a paper showing a boron derivative as an acceptor and phenoxazine (PXZ) or diphenylamine-decorated PXZ derivative in PXZBO1 and PXZBO2, **Figure 9d**.[38] These two compounds show high EQEs of 25.9 % and 29.7 %, emission maxima at 506 and 572 nm, PLQY of 94 % and 97%, respectively, and ΔE_{ST} of 0.01 eV in both cases.[38]

All these studies emphasize the importance of exploring new OLED materials. Fine-tuning the molecular structure can lead to the emergence of novel properties, thus increasing the potential for future commercial applications. It is worth noting that the typical design approach for TADF emitters traditionally revolves around introducing new acceptor cores while relying on a limited set of donor materials like CBZ, DMAC, DPAC, and PXZ, for instance. New challenges arise in the form of designing and synthesizing novel acceptor and donor cores and gaining a more profound understanding of the TADF mechanism, all while keeping an eye on potential practical applications. Readers can find more in-depth information about the TADF mechanism in section 2.3.3, which also covers its non-OLED applications.

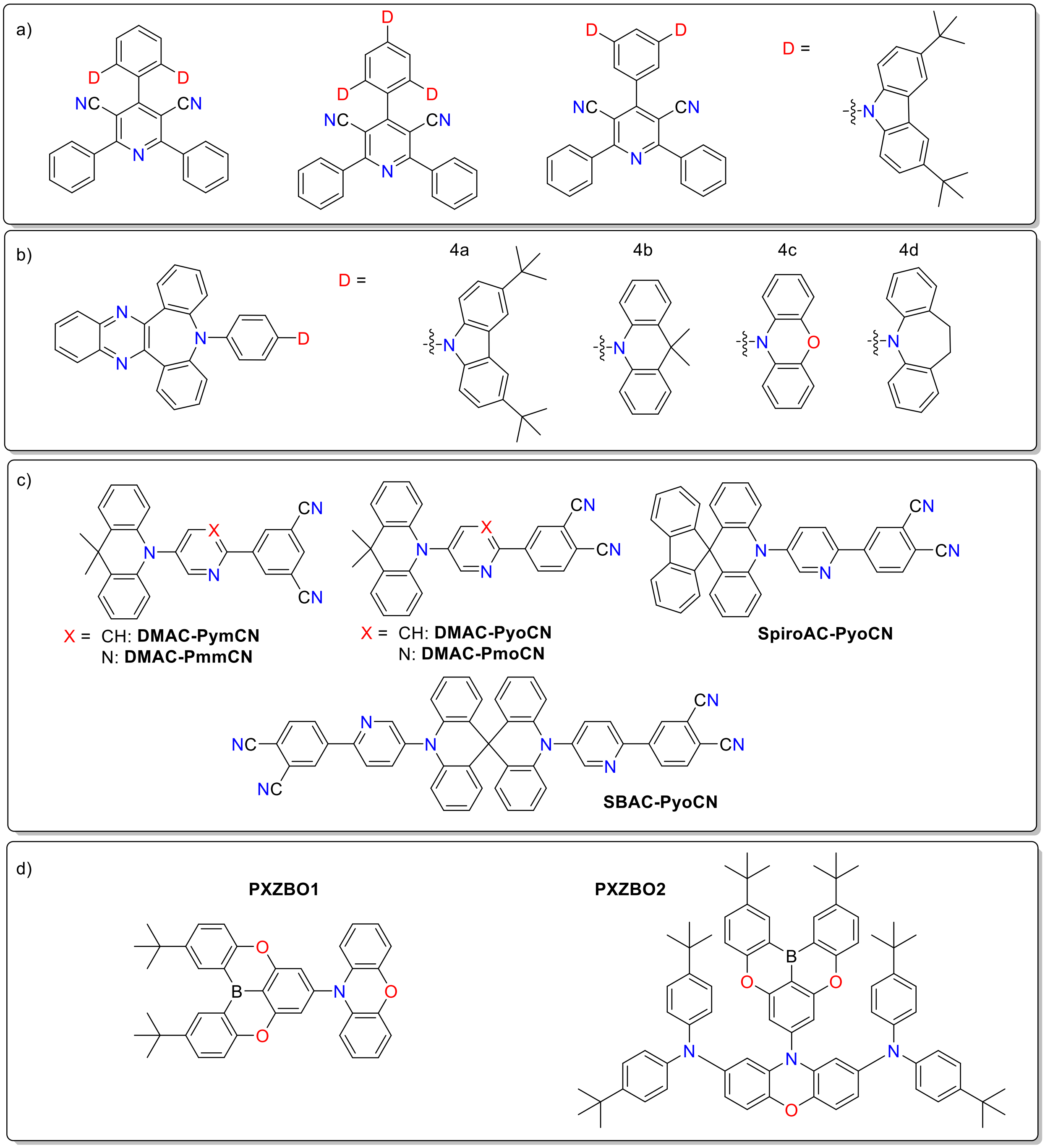

Figure 9. Emitters developed for TADF OLED applications.

2.2.4. Structure of OLED devices

The simplest OLED device structure consists of an emissive layer (EML) sandwiched between two electrodes: anode and cathode.[39] However, this basic configuration often exhibits limited efficiency due to its simplicity. To enhance device performance, additional layers are introduced.[39] The primary objective is to improve the recombination of electron-hole pairs. Electrons and holes are injected from their respective electrodes and traverse through various organic material layers before eventually recombining within the emissive layer. This recombination process results in the creation of excited states known as excitons. Notable layers in OLED devices include the electron and hole injection layers (EIL and HIL), electron and hole transporting layers (ETL and HTL), electron and hole blocking layers (EBL and HBL), and the emissive layer (EML). These layers are illustrated in **Figure 10**.

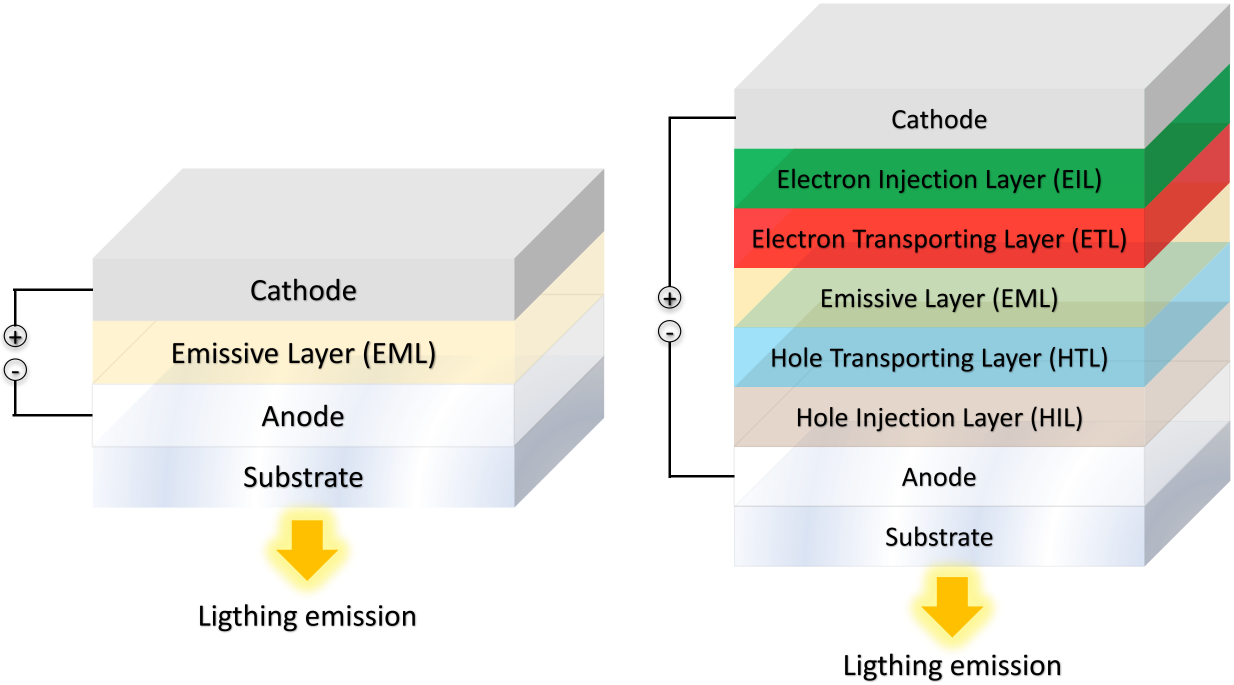

Figure 10. a) Simple OLED structure with EML sandwiched between cathode and anode. b) Complex OLED architecture with a multi-layered structure.

The devices can display a very simple structure as shown in **Figure 10a** but also a multilayer structure, as demonstrated in **Figure 10b**. Recombination and the resultant exciton formation can take place in any part of the device. However, the optimal design of an OLED leads to the recombination occurring solely in the EML. With the multilayer structure it is possible to obtain better control over the recombination in an OLED. Indeed, the external quantum efficiency is described by the following equation:

$$\eta_{ext} = \eta_r \, \phi_f \, \chi \, \eta_{out} = \eta_{int} \, \eta_{out} \quad (1)$$

Where the η_{ext} is the external quantum efficiency, η_r is the probability of hole and electron recombination, ϕ_f is the photoluminescence quantum yield, χ is the probability for radiative decay occuring, and η_{out} is the fraction of photons that escape from the device. The η_{out} is approximately 20-30 % in a common device while the probability η_r and the ϕ_f can be approximate to 1 in ideal conditions, while the χ is 25 % for a fluorescent emitter, 62.5 % for a TTA emitter (discussed later in the thesis), 100 % for RTP and TADF emitters. The origin of these figures will be explained later in the text. This calculation means that even for an ideal OLED emitter the maximum external quantum efficiency would be around 25 %. Besides that, the excitons in OLED may undergo certain quenching processes, such as triplet-polaron quenching (TPQ) and triplet-triplet annihilation (TTA), for example, with these processes resulting in a reduction of OLED efficiency. Careful design of OLEDs and OLED emitters can significantly reduce the effects of these processes.[13] More details are presented in section 2.3.4.

2.2.5. Layers in OLED devices

As mentioned earlier, optimisation of the structure of the OLED can improve its characteristics, resulting in higher EQE, higher current efficiency, lower roll-off, and higher power efficiency, among others.[40] The present section shows the function and functionality of each layer, as shown in **Figure 11**.

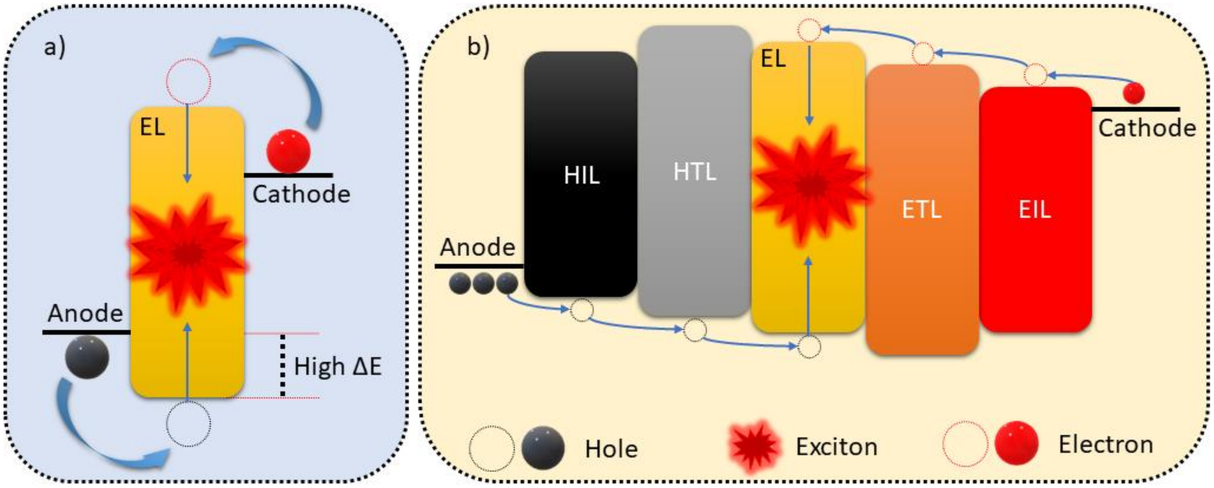

Figure 11. Representation of a typical OLED structure and exciton formation. a) simplest OLED configuration with a higher potential step between electrodes and the EML. b) Multilayer OLED configuration lowering the potential step.

2.2.5.1. Injection Layers

Organic semiconductors are directly influenced by their HOMO and LUMO energies and these energies are connected to the injection of charges in the device. These energies should match with the electrode work functions to reduce the charge injection barriers represented by ΔE in **Figure 11**. This is the role of injection layers as the closer these energies are, the better will be the injection of the charge carriers. In addition, injection layers can be used to optimise OLEDs using various electrode materials displaying different work functions. **Figure 11** demonstrates the importance and function of injection layers.[40] Examples of EILs are: lithium fluoride, caesium fluoride, and caesium carbonate, while popular HILs are PEDOT:PSS, MoO_x or HAT-CN.

2.2.5.2. Transporting Layers

The next comes the transporting layer which takes part in transporting electrons and holes to the EML. They are used, alongside injection layers, to balance the ratio of electrons and holes arriving to the EML. The HOMO of the hole transport layer and LUMO of the electron transport layer should match those of the EML. Sometimes addition of a transport layer can be sufficient to balance charge carriers in an OLED.[40] Examples of materials acting as charge transport layers are presented in **Figure 12**.

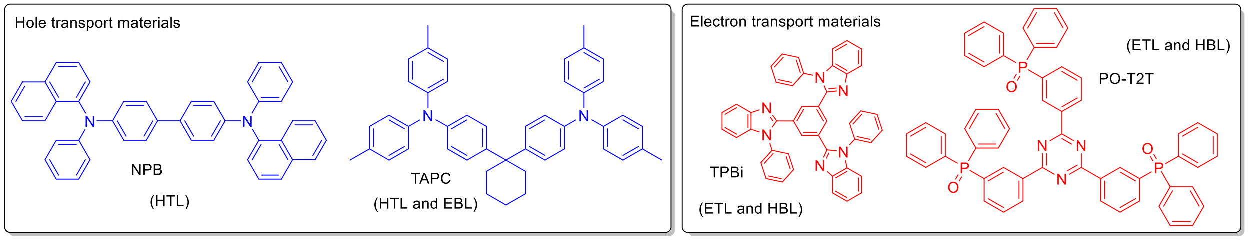

Figure 12. Common compounds used as HTL (left) and ETL (right) in OLED devices.

2.2.5.3. Blocking Layers

These layers are used to block holes or electrons passing through. The problem with electrons and holes potentially passing through a device without recombination in EML is that it leads to reduced device efficiency. In that way, the blocking layers are added to create a high potential barrier blocking the charges from leaving the EML. Holes are blocked by adding a HBL, a compound with a low HOMO energy, which creates an energy barrier for holes. While EBLs have a high LUMO, creating a large energy barrier for electrons.[40] Blocking layers are also transport layers for the opposite charge, *i.e*. HBL is also an ETL. Compounds commonly used for this purpose are presented in **Figure 13**.

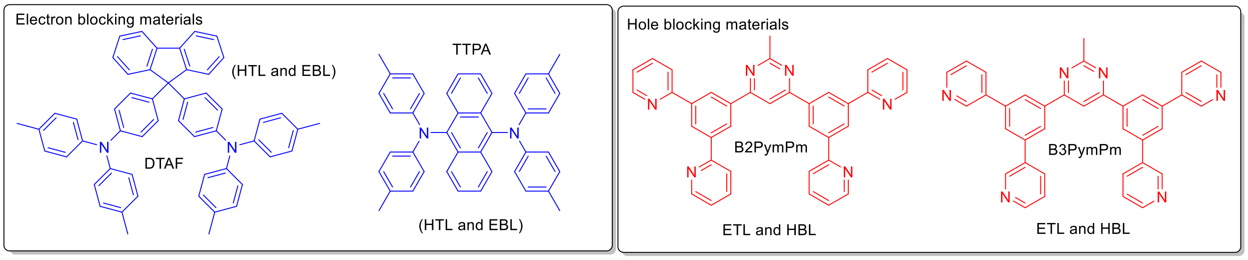

Figure 13. Electrons (right) and Hole (left) blocking materials used in OLED devices.

2.2.5.4. Emissive Layer (EML)

The emissive layer is the “heart” of the device and it is where the “magic” happens. The emissive layers can be separated into two types, doped and non-doped. Non-doped or neat layers are simpler because they contain only one component: the emitter. However, the use of non-doped layers may lead to reduced PLQY due to aggregation-caused quenching (ACQ), TTA and the potential presence of other non-radiative processes. The use of a host is fundamental in most cases as this prevents luminescence quenching, but also improves the electrical properties of the device. The choice of a host depends on the nature of the emitter. One of the key factors for achieving a high EQE with TADF or phosphorescent dopants is that the host material for the emitting dopant must satisfy crucial requirements such as having higher S_1 and T_1 energy levels than those of the dopant, efficient energy transfer to the dopant, low carrier injection barriers from both the transporting layers and efficient exciton confinement. The host materials in TADF OLEDs are similar to those in PhOLEDs, although some minor prerequisites need to be fulfilled.[41] Some of the most common materials used as hosts are presented in **Figure 14**.

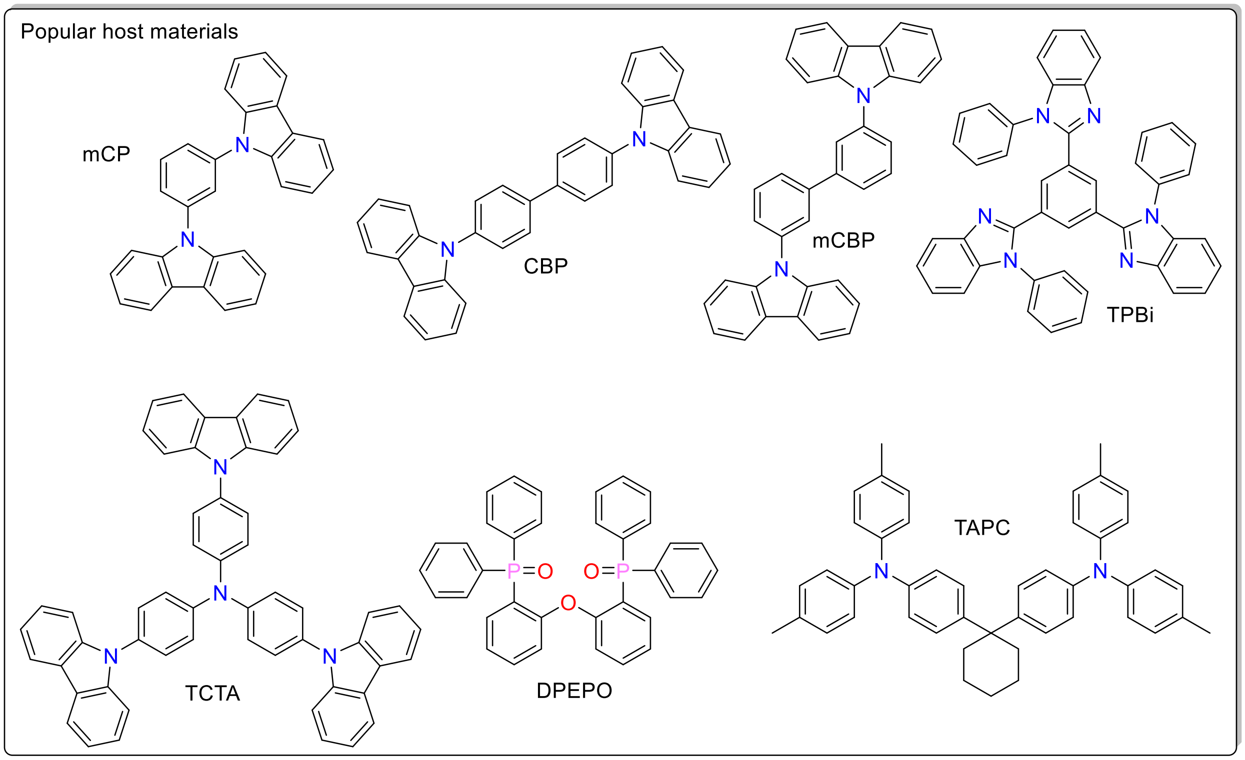

Figure 14. Hosts materials used in OLEDs.

2.3. Photoluminescent processes

As discussed before, the emission process is the key point of OLED devices. These processes will be explained in more detail in this section with a detailed discussion of differences between fluorescence, phosphorescence, and thermally activated delayed fluorescence. In addition, some of the processes leading to the non-radiative decay will also be explained. Furthermore, aggregation effects that contribute to quenching and emission enhancement will be discussed.

2.3.1. Fluorescence

Fluorescence is the most straightforward process that a chromophore undergoes to emit light. In the first case, the chromophore is photoexcited promoting the electron from the fundamental state (S_0) to an excited state (S_n). Following Kasha's rule, the electrons can be emitted in high yield only by the first excited state, so, even if the electron goes to a second or third excited state it will be rapidly interconverted by non-radiative decay to the first excited state, in this case, S_1. The molecule in the S1 excited state can undergo two competing processes in addition to non-radiative decay. In the first one the chromophore in the excited state (S_1) returns to the fundamental state (S_0) by emission of light (fluorescence). In the other process the electron undergoes intersystem crossing (ISC) to the triplet excited state (T_n) and decays to the fundamental state (typically) through non-radiative decay. Jabłoński diagram in **Figure 15** shows these processes. In this figure it is possible to observe that if the molecule is photoexcited it can have a 100 % photoluminescence quantum yield (PLQY) as long as the ISC and singlet non-radiative decay display a very small rate constant ($k_{ISC} \cong 0$ and $k_{nr}^S \cong 0$) which would make all excited states decay to the S_0 though fluorescence.

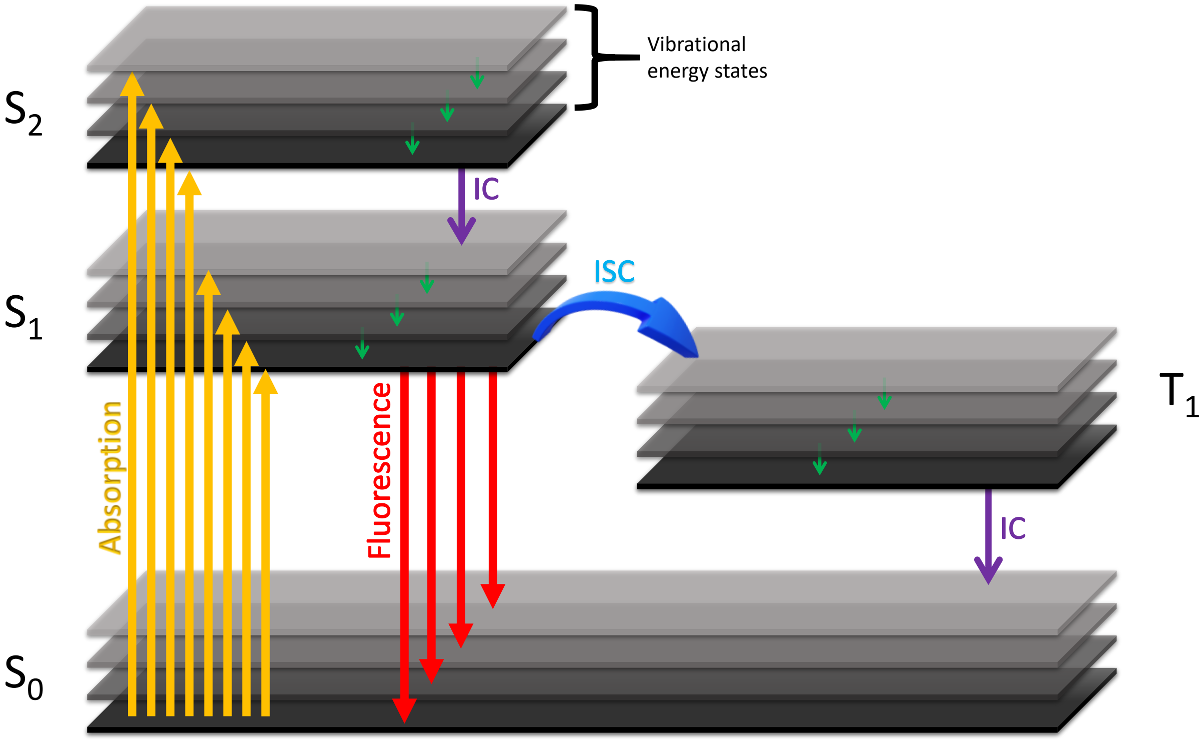

Figure 15. Jabłoński diagram of fluorescence of a generic emitter.

2.3.2. Phosphorescence

Phosphorescence emitters offer an alternative possibility for T_1 excited states to decay radiatively. This radiative process from T_1 to S_0 is called phosphorescence and it is a spin-forbidden process as it occurs with a necessary spin flip as the ground state has a singlet character. Unlike fluorescent emitters, k_{ISC} is usually large in phosphorescent luminophores due to the spin-orbit coupling accelerating not only the T_1 to S_0 transition but also the S_1 to T_1 route. The Jabłoński diagram in **Figure 16** shows the behaviour of a typical phosphorescent emitter after photoexcitation.

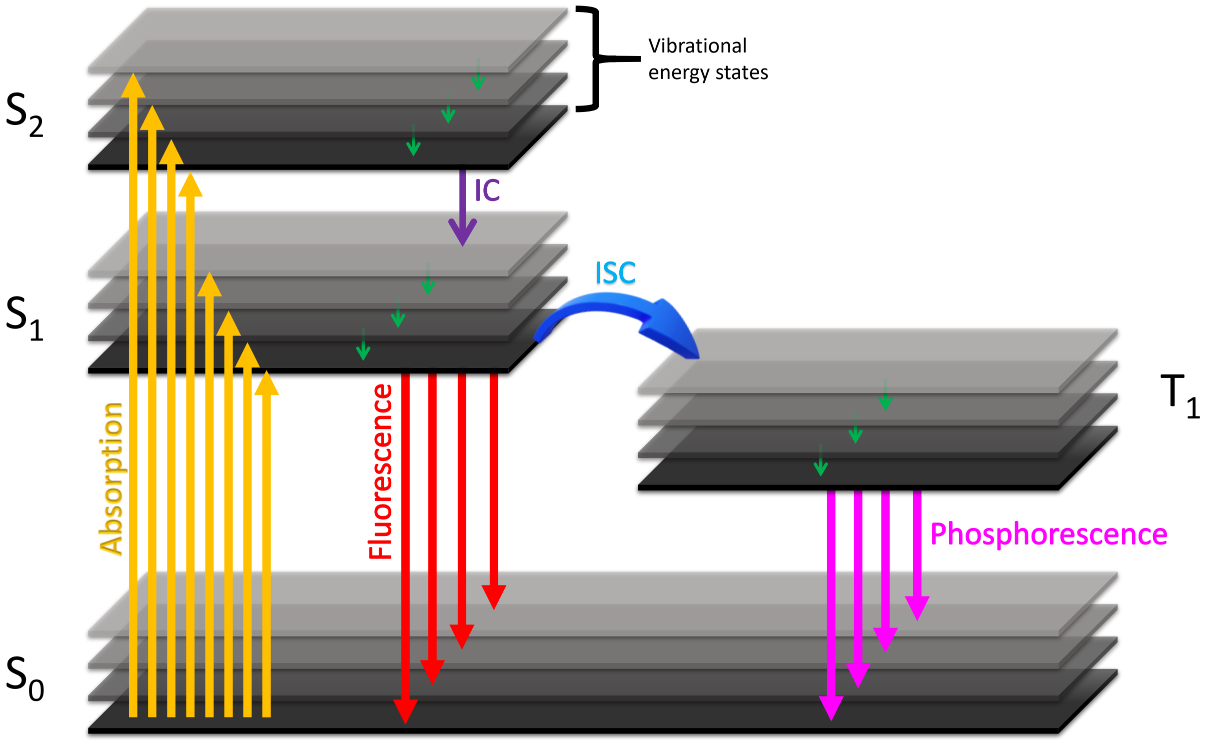

Figure 16. Jabłoński diagram of phosphorescence of a generic emitter.

When the phosphorescent emitter is applied in OLED devices, electrical excitation leads to the formation of 75 % T_1 and 25 % S_1 states, as shown in **Figure 17**. In addition, the ISC process is helping to promote the transition from the S_1 to T_1 state which can lead to phosphorescence accounting for 100 % of electroluminescence. Spin-orbital coupling (SOC) is a relativistic effect associated with the angular moment and spin of the electron and plays an important role in the ISC.[42,43] SOC is also accelerating the radiative rate from T_1 to S_0, hence speeding up phosphorescence.[42,43] Besides the use of metal complexes with organic ligands to achieve an effective SOC and allow efficient decay from T_1 to S_0, metal-free materials with similar properties are gaining some popularity. Pure organic, metal-free compounds are however more difficult to display efficient phosphorescence due to the lower magnitude of SOC induced by non-transition metal atoms.[44] Factors such as non-radiative decay and quenching of triplet excitons contribute to the decrease in the luminescence quantum yields of the emitters at room temperature, including phosphorescence.[44]

The heavy atom effect is the perturbation in the SOC caused by the presence of a high atomic number atom. Due to the presence of higher atomic orbitals, the superposition with the molecular orbitals is more effective in increasing the SOC while also enhancing the spin-forbidden processes. This effect can be observed in complexes with transition metals as in the works presented in the OLED phosphorescent section. Besides that, the heavy atom effect can also be achieved with non-metal atoms, such as bromine, iodine, selenium or tellurium, for example.[43,45] Another strategy that can be adopted is the incorporation of atoms with lone electron pairs, such as oxygen, nitrogen, sulphur or phosphorus, for example.[46]

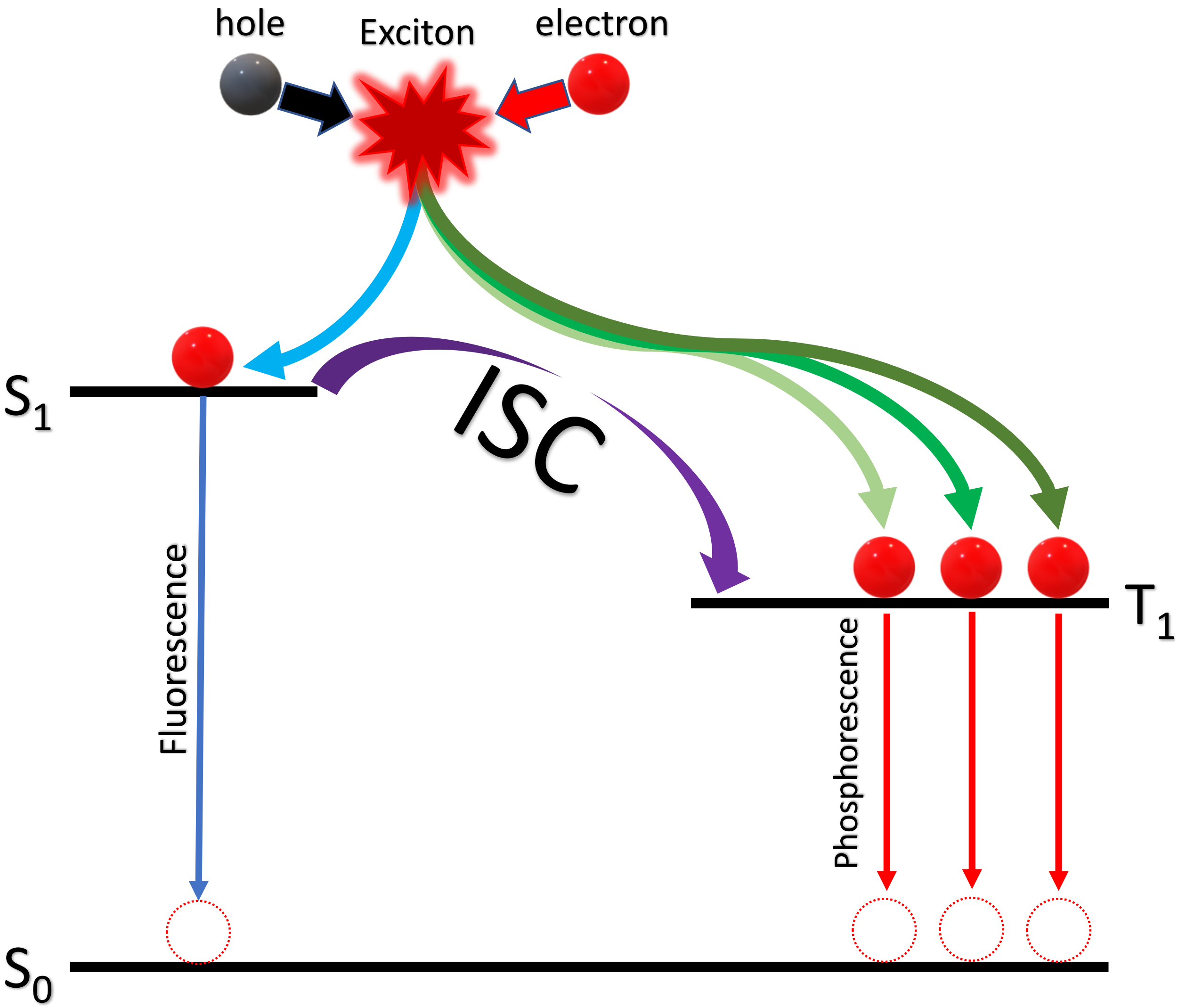

Figure 17. Electrical excitation of a phosphorescent emitter and the possible decay pathways.

2.3.3. Thermally activated delayed fluorescence (TADF)

Thermally activated delayed fluorescence (TADF) occurs when the molecule can up-convert T_1 to the S_1 states intramolecularly, through the thermal energy of the surrounding matter in a process called reverse intersystem crossing (RISC).[47] RISC is active when the molecule displays a small energy difference between S_1 and T_1 states (ΔE_{ST}), usually smaller than 0.3 eV. Small ΔE_{ST} is necessary to obtain fast k_{RISC} (although not the only factor). The most popular way to achieve small ΔE_{ST} is good separation between the highest occupied molecular orbital (HOMO) and the lowest unoccupied molecular orbital (LUMO).[48–50] An easy way to obtain such separation is by using molecules with electron donor (D) and acceptor (A) moieties. These structures display a charge transfer (CT) character of singlet and triplet excited states.[37,51,52] However, RISC is not directly dependent on ΔE_{ST} when the singlet and triplet excited states assume a charge transfer character (or generally the same character).[51] In this case the SOC between triplet and singlet states of the same orbital character is zero, and the k_{RISC} is not inversely proportional to ΔE_{ST}.[53] RISC is thus enhanced with the vibrionic coupling between locally excited triplet (^{3}LE) and charge transfer triplet (^{3}CT).[51] In other words, a higher k_{RISC} can be achieved with a second triplet excited state with an LE character participating when the first triplet and the first singlet excited state have a CT character.[51]

At lower temperatures, the TADF emission is quenched and the emission of phosphorescence at low temperatures becomes the dominant process.[54] In fact, phosphorescence and TADF can be understood as competitive processes where both compete for electrons of the triplet excited state.[55] What will determine which dominates and is more pronounced is the relationship between k_{RISC}, k_{ISC}, and k_P.[55] It is typical to observe the transition from TADF to phosphorescence upon a decrease in temperature: at lower temperatures phosphorescence dominates, while at high temperatures TADF dominates. The TADF mechanism is explained in detail in **Figure 18**. k_{RISC} can be calculated by the following equation.[6]

$$k_{RISC} = \frac{\phi_{RISC}}{\tau_{DF}}\left(\frac{\phi_{PF}+\phi_{DF}}{\phi_{PF}}\right) \qquad (2)$$

Where ϕ_{PF} is the prompt fluorescence quantum yield, ϕ_{DF} is the delayed fluorescence quantum yield and τ_{DF} is the lifetime of the delayed fluorescence. When the ratio between

DF/PF is close or higher than 4 the ϕ_{RISC} approaches 1 and equation 4 becomes equation 5.[6]

$$k_{RISC} = \frac{1}{\tau_{DF}}\left(\frac{\phi_{PF}+\phi_{DF}}{\phi_{PF}}\right) \qquad (3)$$

The ratio of DF/PF can be expressed by amplitude of emission decay (A) multiplied by the lifetime (τ) of the emission as shown in equation 4.[6]

$$\frac{\phi_{DF}}{\phi_{PF}} = \frac{A_{DF}\,\tau_{DF}}{A_{PF}\,\tau_{PF}} \qquad (4)$$

The k_{TADF} can be also determined by the following equation:

$$k_{TADF} = \frac{1}{3} k_{PF}\, exp\left[\frac{-\Delta E_{ST}}{k_b T}\right] \qquad (5)$$

Where the k_{PF} is the rate constant of prompt fluorescence; k_b is the Boltzmann constant; T is temperature and ΔE_{ST} is the energy difference between the singlet and triplet excited states.[56]

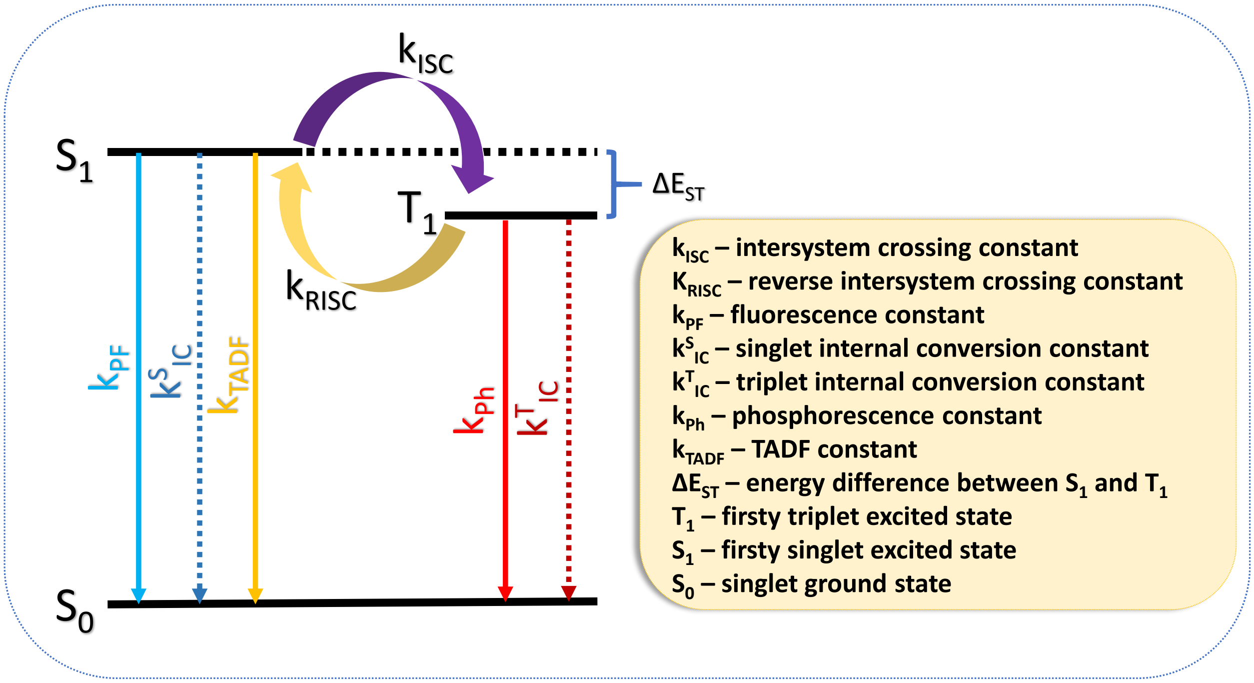

Figure 18. The constants involved in TADF emission process.

The TADF molecules behave somewhat similarly to phosphorescent emitters when in OLEDs as also able to achieve 100 % IQE due to harvesting triplet excited states through the S_1 manifold. See **Figure 19** and **Figure 20** show a simplified Jabłoński diagram representing a typical TADF emitter excited electrically.[57]

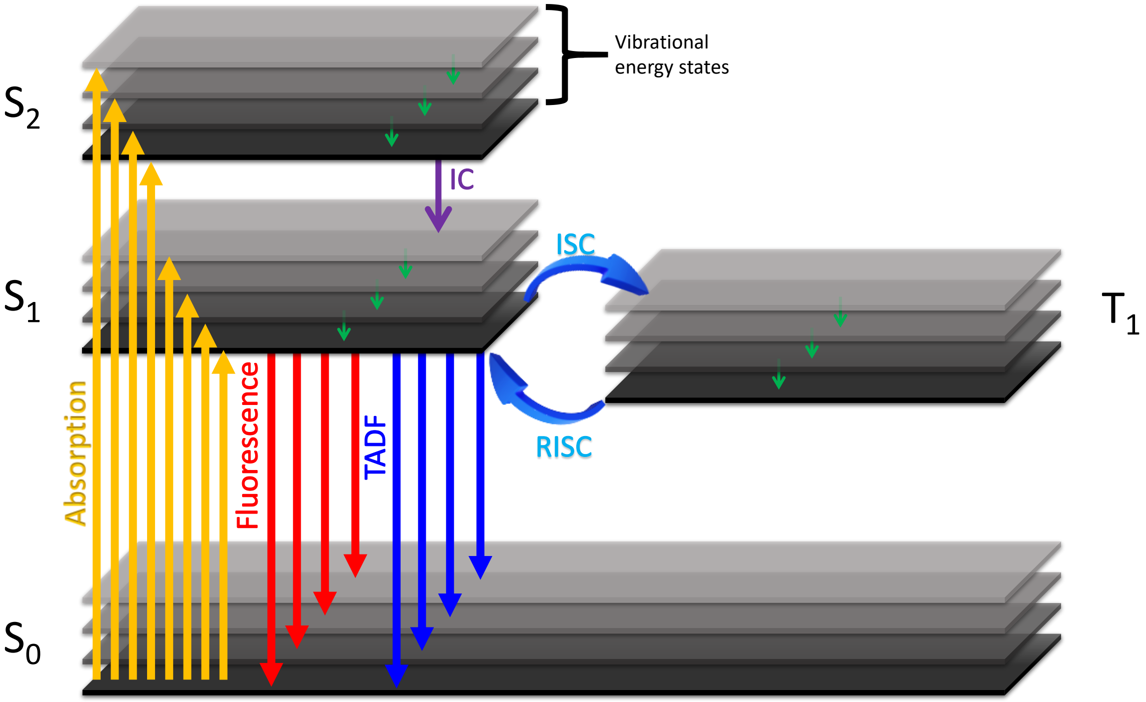

Figure 19. Jabłoński diagram of a typical TADF emitter.

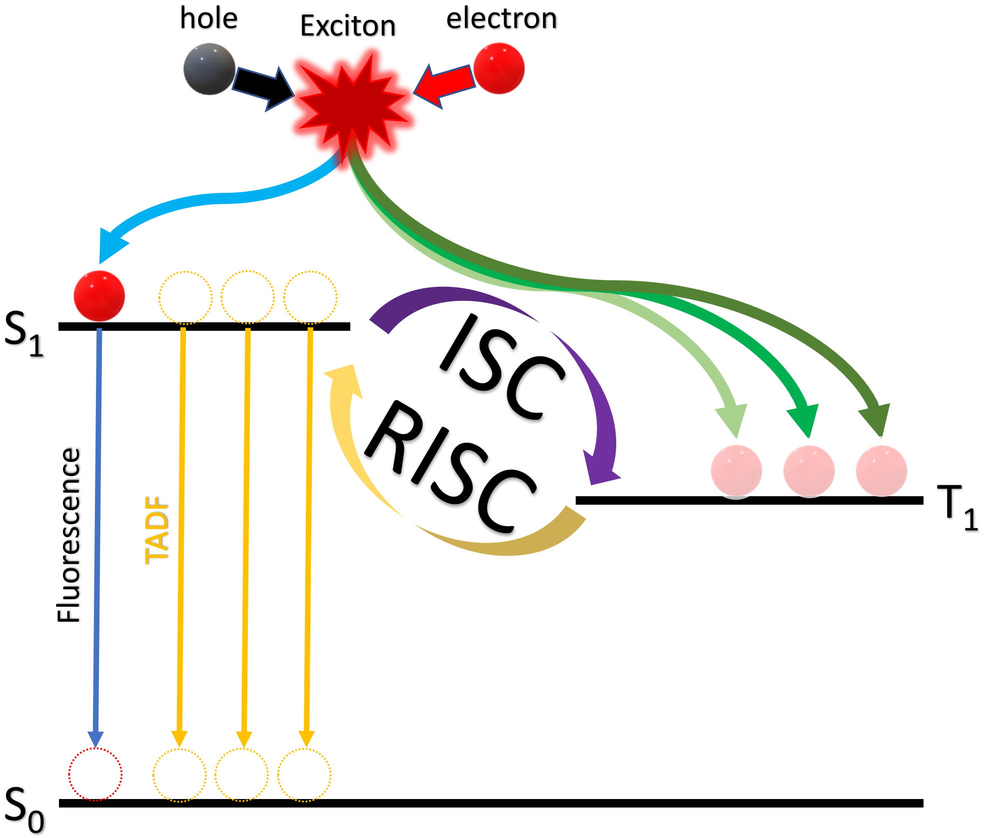

Figure 20. The behaviour of an electrically excited TADF emitter.

2.3.4. Quenching processes

Many phenomena can affect TADF and RTP emitters, such as the presence of oxygen or other quenchers, triplet-triplet annihilation (TTA), singlet-singlet annihilation (SSA), and singlet-triplet annihilation (STA), for example.[51,58–60] Furthermore, molecular oxygen (O_2) displays a triplet ground state.[61] O_2 molecule interacts with the T_1 states of the emitters quenching them. The molecule of oxygen undergoes from its triplet ground state ($^3O_2$) to the singlet excited state ($^1O_2$) via the Dexter electron transfer process, while the luminophore returns to the singlet ground state, as depicted in **Figure 21**.[61] This affects all photoluminescence that has an origin in the triplet excited state.

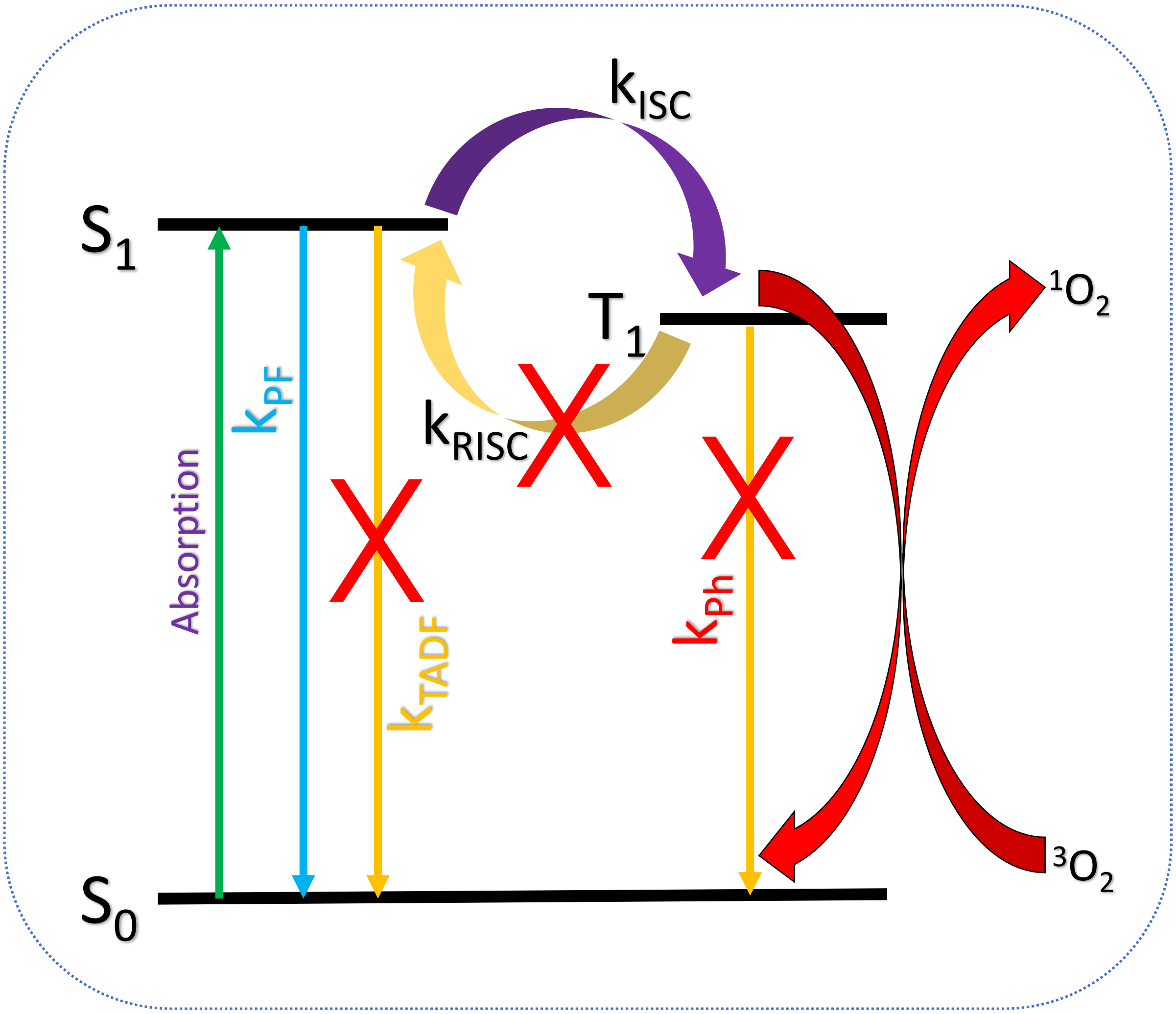

Figure 21. Quenching caused by oxygen in TADF/RTP emitters.

The second quenching mechanism discussed in this thesis is TTA. TTA is not a fully quenching process, but it leads to a reduction of the overall number of excited states. In simple terms, TTA is a process where two triplets interact forming one singlet excited state and a ground state, $T_1 + T_1 \rightarrow S_1 + S_0$.[58] This mechanism allows to generate excited singlet states by consuming two triplet states to form one singlet state, hence it gives a maximum efficiency of 50% of triplet stats. Due to OLED spin statistics, the maximum IQE possible in TTA OLEDs is 62.5 %, with 25 % originating directly from the S_1 state and an additional 37.5 % coming from the TTA mechanism from the 75 % triplet excited states produced.[58] In that way this mechanism also contributes to lowering the efficiency of OLEDs, at least in comparison with TADF and RTP materials, however, it yields higher efficiency than fluorescent emitters.

Besides the TTA mechanism, the singlet excited state also can participate in annihilation processes with another singlet or with a triplet.[62,63] Probability of these processes taking place increases with the excitation power which increases the number of molecules in the excited state at once.[62,63] Singlet-singlet annihilation occurs when two singlet excitons form an upper singlet excited state (S_n) and a ground state. The S_n state then returns to the S_1 by internal conversion.[63] Singlet-triplet annihilation state occurs when two molecules, one in singlet and another one in triplet excited state, interact resulting in a singlet ground state and an upper triplet excited state (T_n) that returns to T_1 by internal conversion.[62]

3. Methodology

3.1. Cyclic Voltammetry

Cyclic voltammograms were conducted using a 2 mL electrochemical cell employing a three-electrode setup, including a working electrode (platinum disc), a reference electrode (silver wire), and a counter electrode (platinum wire). The electrolyte used was tetrabutylammonium tetrafluoroborate at a concentration of 100 mM in dichloromethane (DCM). The potentiostat employed was the PGSTAT100N by AUTOLAB. Analytes were examined in 1 mM solutions. To calibrate the reference electrode, ferrocene was used as the standard. Ionization potential was correlated with the HOMO, and electron affinity was linked to the LUMO, both of which were determined from the onset oxidation and reduction potentials, respectively, and the equation used for that was:

$$E_{(HOMO\ or\ LUMO)} = -(5.1 + E_{oxidation\ \ or\ reduction})$$

3.2. UV-Vis spectrophotometry

Absorption spectra were recorded with solutions of analytes at concentrations between 1×10^{-4} and 1×10^{-5} M and in various solvents: dichloromethane (DCM), tetrahydrofuran (THF), toluene (TOL), methylcyclohexane (MCH), and acetonitrile (ACN). Shimadzu UV-2550 spectrophotometer was used for recording UV-Vis spectra. The results were obtained as text files and analysed in Origin software by plotting absorbance *vs.* wavelength. Absorption coefficients were extracted using Lambert-Beer law:

$$A = dc\varepsilon$$

Where A is absorbance, d is the optical path (cm), c is the molarity (M) of the solution and ε is the molar absorption coefficient ($M^{-1}cm^{-1}$).

3.3. Spectrofluorimetry

3.3.1. Photoluminescence in solution

The emission properties of derivatives were investigated with solutions at c = 1×10^{-4}, 1×10^{-5}, and 1×10^{-6} M in various solvents like DCM, THF, TOL, MCH, and ACN. Direct photoluminescence quantum yield (PLQY) in solution was recorded using an integration sphere with the same solution concentration. Analysis in degassed solution, which is without oxygen, was performed using the same solution concentration and using a special cuvette (**Figure 22**) with a round flask. The freeze-pump method was used for removing dissolved gas (including oxygen) by evacuating the cuvette with a solution cooled to 77 K, using a vacuum pump, which retains the original concentration of the solution. Photoluminescence spectra were recorded before and after removing the oxygen for comparison. The increase of the photoluminescence intensity is obtained as a ratio of areas under the emission spectra after and before degassing. The analysis of steady-state emission was carried out using a FluoroSens spectrofluorometer. The studies used clean 1 cm optical path photoluminescence cuvettes (Aireka Cells). Photoluminescence spectra were calibrated for detector efficiency using company-supplied, instrument-specific calibration files.

Figure 22. Special quartz cuvette for solution degassing used in photoluminescence studies in solutions.

3.3.2. Photoluminescence in film

The emission spectra in the solid state were recorded using films of 1 % of the luminophore in Zeonex as well as 10 % in CBP OLED hosts. Films were deposited on a sapphire disc with a diameter of 12 mm. These films were analysed in the same fluorimeter used for solutions with proper support to hold the sapphire. Determination of PLQY was undertaken using an integrating sphere with the host matrix as a blank film. The effect of oxygen on steady-state photoluminescence was studied in a sample holder of a cryostat in air and at vacuum.

3.3.3. Time-dependent photoluminescence analysis

Time-dependent photoluminescence analysis was carried out with an iCCD camera coupled with a cryostat with a high vacuum pump and an Nd:YAG laser with a 10 Hz pulse to excite the sample with its 3rd harmonics at 355 nm. The temperature was variated in the range between 10 K and 300 K and the delay time was within a range of 0 ns until 80 ms. This analysis allows us to record the S_1 and T_1 energies from fluorescence and phosphorescence spectra as well as to conduct spectral analysis of the emission in function of time. **Figure 23** shows the equipment setup.

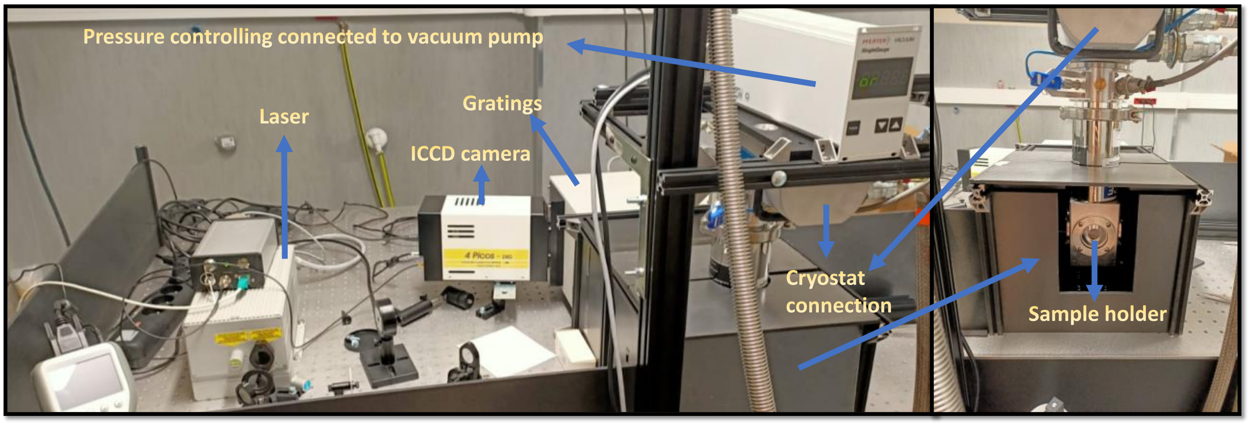

Figure 23. Setup to the time dependence spectroscopy analysis.

The samples were prepared by drop or spin-coating of a solution containing 1 % of the compound in Zeonex or 10 % of the compound in CBP in a sapphire as substrate. The energies of the first singlet excited state (S_1) and first triplet excited state (T_1) were obtained by the onset emissions of prompt fluorescence and phosphorescence at low temperatures and with that the value of ΔE_{ST} for each compound in two different matrices, Zeonex and CBP.

3.3.4. OLED devices fabrication

OLEDs have been fabricated with an indium-tin-oxide (ITO) coated glass substrate with a sheet resistance of 20 Ω/sq and ITO thickness of 100 nm. PEDOT:PSS {poly(3,4-ethylenedioxythiophene) polystyrene sulfonate} was used as a Hole Injection Layer (HIL) and Hole Transport Layer (HTL). TPBi {2,2',2"-(1,3,5-benzinetriyl)-tris(1-phenyl-1-*H*-benzimidazole)} was introduced as an Electron Transport Layer (ETL). Lithium fluoride (LiF) and aluminium were used as the electron injection layer (EIL) and cathode, respectively. TPBi and aluminium were deposited at a rate of 1 Å s^{-1}, and the LiF layer was deposited at 0.1 Å s^{-1}. CBP {4,4′-bis(*N*-carbazolyl)-1,1′-biphenyl}, was used as a host for all emitters. All materials were purchased from Sigma Aldrich or Lumetec and were purified by temperature-gradient sublimation in a vacuum. PEDOT:PSS layer was prepared on an ITO-coated glass substrate by spin coating of the solution at 4000 rpm and 45 s with 15 minutes of annealing treatment at 120 °C after deposition. The emissive layers were prepared by spin-coating a solution of 95:5 m/m of chloroform and chlorobenzene with 10 % of emitter compounds in CBP (host) at 4000 rpm and 45 s. All other molecules and cathode layers were thermally evaporated using a Kurt J. Lesker NANO 36 evaporation system under pressure of 10^{-7} mbar without breaking the vacuum. The sizes of pixels were 4 mm^2, 8 mm^2 and 16 mm^2. The characteristics of the devices were recorded using a 6-inch integrating sphere (Labsphere) connected to a Source Meter Unit and Ocean Optics USB4000 spectrometer.

3.3.5. Singlet Oxygen analyses

Singlet oxygen experiments were carried out in a quartz cuvette (Hellma Analytics) with a 10 mm path using DCM solutions of 0.016 mM photosensitizers and 0.13 mM of tetraphenylcyclopentadienone (TPCPD) as the specific singlet oxygen trap. Temporal changes in absorbance of TPCPD at $\lambda = 510$ nm were monitored while using the irradiation beam, $\lambda = 445$ nm, with a *ca*. 0.5 cm^2 cross section in perpendicular configuration to the UV-Vis spectrometer optical path. A diode laser with an emission wavelength of 445 nm (Oxxius 100 mW model LBX-445-100-CSB-PP) working at 20 mW was applied as a source of light. The equation used to calculate singlet oxygen formation (ϕ_Δ) was:

$$\phi_{\boldsymbol{\Delta}} = \phi_{\boldsymbol{PN}}.\frac{\boldsymbol{k_i}}{\boldsymbol{k_{PN}}}.\frac{\boldsymbol{\alpha_{PN}}}{\boldsymbol{\alpha_i}}.$$

Where $\boldsymbol{\phi_\Delta}$ is the quantum yield of singlet oxygen formation, $\boldsymbol{\phi_{PN}}$ is the singlet oxygen quantum yield for phenalenone (PN) (0.95 in DCM)[64,65], $\mathbf{k_i}$ is the slope of temporal change in absorbance of TPCPD, $\mathbf{k_{PN}}$ is the slope of temporal change in absorbance of TPCPD and $\boldsymbol{\alpha_i}$ is a function of absorbance at 445 nm, $\alpha = (1 - 10^{-A})$.

4. Compounds analyzed in this thesis

Systematic modifications in acceptor and donor moiety were investigated to better understand the influence of molecular structure on TADF and RTP properties. The modification in acceptor cores includes isomeric structures used for evaluation of the properties in response to small modifications in D-A and D-A-D structures. Besides that, the influence of a methyl group in the phenyl bridge or in the donor moiety was evaluated in a system of the form $(D\text{-}Ph)_3\text{-}A$. A full description of molecules is presented in each of the following chapters, including a discussion of their structural variation. As discussed in the introduction, the development of new luminophores is essential to improve the understanding of the structure-property relationships as well as the performance of such emitters in OLEDs. The derivatives that were investigated in this work were synthesised by partners from the Silesian University of Technology (SUT), Gliwice, Poland and from Osaka University, Osaka, Japan. The origin of the samples in each case is indicated at the beginning of every chapter.

4.1. [1,2,3]triazolo[4,5-b]pyridine isomers (PyBTA-1, PyBTA-2 and PyBTA-3)

These molecules were synthesized by Dr Leandro Espíndola and Mr Welisson de Pontes Silva. The [1,2,3]triazolo[4,5-b]pyridine cores were designed and studied in three different isomeric forms to understand the importance of the position of the acceptor methyl group on the photophysics of these derivatives. Besides that, this core was not studied before in TADF and/or RTP luminophores. Three different positional isomers of the brominated acceptor core were obtained: 6-bromo-3-methyl-3*H*-[1,2,3]triazolo[4,5-b]pyridine, 6-bromo-2-methyl-2*H*-[1,2,3]triazolo[4,5-b]pyridine, and 6-bromo-1-methyl-1*H*-[1,2,3]triazolo[4,5-b]pyridine. These were then coupled with **PTZ**, **PXZ** and **DPA**, donors, resulting in a total of 9 molecules shown in **Figure 24**.

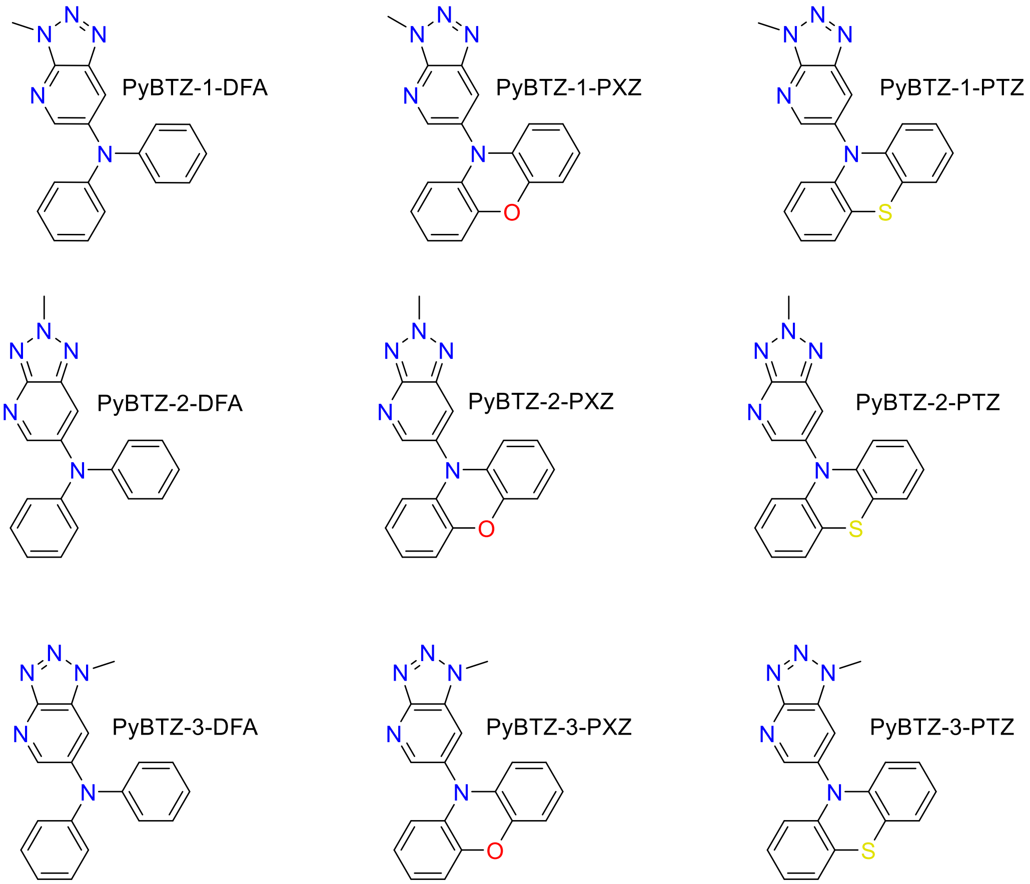

Figure 24. Donor-acceptor molecules based on isomeric [1,2,3]triazolo[4,5-b]pyridine derivatives synthesized by Dr Leandro Espíndola and Mr Welisson de Pontes Silva.

4.2. Acenaphtopyrido[2,3-b]pyrazine compounds

These molecules were synthesized by Dr Leandro Espíndola and Mr Welisson de Pontes Silva. The derivatives of acenaphtopyrido[2,3-b]pyrazine (**NQPy**) have been studied before, however not as in-depth as presented in this thesis.[66] New D-A molecules based on the **NQPy** acceptor core were produced with the idea of completing this previous work by focusing on the analysis of the structure-property relationships resulting from the use of different donors. These donors were: phenothiazine (**PTZ**), phenoxazine (**PXZ**), dimethylacrydine (**DMAC**), diphenylacrydine (**DPAC**), diphenylamine (**DPA**), carbazole (**CBZ**), dihydrodibenzoazepine (**DDA**) and dibenzoazepine (**IMD**). The structures of the D-A molecules are shown in **Figure 25**. Due to the long-lived triplet states these compounds were good candidates to work as a photosensitizer in singlet oxygen generation. Besides that, some of these compounds showed aggregation-induced emission (AIE) or aggregation-induced emission enhancement (AIEE).

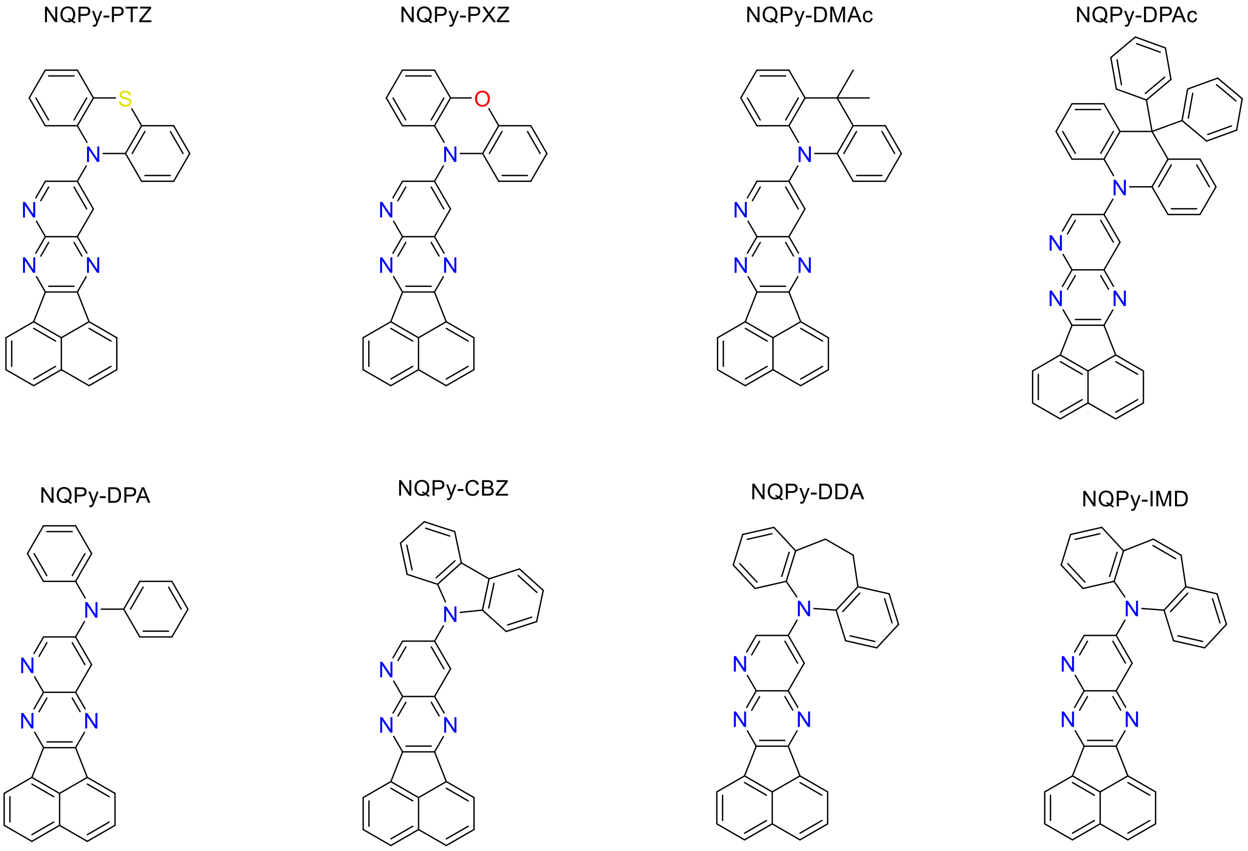

Figure 25. Acenaphtopyrido[2,3-b]pyrazine derivatives synthesized by Mr Welisson de Pontes Silva with the help of Dr Leandro Espíndola.

4.3. Tris([1,2,4]triazolo)[1,3,5]triazine (TTT) compounds

The **TTT** derivatives, **Figure 26**, were designed and synthesized by Dr Marli Ferreira. They were derived from the acceptor core tris([1,2,4]triazolo)[1,3,5]triazine (**TTT**). Structural changes were introduced, more specifically by addition of methyl groups in the phenyl spacers that link the D and A units and in the donor. The presence or absence of methyl groups provides control over steric hindrance favouring either TADF or RTP properties. These derivatives also showed aggregation properties with the AIEE effect being relatively pronounced.

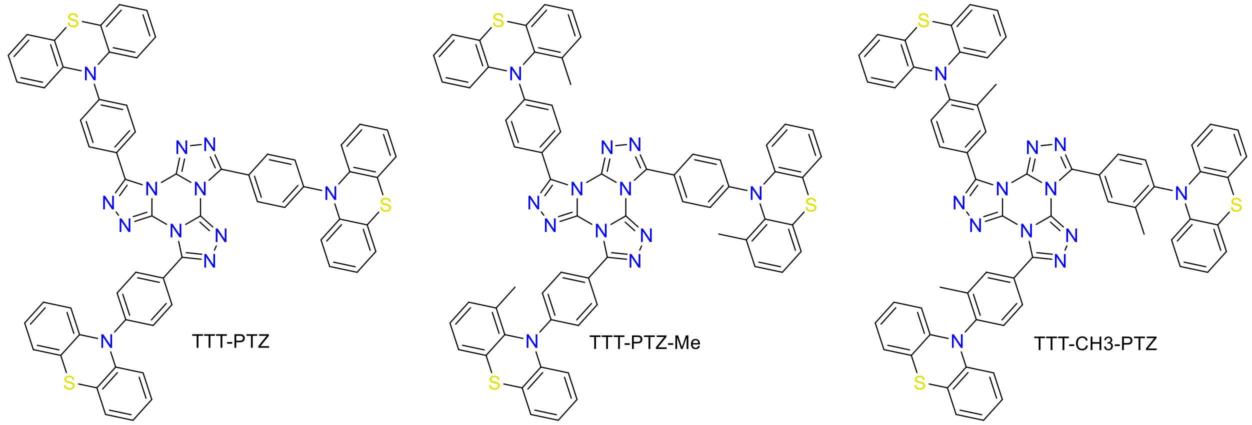

Figure 26. **TTT** derivatives synthesized by Dr Marli Ferreira.

4.4. Dibenzo[a,j]phenazine compounds (JAP)

Professor Youhei Takeda's group from the University of Osaka in Japan synthesized various derivatives of dibenzo[a,j]phenazine (**JAP**) by changing the type and position of donors in the acceptor core forming regioisomers 2,12 and 3,11. The dibenzo[a,j]phenazines were described in the literature as a versatile core developed by professor Takeda and his group. These molecules are presented in **Figure 27**. The compounds were analysed by the comparison of the regioisomers and the different donors.

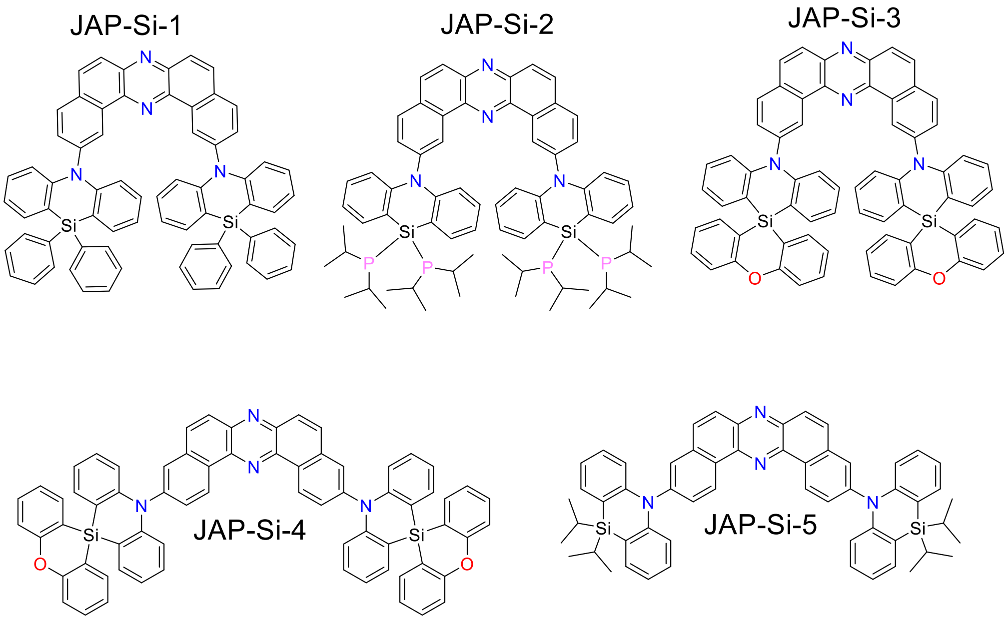

Figure 27. Dibenzo[a,j]phenazine derivatives synthesized by Takeda's research group.

5. Results

In this work were studied selected newly developed donor-acceptor derivatives based on four different acceptor cores. Photoluminescent properties of these systems were characterized and they were applied as emitters in OLED devices. The photophysical investigations were done by using an iCCD camera and a pulse laser to record time-resolved photoluminescence spectra and luminescent decays. Besides that, the utilization of a cryostat permitted the variation of temperature what helped to identify important parameters of the samples as triplet energies and temperature dependence of the luminescent decay (TADF and RTP). Another parameters that were evaluated using this equipment were ratio between prompt and delayed fluorescence, an important parameter which can be used to calculate k_{RISC}. The analyses performed in two solid matrices were made to evaluate the influence of a non-polar and a polar matrix on the emission properties. The polar matrix stabilizes CT excited states and can influence photophysical parameters of charge transfer luminophores. After the full characterization, the compounds were applied as emissive layers in solution processed OLED devices. These devices were manufactured and analysed for most of the TADF and RTP emitters presented in this thesis. Besides that some of the compounds present a plethora of various additional characteristics, including AIE and AIEE as well as singlet oxygen generation. Thanks to the systematically designed emitter structures it was possible to study in depth the structure-property relationships of the TADF and RTP emitters, advancing the overall knowledge in the topic. Hence, aiding future emitter design for tailored applications.

5.1. Triazolopyridine derivatives (PyBTA-1, PyBTA-2 and PyBTA-3)

The draft of this chapter is in preparation to submission to the Journal of Materials Chemistry C. The title of the manuscript is “Tailoring TADF Properties: A comprehensive analysis of isomerism in [1,2,3]triazolo[4,5-b]pyridine compounds for enhanced OLED performance and beyond”.

N-rich structures are a good approach for development of new cores to achieve TADF properties. Higher electronegativity of nitrogen in relation to carbon makes the acceptor stronger.[67] In addition, the D-A structure is usual to obtaining well separated HOMO and LUMO orbitals resulting in low ΔE_{ST}, as discussed in the introduction.[52] Besides that, benzotriazoles and [1,2,3]triazolo[4,5-b]pyridines in the TADF field are not yet fully described and understood. In fact, to the best of my knowledge, no publications involving triazolo[4,5-b]pyridine and TADF was published until the date of submission of this thesis. This core after methylation showa a fixed asymmetry resulting in three different isomers, called here as **PyBTA-1**, **PyBTA-2** and **PyBTA-3**. These three isomers can show different properties due to the conjugation with the D-A that is different for each isomer. The compounds **PyBTA-x-Donor** developed in our research group are showed in **Figure 24**. These derivatives have been designed to understand the positional isomerism in the TADF/RTP properties for three different donors. These positional variations are related to the methyl group in relation to the donor group added in the core. The relative position of the pyridinic nitrogen remains constant. The changes in the position of the methyl group in the **PyBTA-1**, **PyBTA-2** and **PyBTA-3** cores have been sufficient to cause a significant difference in the final properties of the compounds. Even though this change looks like a small modification, it visibly modulates the strength of the acceptor part and affects conjugation along of the whole molecule. Resonance structures for these three derivatives are shown in **Figure 28**.

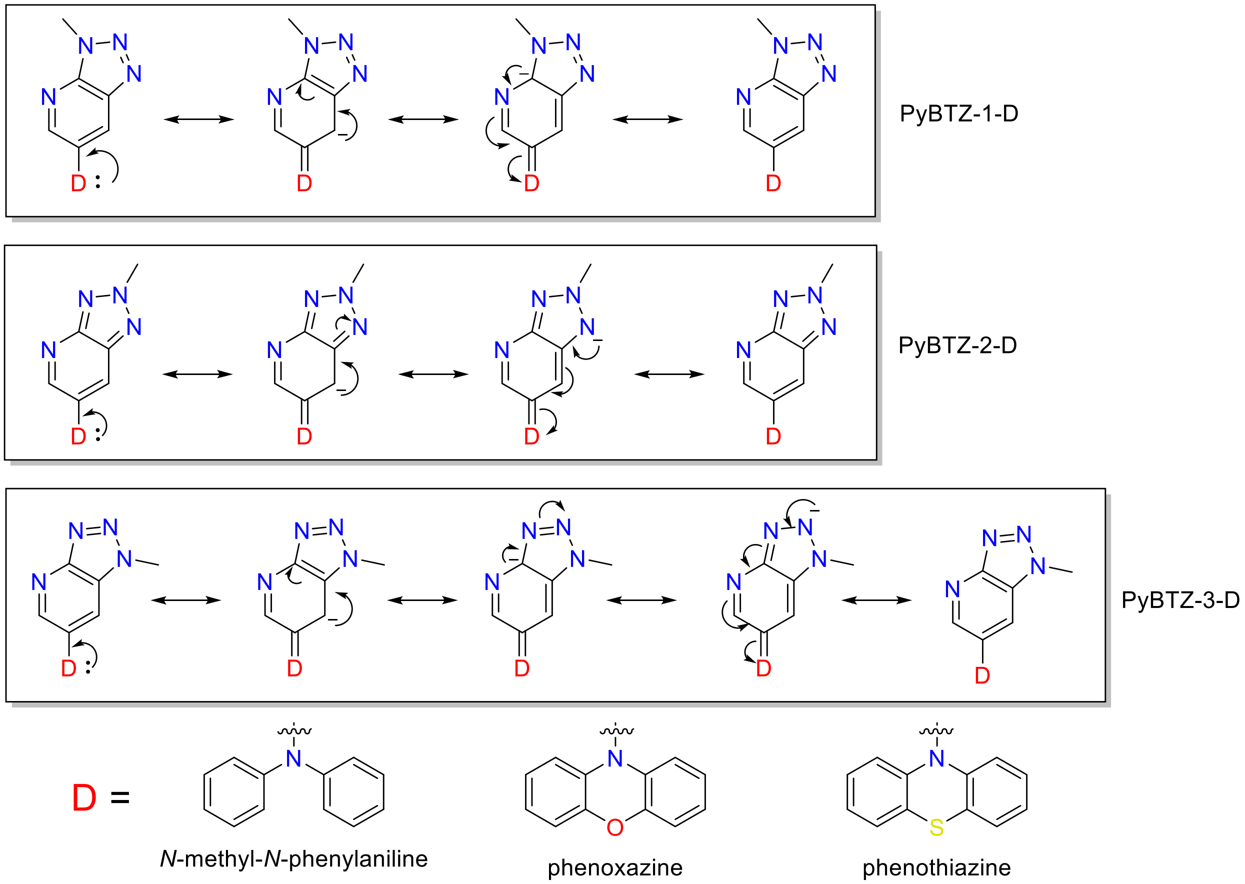

Figure 28. Resonance structures of **PyBTA-1**, **PyBTA-2** and **PyBTA-3**.

5.1.1. Cyclic Voltammetry (CV)

The CVs for the molecules with [1,2,3]triazolo[4,5-b]pyridine core (**PyBTA-1**, **PyBTA-2** and **PyBTA-3**) are shown in **Figure 29-A**, **B** and **C**. In first case, for the diphenylamine (**DPA**) as donor, it is possible to see the higher oxidation potential was observed for the isomer 2 (**PyBTA-2**) followed by the isomer 3 (**PyBTA-3**) and then the isomer 1 (**PyBTA-1**). While the oxidation potential with donors **PTZ** and **PXZ** changed in the following order: **PyBTA-3** > **PyBTA-2** > **PyBTA-1**. Looking at the reduction potential it is possible to observe the lower value for isomers **PyBTA-3** < **PyBTA-1** < **PyBTA-2** for **DPA** derivatives. Again, **PTZ** and **PXZ** derivatives have shown a different behaviour than the molecules with the **DPA** donor. The reduction potential for **PTZ** and **PXZ** derivatives changes in the isomer order of **PyBTA-1** < **PyBTA-3** < **PyBTA-2.** The bar plot shown in **Figure 30** represents all HOMO and LUMO energies compared to the OLED electrode work functions. We observe that **PyBTA-2** displays the largest acceptor strength. This is evidenced by the lowest LUMO in of these compounds having a higher electron affinity what means that they can receive an electron more easily than the other isomers.[68]

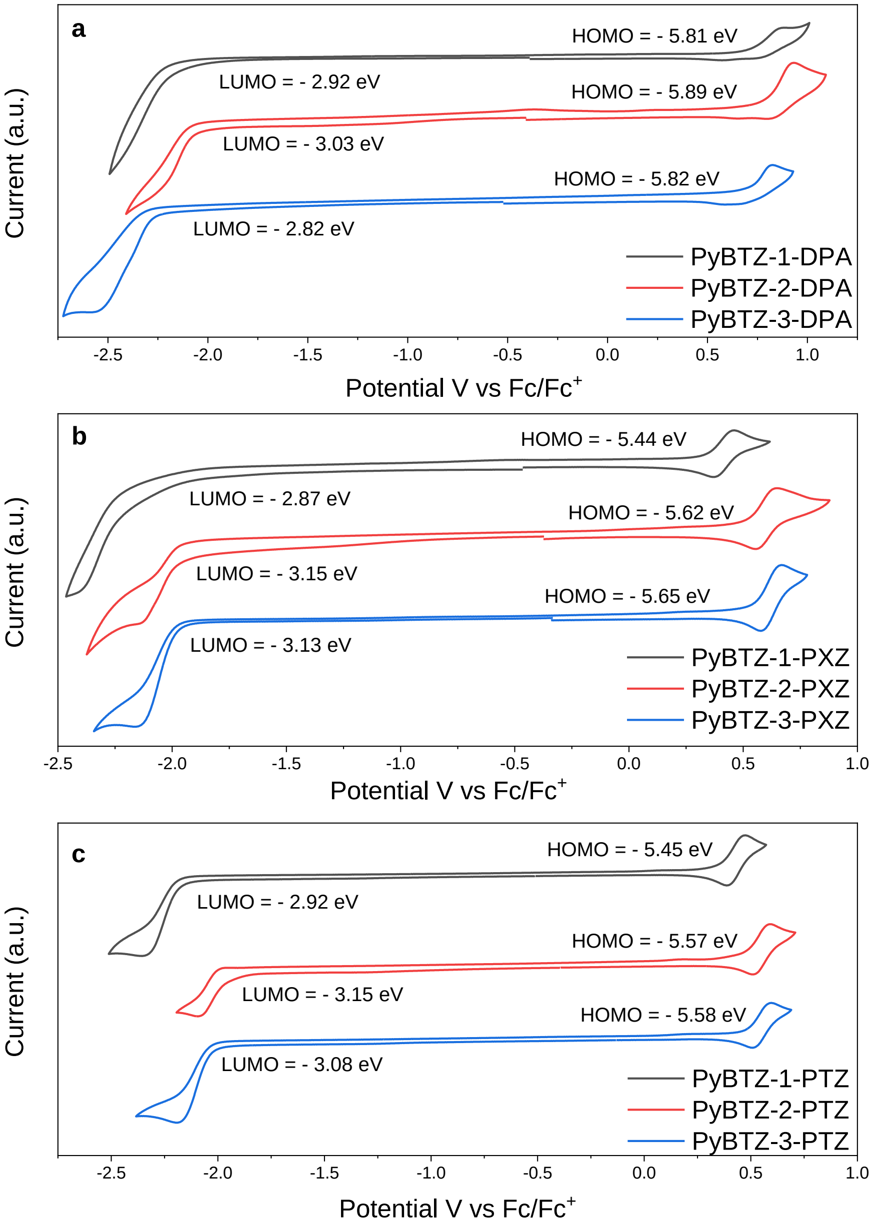

Figure 29. Cyclic Voltammetry of 1 mM of compounds in 0.1 M of tetrabutylammonium tetrafluoroborate in DCM A) **PyBTA-1-DFA**, **PyBTA-2-DFA** and **PyBTA-3-DFA**. B) **PyBTA-1-PXZ**, **PyBTA-2-PXZ** and **PyBTA-3-PXZ**. C) **PyBTA-1-PTZ**, **PyBTA-2-PTZ** and **PyBTA-3-PTZ**.

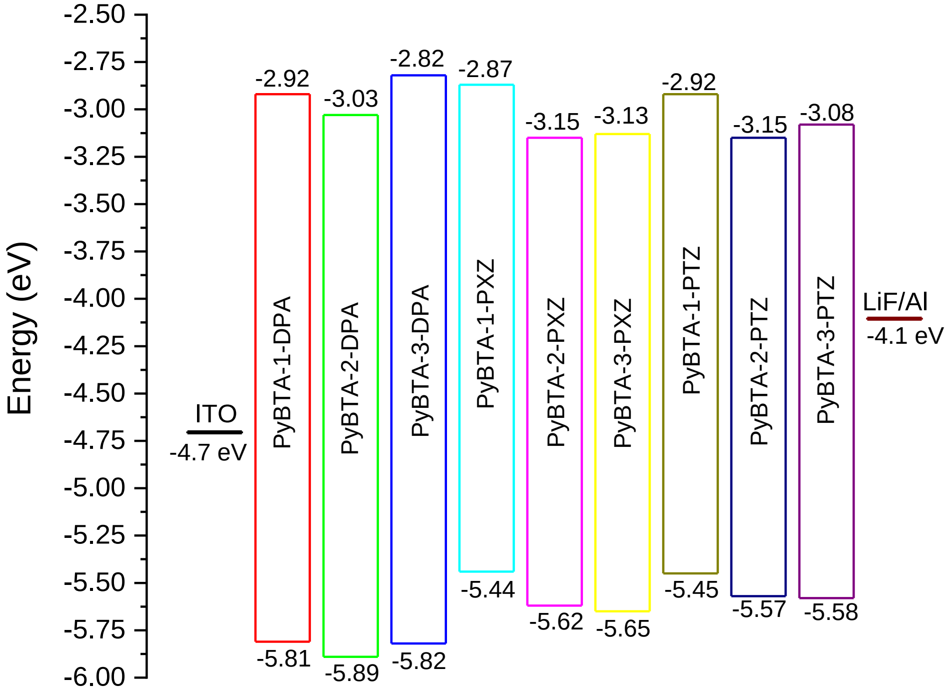

Figure 30. Bar plot of HOMO and LUMO energies for all **PyBTA** compounds compared with ITO and LiF/Al.

5.1.2. Steady state spectroscopy in solution

Absorption and photoluminescence spectra of the studied molecules are shown in **Figure 31**. They present three distinctive absorption bands with the energetically lowest band attributed to a charge transfer (CT) transition, see numerical data shown in **Table 1**. The **PyBTA-x-DPA** derivatives display strong CT absorption bands, ε = 7000 M^{-1} cm^{-1}, while for **PyBTA-x-PXZ** and **PyBTA-x-PTZ** the CT bands are weak, ε = 800 M^{-1} cm^{-1} and ε = 500 M^{-1} cm^{-1}, respectively, and even difficult to identify in some cases. It is possible to observe a different redshift in the absorption CT band depending of the donor. For the **DPA** donor the absorption band of the isomers showed a red shift with wavelengths in the order of **PyBTA-3** < **PyBTA-2** < **PyBTA-1**. On the other hand, for the **PXZ** derivatives the absorption order is **PyBTA-1** < **PyBTA-3** < **PyBTA-2**. While that, the isomers with **PTZ** as donor showed a more complicated behaviour due to the presence of more than one CT band originated from two different conformations of **PTZ**, *quasi*-axial (ax) and *quasi*-equatorial (eq).[69] Authors often attribute the lower energy transition to the eq-eq conformers being the ax-ax the most energetic one.[70,71] Different from these works, the present molecules show just one donor with two possibilities ax or eq conformers. Gao and co-authors observed the formation of two crystals with a single PTZ donor system, revealing distinct ax and eq conformers. These conformers exhibited disparate prompt emissions in the solid state, with the eq conformation displaying a more pronounced redshift compared to the ax conformation what is in agreement with discussed before.[72]

Table 1. Photophysical properties of the **PyBTA-1,2,3-Donor** compounds in diluted solutions.

Compounds	λ_{abs}/nm [ε/10^{3}M^{-1} cm^{-1}]	$\lambda_{emis(DCM)}$/nm [PLQY/%]	$\lambda_{emis(Toluene)}$/nm [PLQY/%]
PyBTA-1-DPA	257, 290, 394 [11.8, 16.6, 4.16]	505[61.0]	467[62.0]
PyBTA-2-DPA	266, 283sh, 392 [18.1, 15.6, 7.1]	522[62.0]	478[74.0]
PyBTA-3-DPA	266, 291, 378 [16.6, 15.8, 9.2]	499[56.0]	458[79.0]
PyBTA-1-PXZ	295, 316sh, 411 [11.0, 8.3, 0.7]	-	553[2.7]
PyBTA-2-PXZ	288, 317sh, 423 [12.4, 6.0, 0.8]	-	576[1.7]
PyBTA-3-PXZ	285, 317sh, 416 [8.3, 5.3, 0.8]	-	549[5.3]
PyBTA-1-PTZ	256, 293, 319sh 391sh [28.6, 5.4, 2.1, 0.4]	472[0.1]	566[0.9]
PyBTA-2-PTZ	256, 288, 321sh, 382sh [23.7, 7.5, 1.9, 0.7]	474[0.1]	593[0.1]
PyBTA-3-PTZ	256, 286, 333, 414sh [18.4, 4.2, 1.6, 0.2]	461[0.1]	565[1.3]

The emission spectra are shown in **Figure 31**. All luminophores are emissive in both, TOL and DCM generally showing broadband spectra characteristic to CT states, except for the **PXZ** derivatives that do not present any emission in DCM. Interestingly, **PyBTA-x-PTZ** molecules as well as **PyBTA-1-DPA** to some extent display dual emission in DCM solvent, but a single emission band in TOL. This behaviour can be explained with the additional, higher energy emission arising from molecules with different donor conformers, as shown previously.[73] Looking at the emission in toluene it is possible to observe that the molecules with the isomeric acceptor **PyBTA-2** are the most redshifted among the three donors, followed by the isomer **PyBTA-1** and then the isomer **PyBTA-3**. That indicates the energy of S_1 state variety in the same isomer order *i.e.* **PyBTA-2** < **PyBTA-1** < **PyBTA-3**.

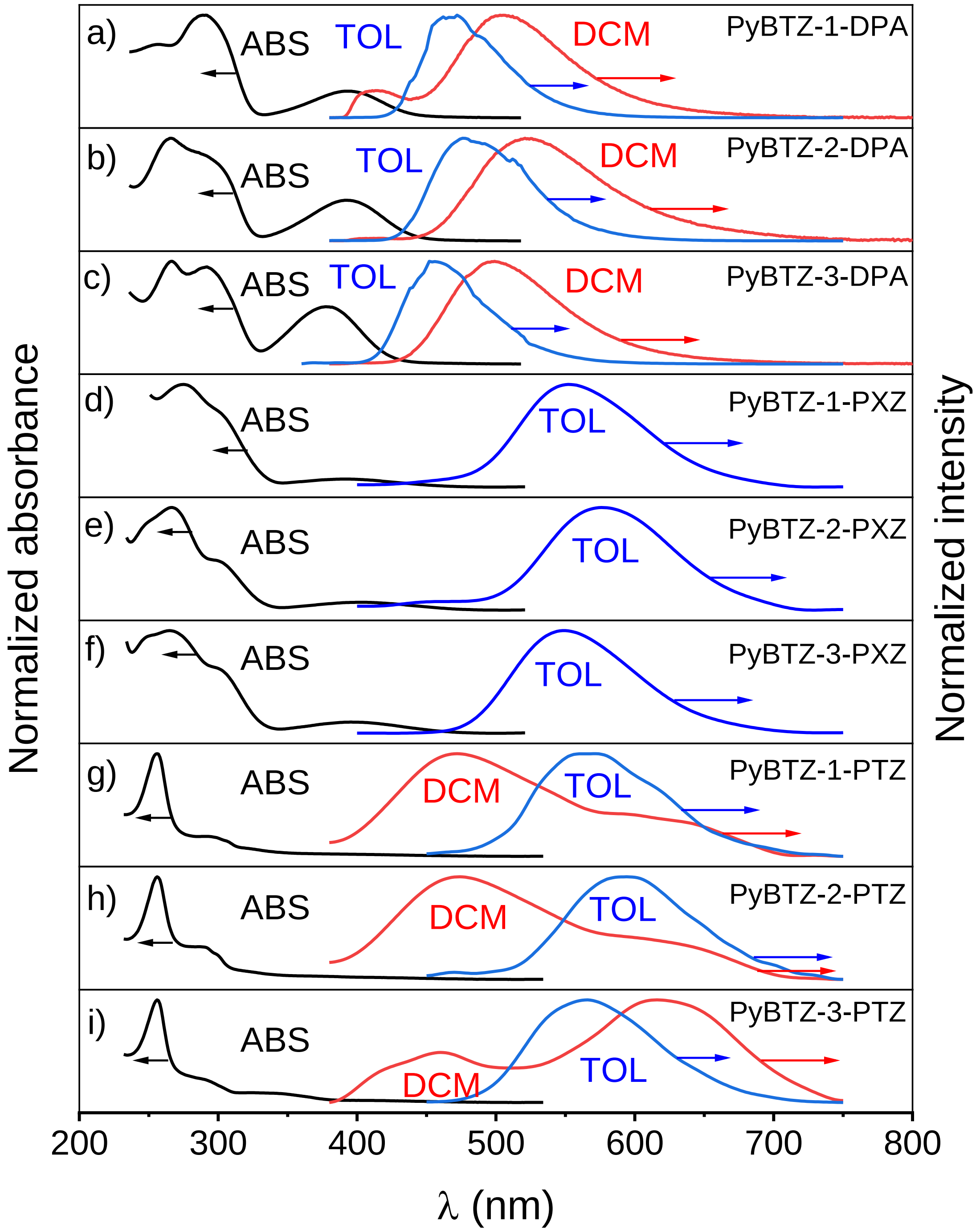

Figure 31. Absorption in DCM and emission in TOL and DCM of compounds **PyBTA-X-Donor** derivatives, c = 1×10^{-5} M.

5.1.3. Steady state photoluminescence in films

Photoluminescence in film are presented in **Figure 32**, while the numerical data are shown in **Table 2.** The results follow the same trend as in a solution for groups of molecules with different donors, but the differences between isomeric structures are much less pronounced. For **PXZ** and **PTZ** derivatives we observe a clear trend in solid state PL with the spectra red shifting in the order: isomer 1 < isomer 2 < isomer 3. At the same time all **PyBTA-x-DPA** molecules display a similar PL spectrum with little effect from the differences in acceptor. Besides that, the FWHM of the emission bands is showing a broader band for compounds in the order of isomer 3 > isomer 2 > isomer 1.

The analysis of PLQY has revealed its sensitivity to oxygen, attributed to quenching promoted by triplet oxygen, as mentioned previously. In this context, compounds that exhibited an increase in emission under vacuum conditions are those with triplet states contributing to the emission. By comparing the values presented in **Table 2**, it becomes evident that the most significant enhancements in emission occurred for isomer 1, followed by isomer 2, and then isomer 3, indicating a higher proportion of a delayed component in the same order. Notably, among the compounds, **PyBTA-1-PXZ** and **PyBTA-1-PTZ** stand out by achieving approximately 84 % and 57 % of PLQY in vacuum.

Table 2. Results of emission and PLQY for **PyBTA** derivatives.

	$\lambda_{emis(Zeonex)}$ max. (nm)	Increase*	PLQY (%)
PyBTA-1-DPA	448	1.18	448/50.6/60.0#
PyBTA-2-DPA	451	1.00	450/62.3/62.3#
PyBTA-3-DPA	446	1.00	446/51.1/51.1#
PyBTA-1-PXZ	507	2.62	509/32.0/83.7#
PyBTA-2-PXZ	522	1.83	522/26.4/48.2#
PyBTA-3-PXZ	535	1.44	535/13.2/19.0#
PyBTA-1-PTZ	520	6.16	520/9.2/56.6#
PyBTA-2-PTZ	525	1.60	526/15.2/24.3#
PyBTA-3-PTZ	546	1.55	546/8.3/12.8#

* Emission area without O_2 divided by area with O_2; # PLQY in Zeonex matrix increased by the vacuum conditions.

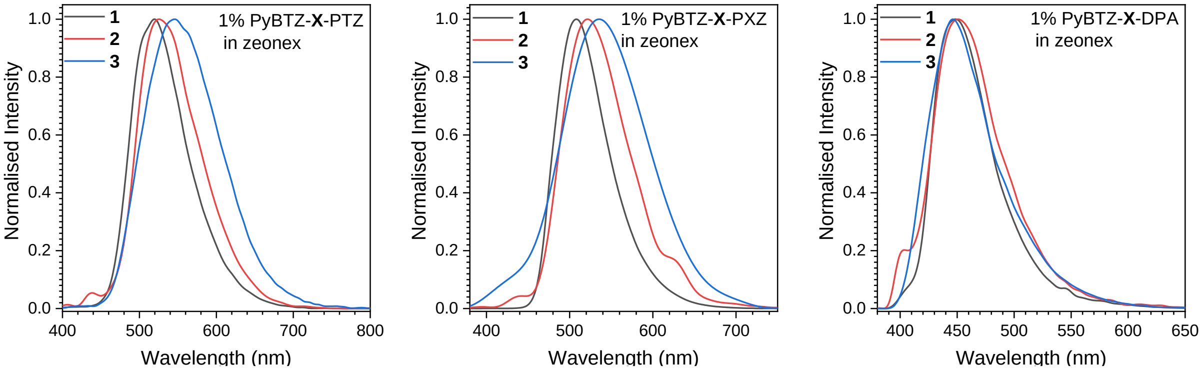

Figure 32. Emission of 1% of **PyBTA-X-Donor** compounds in Zeonex matrix.

5.1.4. Time-dependence analysis

All derivatives were studied by their emission in different delayed times between laser pulse and the iCCD camera. These analyses make it possible to extract important information about the final compounds as it is showed in the **Table 3**, that brings the values for each compound in two different matrices, Zeonex and CBP. The ΔE_{ST} of these compounds in Zeonex showed similar values for the first and second isomers (**PyBTA-1** and **PyBTA-2**) with the donors **PXZ** and **PTZ**, with the isomer 3 the one that presented the lowest values of ΔE_{ST} for both series of donors with **PTZ** and **PXZ**. The series of **DPA** showed a lower value of ΔE_{ST} for the first isomer (**PyBTA-1**). In general, all values obtained for ΔE_{ST} for PTZ and PXZ donors with all core isomers were low, being the values for **PyBTA-1-PTZ**, **PyBTA-2-PTZ** and **PyBTA-3-PTZ**, 0.12 eV, 0.12 eV and 0.05 eV, respectively. The values for **PyBTA-1-PXZ**, **PyBTA-2-PXZ** and **PyBTA-3-PXZ**, 0.15 eV, 0.18 eV and 0.12 eV, respectively. In contrast, the values obtained for the **DPA** series were 0.27 eV, 0.40 eV and 0.31 eV for **PyBTA-1-DPA**, **PyBTA-2-DPA** and **PyBTA-3-DPA**, respectively, being quite higher than for the other derivatives also in Zeonex.

In addition, the compounds with **PTZ** and **PXZ** as donors showed high values of the DF/PF ratio showing strong influence of delayed fluorescence in their emission in Zeonex. The highest values were obtained for **PyBTA-1-PTZ** (10.9), **PyBTA-2-PTZ** (9.3) and **PyBTA-3-PXZ** (8.0) all in Zeonex matrix. In contrast the **DPA** derivatives doesn't showed delayed fluorescence at all, but the compounds showed RTP properties in Zeonex matrix. The τ_{DF} show faster decay of DF emission in the order of **PyBTA-1-PTZ** > **PyBTA-3-PTZ** > **PyBTA-2-PTZ** going from 87.9 µs > 25.3 µs > 19.6 µs. The order of **PXZ** donor was

PyBTA-3-PXZ > **PyBTA-2-PXZ** > **PyBTA-1-PXZ** going from 93.5 µs > 60.7 µs > 22.5 µs.

Table 3. Photophysical parameters extracted by the time-dependence analysis

PyBTA	HOST	τ_{PF} (ns)	τ_{DF} (µs)	DF/PF	S_1* (eV)	T_1* (eV)	ΔE_{ST}* (eV)	$\lambda_{max\ PF}$ (nm)	k_{RISC} (s^{-1})
1-PTZ	Zeonex	26 ±0.4	87.9 ±3.6	10.9	2.77	2.65	0.12	506	1.24×10^5
	CBP	24 ±0.4	17.2 ±1.8	1.7	2.72	2.56	0.16	526	9.88×10^4
2-PTZ	Zeonex	20 ±0.2	22.5 ±1.4	9.3	2.76	2.64	0.12	527	4.13×10^5
	CBP	23 ±0.7	10.0 ±0.2	2.5	2.67	2.53	0.14	551	2.05×10^5
3-PTZ	Zeonex	25 ±0.7	43.0 ±0.03	3.2	2.78	2.73	0.05	545	7.44×10^4
	CBP	26 ±1.1	4.2 ±0.2	1.2	2.61	2.58	0.03	550	2.86×10^5
1-PXZ	Zeonex	50 ±1.7	22.5 ±1.4	3.0	2.83	2.68	0.15	496	1.33×10^5
	CBP	37 ±0.8	5.6 ±0.8	0.5	2.66	2.51	0.15	543	8.75×10^4
2-PXZ	Zeonex	40 ±1.9	60.7 ±1.6	3.3	2.72	2.55	0.18	522	5.44×10^4
	CBP	22 ±0,8	24.8 ±0.5	0.5	2.71	2.47	0.24	530	2.18×10^4
3-PXZ	Zeonex	21 ±0.1	93.5 ±1.9	8.0	2.86	2.74	0.12	527	8.56×10^4
	CBP	27 ±0.5	6.6 ±1.1	0.4	2.76	2.54	0.22	520	5.91×10^4
1-DPA	Zeonex	24 ±1.3	(98.5±9.2) $\times10^{6\#}$	-	3.08	2.81	0.27	456	-
	CBP	14 ±0.2	-	-	2.98	2.54	0.44	476	-
2-DPA	Zeonex	17 ±1.0	(110.3±0.1) $\times10^{6\#}$	-	3.13	2.73	0.40	459	-
	CBP	17 ±0.5	-	-	2.91	2.75	0.16	487	-
3-DPA	Zeonex	12 ±0.2	(49.2±0.6) $\times10^{6\#}$	-	3.25	2.94	0.31	444	-
	CBP	14 ±0.9	-	-	3.04	2.66	0.38	476	-

*Obtained from onset values. #phosphorescence

The analysis of the compounds in CBP matrix showed different behaviours for all series with **DPA**, **PXZ** and **PTZ**. The S_1 and T_1 with CBP were all lower than the ones obtained for Zeonex due to the higher polarity of this matrix. The **PTZ** series showed the S_1 varying in the order of **PyBTA-1-PTZ** > **PyBTA-2-PTZ** > **PyBTA-3-PTZ**, while the T_1 was almost not change for **PTZ** derivatives. The same was observed for the T_1 of **PXZ** derivatives but when looking at the S_1 the behaviour was opposite to that observed for **PTZ** derivatives:

PyBTA-3-PXZ > **PyBTA-2-PXZ** > **PyBTA-1-PXZ**. The Values of ΔE_{ST} were similar for **PXZ** and **PTZ** derivatives in CBP and in Zeonex.

1. Photoluminescent characteristics of these compounds are compiled in the **Figure 33** and **Figure 34** for **PTZ** derivatives, **Figure 35** and **Figure 36** for **PXZ** derivatives and **Figure** 37 and **Figure 38** for **DPA** derivatives in Zeonex and CBP matrix. These molecules show the emissions bands at low temperatures and high delays attributed to phosphorescence. In addition, the delay times where DF is observed are much smaller than those where phosphorescence is observed. The spectra of PF emission and DF emission and display a low vibrionic and quite broadband emission characteristic of a charge transfer singlet state, ^{1}CT. Phosphorescence of these molecules presents a more vibrionic emission pattern, showing narrowband and, in some cases, more resolved spectrum, characteristic of local excited state emission, ^{3}LE. As discussed before, for **PTZ** derivatives it is possible to observe the presence of two conformers. It is possible to attribute the emission of **PyBTA-1-PTZ** in Zeonex, **Figure 33a** and **Figure 33d**, starting with the PF emission where it is possible already to see the emission of both conformers, eq and ax. These emissions are very fast and appear as a mixed band. Further, two

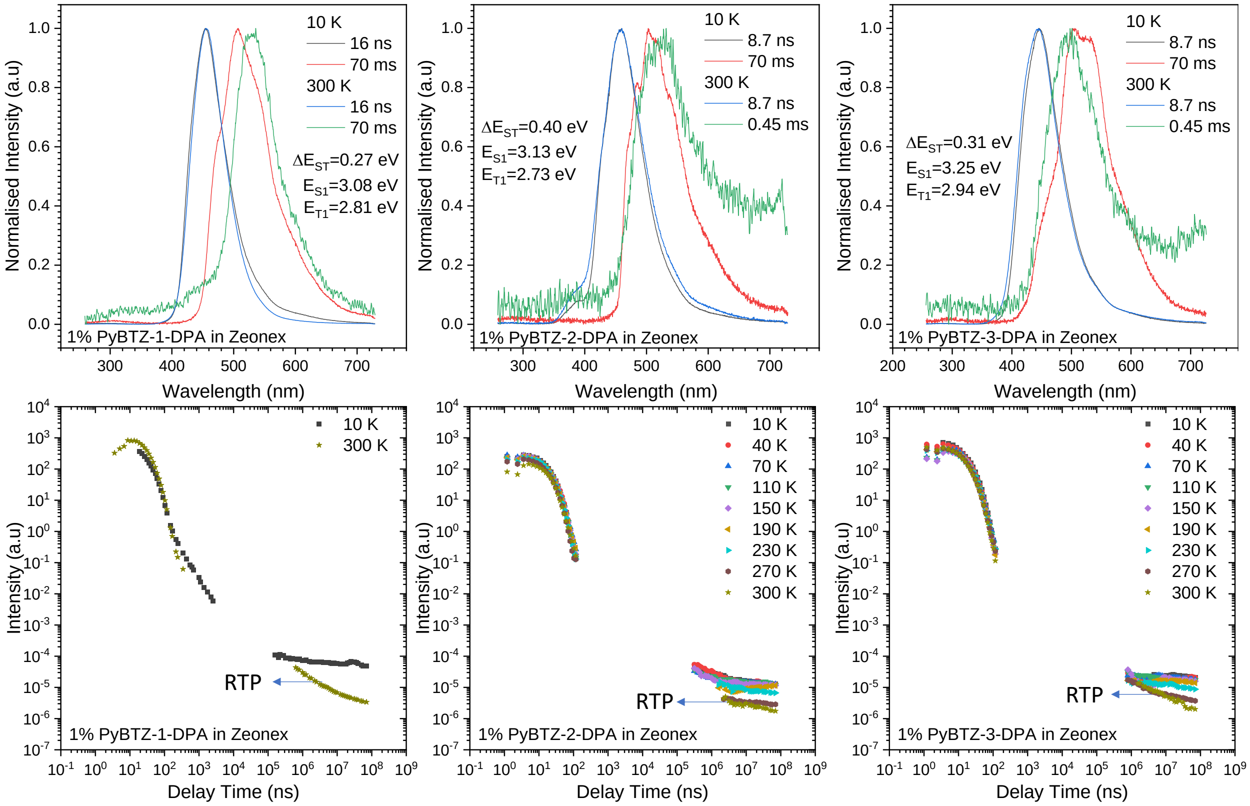

emissions at different delay times and different energies are observed being the eq at lower energy band and ax at higher energy. The first emission at 0.14 ms coming from S_1 as a TADF emission from the first conformer, ax, and after, at 25.1 ms the second emission from the second conformer, eq, and comes also from the S_1 but at lower energy. The **PyBTA-2-PTZ** in Zeonex, **Figure 33b** and **Figure 33e**, showed the same behaviour with emissions at 31.6 µs for the first conformer, ax, and at 70 ms for the second conformer, eq, being both attributed to TADF emission. The compound **PyBTA-3-PTZ** showed in Zeonex, **Figure 33c** and **Figure 33f**, an interesting behaviour with a PF, shorter-lived TADF with redshifted emission, coming from the second conformer, eq, and a second TADF component coming from the ax conformer, at 79.4 µs. The three isomers show a variation of TADF lifetimes in the order of **PyBTA-2-PTZ** < **PyBTA-3-PTZ** < **PyBTA-1-PTZ**. While that the variation of k_{RISC} was higher for **PyBTA-2-PTZ** then the **PyBTA-1-PTZ** and then **PyBTA-3-PTZ**.

The behaviour observed for the **PTZ** derivatives (**PyBTA-1-PTZ**, **PyBTA-2-PTZ** and **PyBTA-3-PTZ**) in CBP, **Figure 34**, shows the mixed emission from the two conformers being the emission mixed at PF and at TADF. The behaviour of the three isomers were similar but the TADF emission present a small shift on the maximum wavelength of emission but always with the presence of the two conformers emissions. The faster lifetimes were obtained for isomer 3 faster than the isomer 2 that was faster than the isomer 1 same order of the higher k_{RISC} to the lowest.

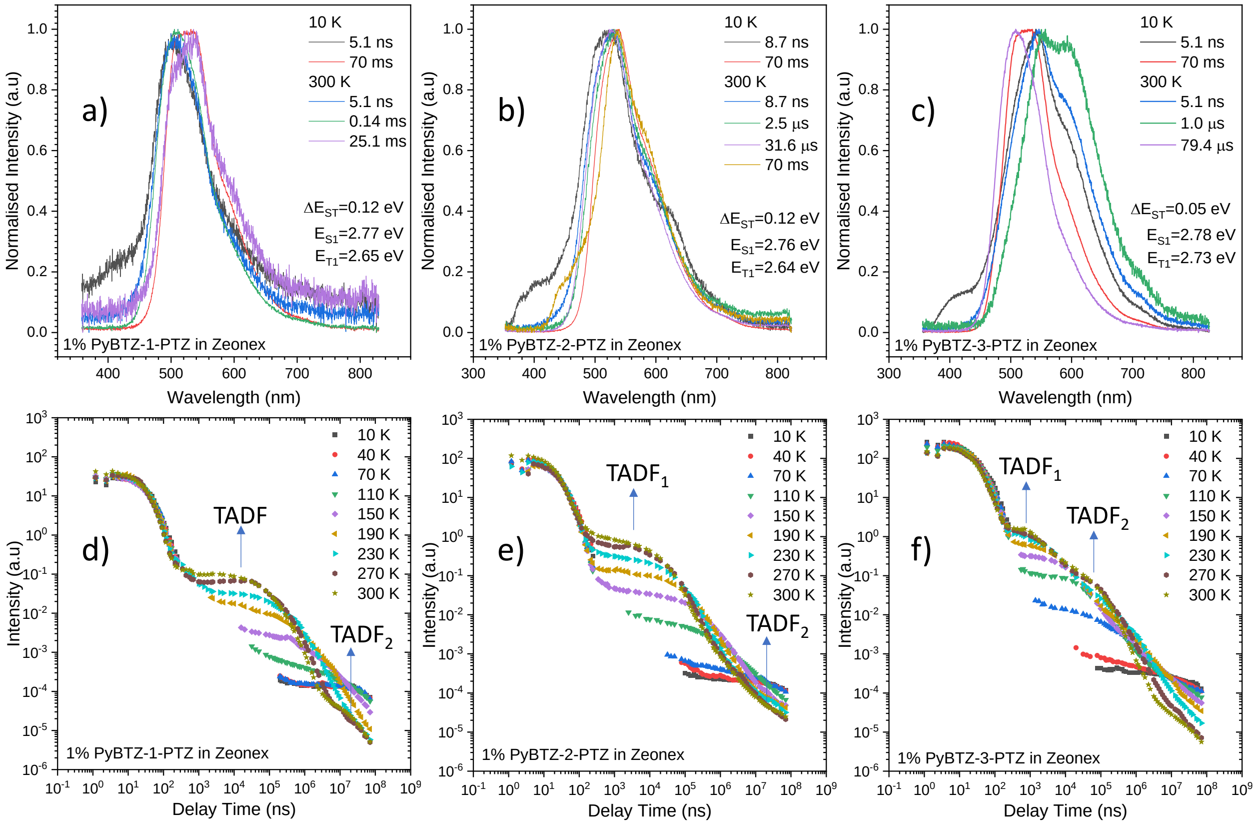

Figure 33. Time-dependence analysis obtained with iCCD camera in different delay times and at different temperatures for compounds **PyBTA-x-PTZ** in Zeonex matrix.

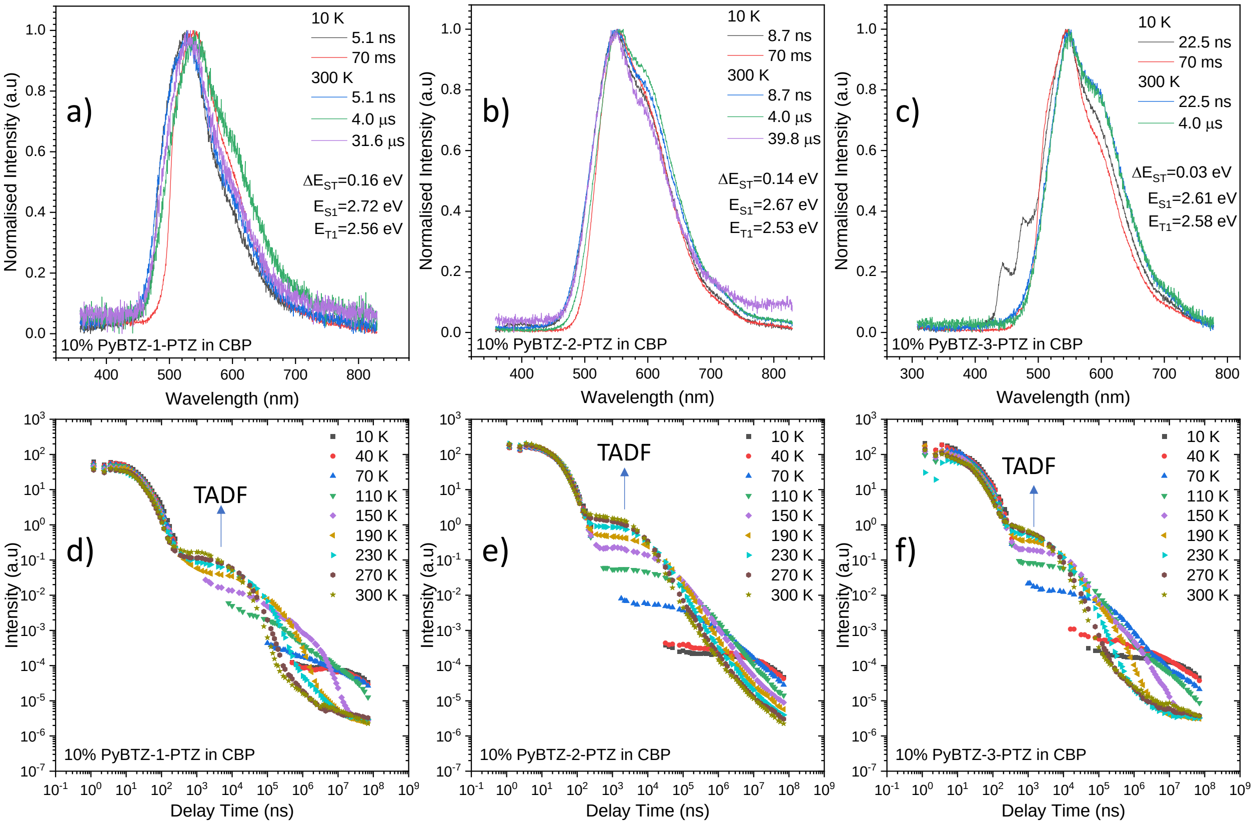

Figure 34. Time-dependence analysis obtained with iCCD camera in different delay times and at different temperatures for compounds **PyBTA-x-PTZ** in CBP matrix.

The compounds with **PXZ** donor present TADF properties in both matrixes as in the case of **PTZ** derivatives, but here the **PXZ** donor does not form conformers so easily which makes the picture less complicated. The compounds **PyBTA-1-PXZ** in Zeonex, **Figure 35a** and **Figure 35d**, presented, after PF, TADF between 0.3 µs and 1.2 ms. The compound **PyBTA-2-PXZ** in Zeonex, **Figure 35b** and **Figure 35e**, showed a TADF between 0.3 µs and 10.2 ms. The compound **PyBTA-3-PXZ** shows in Zeonex, **Figure 35c**, **Figure 35f** and Error! Reference source not found., between 0.3 µs and 5.3 ms. Comparing the τ_{DF} of each isomer with **PXZ** in Zeonex it is possible to observe the lifetimes for **PyBTA-1-PXZ** < **PyBTA-2-PXZ** < **PyBTA-3-PXZ**. In addition, the k_{RISC} was higher in the order **PyBTA-1-PXZ** > **PyBTA-3-PXZ** > **PyBTA-2-PXZ**.

In CBP compound **PyBTA-1-PXZ**, **Figure 36a** and **Figure 36d**, **PyBTA-2-PXZ**, **Figure 36b** and **Figure 36e**, and **PyBTA-3-PXZ**, **Figure 36c** and **Figure 36f**, present two long-lived components attributed to TADF. This behaviour likely results from heterogeneity in the sample due to the presence of more than one conformer of the **PXZ** donor.[74] A blue shift from the TADF$_1$ to TADF$_2$ component can be interpreted similarly to the case of the emitters with the **PTZ** donor. In this case we observe a conformer eq at shorter delay times and an ax conformer at longer delay times. The k_{RISC} of these compounds presented the same order of obtained in Zeonex, **PyBTA-1-PXZ** > **PyBTA-3-PXZ** > **PyBTA-2-PXZ**.

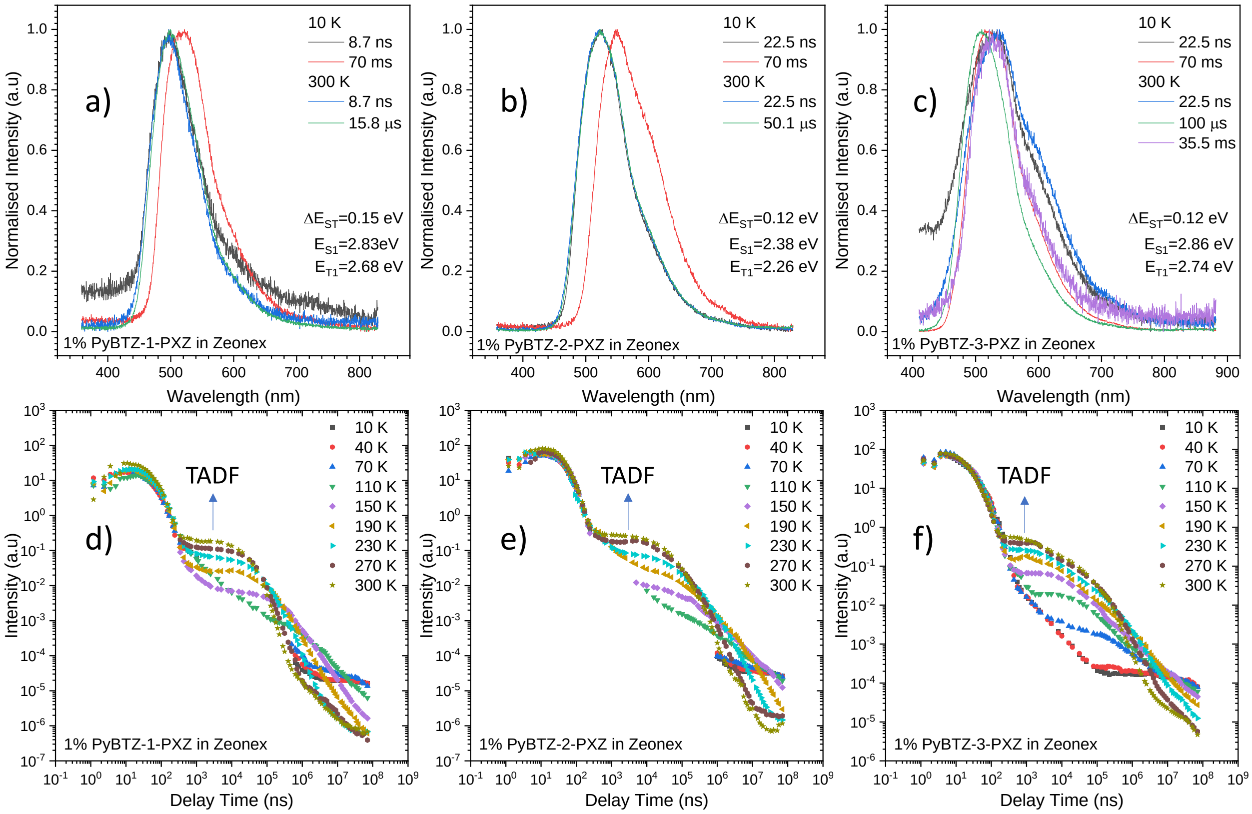

Figure 35. Time-dependent analysis obtained with iCCD camera in different delay times and at different temperatures for compounds **PyBTA-x-PXZ** in Zeonex matrix.

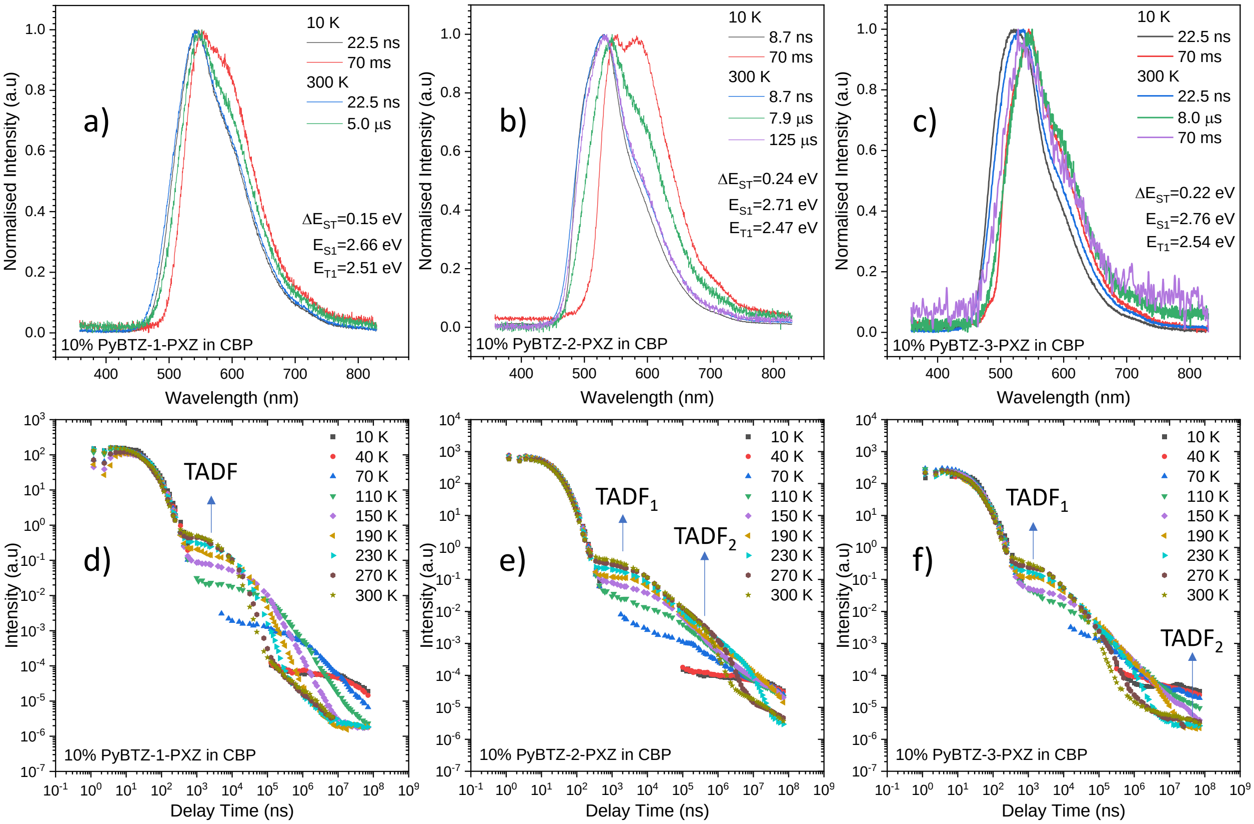

Figure 36. Time-dependent analysis obtained with iCCD camera in different delay times and at different temperatures for compounds **PyBTA-x-PXZ** in CBP matrix.

The compounds with **DPA** as donor, **Figure 37** and **Figure 38**, presented weak RTP emission in Zeonex matrix but no TADF emission was observed in any matrix studied, Zeonex or CBP. In addition, in CBP the RTP was not observed. The RTP for all three isomers with the **DPA** donor are shown as green lines in the figures below.

The k_{RISC} for molecules with **PXZ** and **PTZ** derivatives was calculated using the equation, **Equation 5**. The results were shown in **Table 3**. These results show the values of k_{RISC} above than 1×10^5 s^{-1} for these derivatives. In contrast the CBP matrix showed different results for **PTZ** and **PXZ**. These differences between Zeonex and CBP matrixes are coming from the effect of the polarity of the matrix on the excited states.

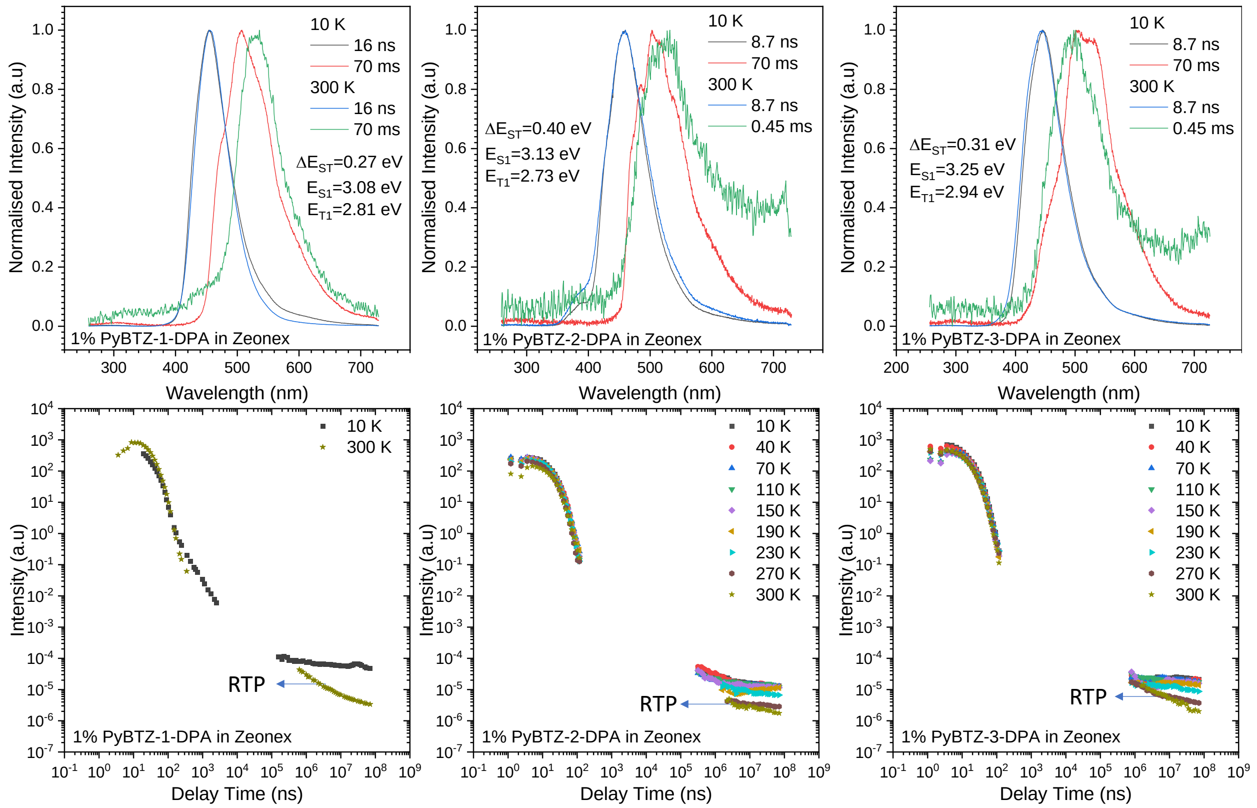

Figure 37. Time-dependent analysis obtained with iCCD camera in different delay times and at different temperatures for compounds **PyBTA-x-DPA** in Zeonex matrix.

The alterations in the position of the methyl group within the molecular core have exerted a noticeable influence on the resultant emission colour. A similar phenomenon is observed when varying the donor moiety while keeping the same acceptor core. This effect enables precise colour tuning by selecting both the donor molecule and the acceptor core. When considering isomeric configurations with identical donor moieties, a notable redshift is observed within the Zeonex matrix. This redshift progresses sequentially from **DPA** to **PXZ** and then to **PTZ** across all isomers. However, in the case of CBP, the order of this redshift varies. For the first isomer, **PyBTA-1**, featuring all three donor molecules, the order of the redshift is as follows: **DPA** to **PTZ** and then to **PXZ**. Conversely, for the second isomer, **PyBTA-2**, and the third isomer, **PyBTA-3**, the observed redshift order corresponds to that previously seen in Zeonex: **DPA** to **PXZ** and then to **PTZ**. These findings provide two distinct avenues for manipulating colour output: one involving fine adjustments through isomeric selection while maintaining a constant donor, and the other involving broader colour adjustments by varying the donor within a given isomeric configuration.

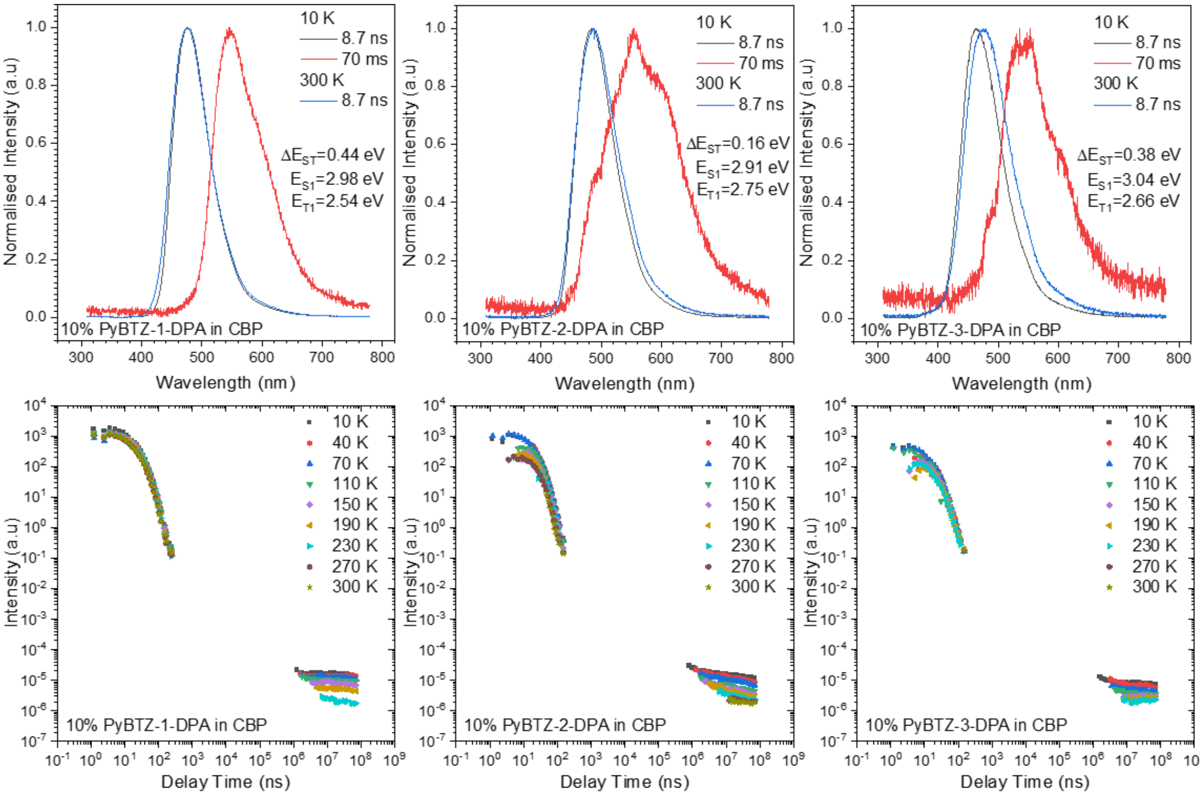

Figure 38. Time-dependent analysis obtained with iCCD camera in different delay times and at different temperatures for compounds **PyBTA-x-DPA** in CBP matrix.

5.1.5. OLED results for PyBTA-X-Donor compounds

To investigate the applicability of the newly developed materials as TADF OLED emitters, we fabricated solution-processed devices using them as the emissive dopants. The devices 1-9 (**PyBTA-1-PTZ**, **PyBTA-2-PTZ**, **PyBTA-3-PTZ**, **PyBTA-1-PXZ**, **PyBTA-2-PXZ**, **PyBTA-3-PXZ, PyBTA-1-DPA**, **PyBTA-2-DPA** and **PyBTA-3-DPA**) are based on the structure ITO / PEDOT:PSS (30 nm) / 10% **PyBTA-X-Donor** + CBP (25 nm) / TPBi (50 nm) / LiF (1nm) / Al (100 nm). The PEDOT:PSS and the emissive layer were deposited by spin-coating, while the rest was deposited by thermal evaporation. The characteristics of the electroluminescent devices are shown in **Figure 39**, **Figure 40** and **Figure 41** and summarized in **Table 4**. All devices present a low turn-on voltage, between 4 V to 5 V. The emission colour of the devices varies from orange to blue following the strength of the donor moiety attached to the **PyBTA-x** cores (**Figure 42**). The less efficient OLEDs are obtained with emitters containing the **DPA** as donor, **PyBTA-x-DPA**. The OLEDs displaying higher EQE are made with TADF emitters **PyBTA-x-PTZ**, **PyBTA-x-PXZ** with **PyBTA-2-PTZ** and **PyBTA-1-PXZ** showing the highest values of EQE 15.9 % and 14.9 %, respectively. This can be attributed to the higher k_{RISC} in these compounds in CBP and lesser susceptibility for triplet quenching. The lowest EQE of OLEDs was obtained using **DPA** derivatives as emitters which correlates with the time-resolved photophysics analysis showing no TADF properties in CBP matrix.

Table 4. Photophysical properties of OLED devices 1-9.

Device	**Compound**	**λ_{emiss} (nm)**	**EQE_{max} (%)**	**Luminance (cd m^{-2})**	**Turn on (v)**	**Current efficiency (cd A^{-1})**	**FWHM (nm)**
1	**PyBTA-1-PTZ**	566	6.4	1660	4.0	9.2	98
2	**PyBTA-2-PTZ**	573	15.9	2063	4.7	16.0	94
3	**PyBTA-3-PTZ**	569	6.0	992	3.7	7.9	91
4	**PyBTA-1-PXZ**	564	14.9	3621	4.3	22.6	105
5	**PyBTA-2-PXZ**	569	6.6	2922	4.4	11.6	92
6	**PyBTA-3-PXZ**	567	9.6	1280	4.1	11.9	96
7	**PyBTA-1-DPA**	487	1.4	304	4.6	3.1	147
8	**PyBTA-2-DPA**	485	2.0	253	3.8	2.6	74
9	**PyBTA-3-DPA**	480	1.7	70	3.6	1.9	117

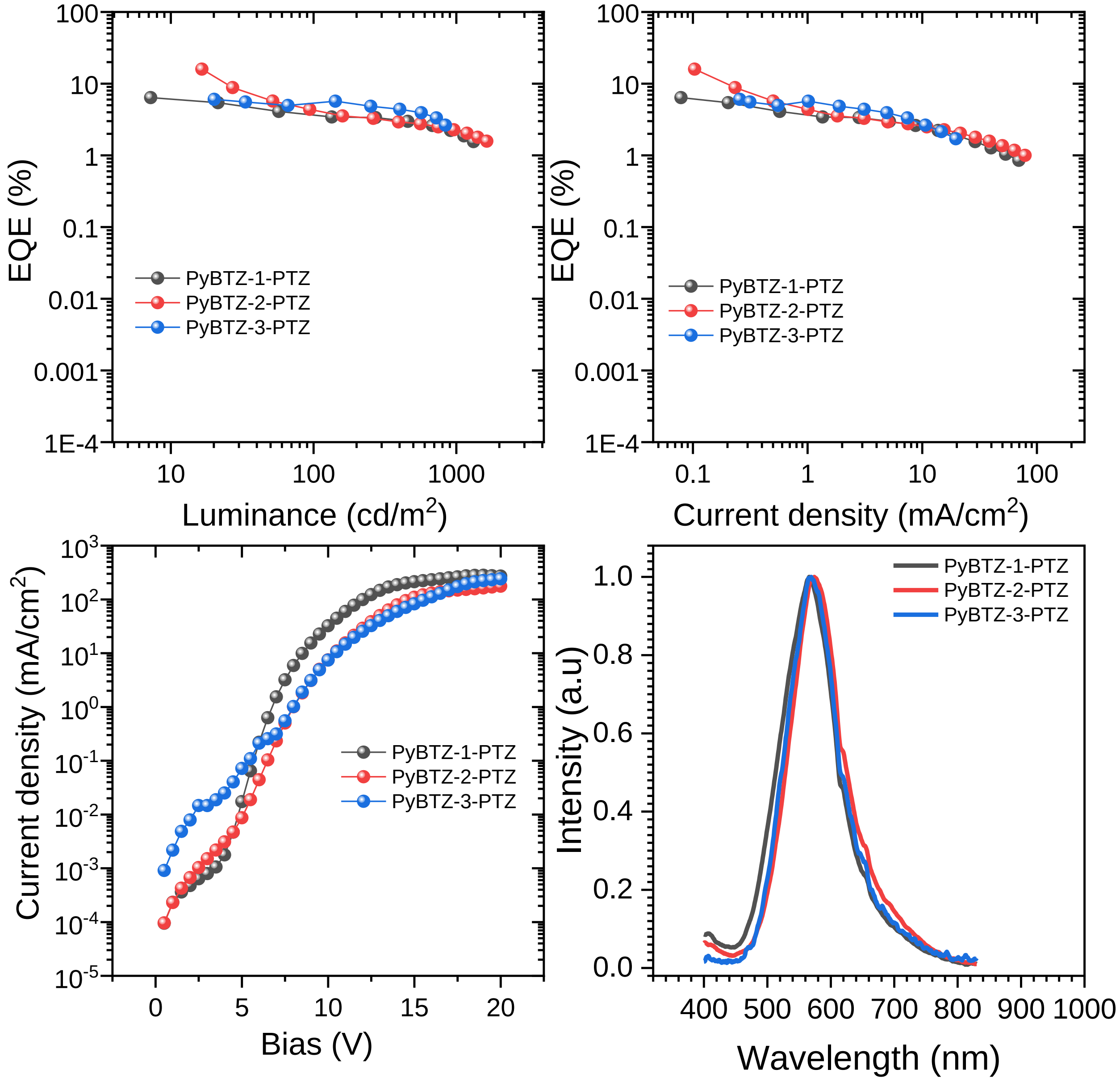

Figure 39. Results of devices with PTZ as donor. a) EQE vs. Luminance. b) EQE vs. Current density. c) Current density *vs.* Bias. d) Normalized electroluminescence of devices.

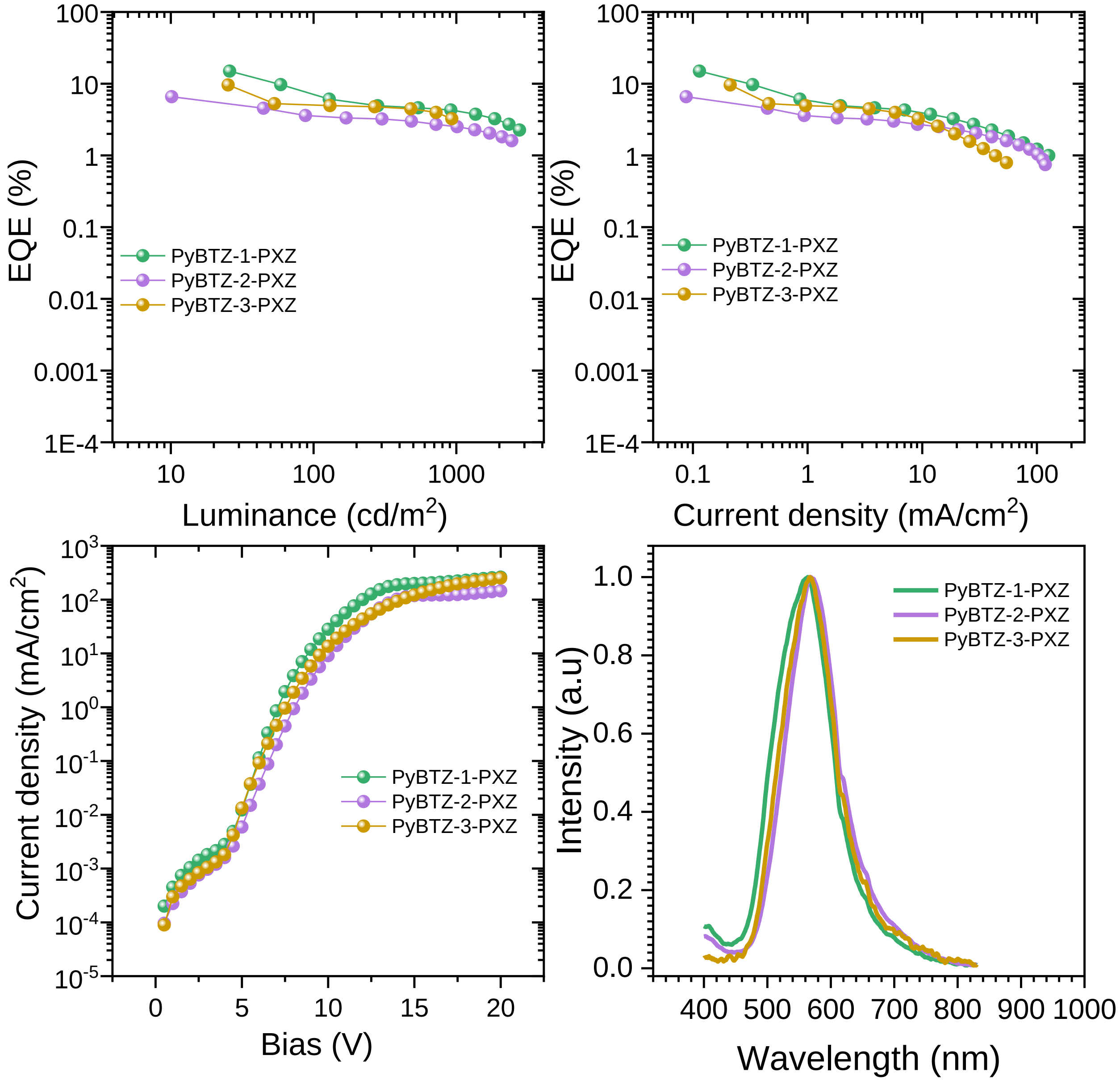

Figure 40. Results of devices with PXZ as donor. a) EQE vs. Luminance. b) EQE vs. Current density. c) Current density vs. Bias. d) Normalized electroluminescence of devices.

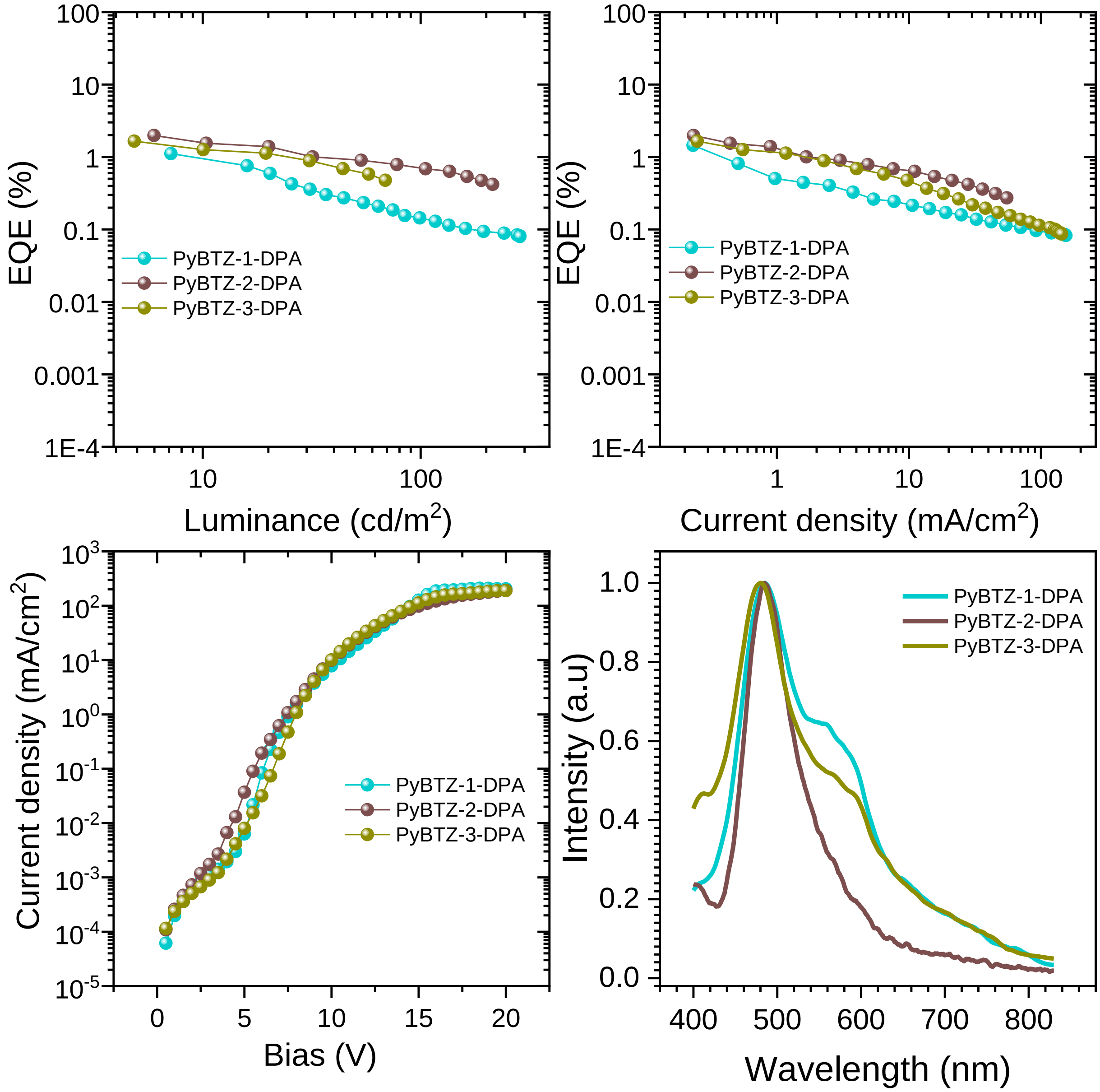

Figure 41. Results of devices with DPA as donor. a) EQE vs. Luminance. b) EQE vs. Current density. c) Current density vs. Bias. d) Normalized electroluminescence of devices.

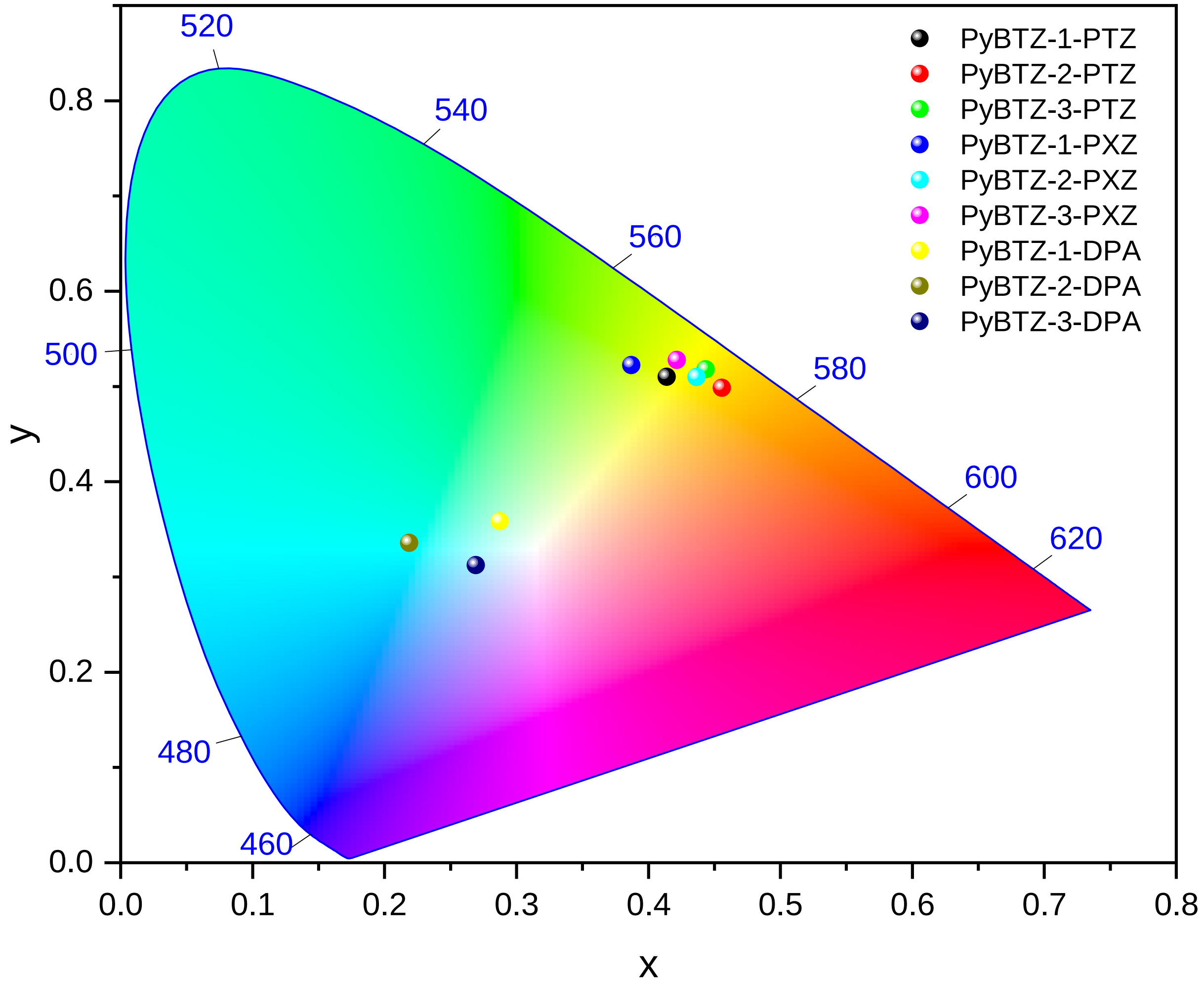

Figure 42. Chromaticity of the electroluminescence of all **PyBTA-x-Donor** derivatives in the devices 1-9.

5.1.6. Conclusions

The analysis for the compounds **PyBTA** showed how the small changes in the core can affect the properties of the materials. The position of the methyl group can be used to tune TADF properties depending on the donor. In addition, the heterogeneity of delayed fluorescence presented for molecules with the **PTZ** and **PXZ** donors due to the existence of axial and equatorial conformers could be observed. Besides that, the photophysics studies showed the promising results for the compounds containing **PTZ** and **PXZ** for the three isomers to be applied in OLED devices. After these analysis the OLEDs were fabricated by solution process and the best results were obtained with **PyBTA-2-PTZ** and **PyBTA-1-PXZ**, achieving 15.9 % and 14.9 % of EQE, respectively. The **PyBTA** unit has shown a promising value as an N-rich core for the development of TADF compounds. In future, another acceptor core can be explored for its isomers which provide small modifications and use this work as a reference. In perspective, it would be possible to explore more donors such as DPAC and DMAC, for example. Another option would be to use the presented molecules in other applications, such as singlet oxygen generation, photodynamic therapy, or explore properties like aggregation-induced emission (AIE).

5.2. Acenaphtopyrido[2,3-b]pyrazine Derivatives (NQPy-donor)

The results presented in this chapter have been published as:

W. P. Silva, **N. O. Decarli**, L. Espíndola, K. Erfurt, A. Blacha-Grzechnik, P. Pander, M. Lapkowski and P. Data

"Multifunctional Properties of D-A Luminophores Based on Acenaphtopyrido[2,3-b]pyrazine Core: Photophysics, Photochemistry, and Efficient Solution-Processed OLEDs."

J Mater Chem C. **2023,** 1, 3777. **doi:10.1039/D3TC02860G**

Molecules with a D-A structure are good candidates to display a clear separation between HOMO and LUMO, thus helping to achieve a low ΔE_{ST} and making TADF properties possible.[75] Besides that, the molecules that present singlet and triplet excited states with CT character and also have the presence of an energetically accessible ^{3}LE state can show a good ISC and present efficient RTP or TADF properties.[51] Multifunctional molecules are able to present different properties showing the possibility for different types of applications. For example, molecules with AIE or AIEE properties can be used in non-doped OLEDs, but also used at higher concentration in doped devices without showing aggregation-caused quenching (ACQ).[76] The use of N-rich heterocyclic cores in design of new emitters to OLED applications is already well established in literature due to the higher electron affinity of nitrogen atom compared with carbon.[77] As shown in sections 2.1.1, 2.1.2 and 2.1.3 many derivatives with N-rich heterocyclic cores were already studied in OLED applications. Besides that the acenaphtopyrido[2,3-b]pyrazine core (**NQPy**) was published before by our group with various silicon derivatives were the authors investigated the TADF properties and applied them to OLED devices, obtaining up to 9.1 % of EQE.[66] However, the effect of different donors can provide various properties to the material as shown below. The versatile properties of materials presented in this chapter were explored by various techniques and applied in OLEDs as well as for singlet oxygen generation (SO). In this study the same core with different donors, **Figure 25**, was investigated and applied successfully in OLED devices. With the variation of donor, it was possible to obtain molecules that showed multifunctional properties like RTP, TADF, AIE/AIEE, and photoactivity for singlet oxygen (SO) generation. Basically, molecules that presented RTP properties and longer triplet lifetime showed better results in SO generation while the ones with TADF properties were better in OLED devices.

5.2.1. Cyclic voltammetry of NQPy-donor derivatives

Electrochemical behaviour of the D-A molecules was studied using cyclic voltammetry (CV) to estimate the HOMO and LUMO energy. The results are compiled in Table 5, while the voltammograms are presented in **Figure 43. Voltammograms of NQPy-Donor molecules recorded with 1 mM of** the analyte using tetrabutylammonium tetrafluoroborate 100 mM in CH2Cl2 as the supporting electrolyte..

Table 5. HOMO and LUMO energy from cyclic voltammetry and theoretical calculations.

	Cyclic Voltammetry		
Compound	**HOMO (eV)**	**LUMO (eV)**	***E*$_g$ (eV)**
NQPy-PTZ	-5.49	-3.45	2.04
NQPy-PXZ	-5.56	-3.56	2.00
NQPy-DMAC	-5.68	-3.44	2.24
NQPy-DPAC	-5.77	-3.44	2.33
NQPy-DDA	-5.90	-3.19	2.69
NQPy-IMD	-5.87	-3.18	2.71
NQPy-CBZ	-6.01	-3.49	2.52
NQPy-DPA	-5.85	-3.41	2.44

a. Recorded with 1 mM of the analyte using tetrabutylammonium tetrafluoroborate 100 mM in CH_2Cl_2 as the supporting electrolyte.

All compounds display reversible first reduction process localized on the acenaphtopyrido[2,3-b]pyrazine acceptor. First oxidation process is mostly reversible for **NQPy-PXZ**, **NQPy-PTZ**, and **NQPy-DMAC**, while it is mostly irreversible for the others (**Figure 43**). The data show increasing HOMO energies according to the donor strength: **NQPy-CBZ** < **NQPy-DDA** < **NQPy-IMD**, **NQPy-DPA < NQPy-DPAC** < **NQPy-DMAC** < **NQPy-PXZ** < **NQPy-PTZ**. The LUMO energy appears to be affected by a partial conjugation with the donor and hence it varies according to its type. The results are in-line with those reported earlier for molecules **2** and **3**.[66]

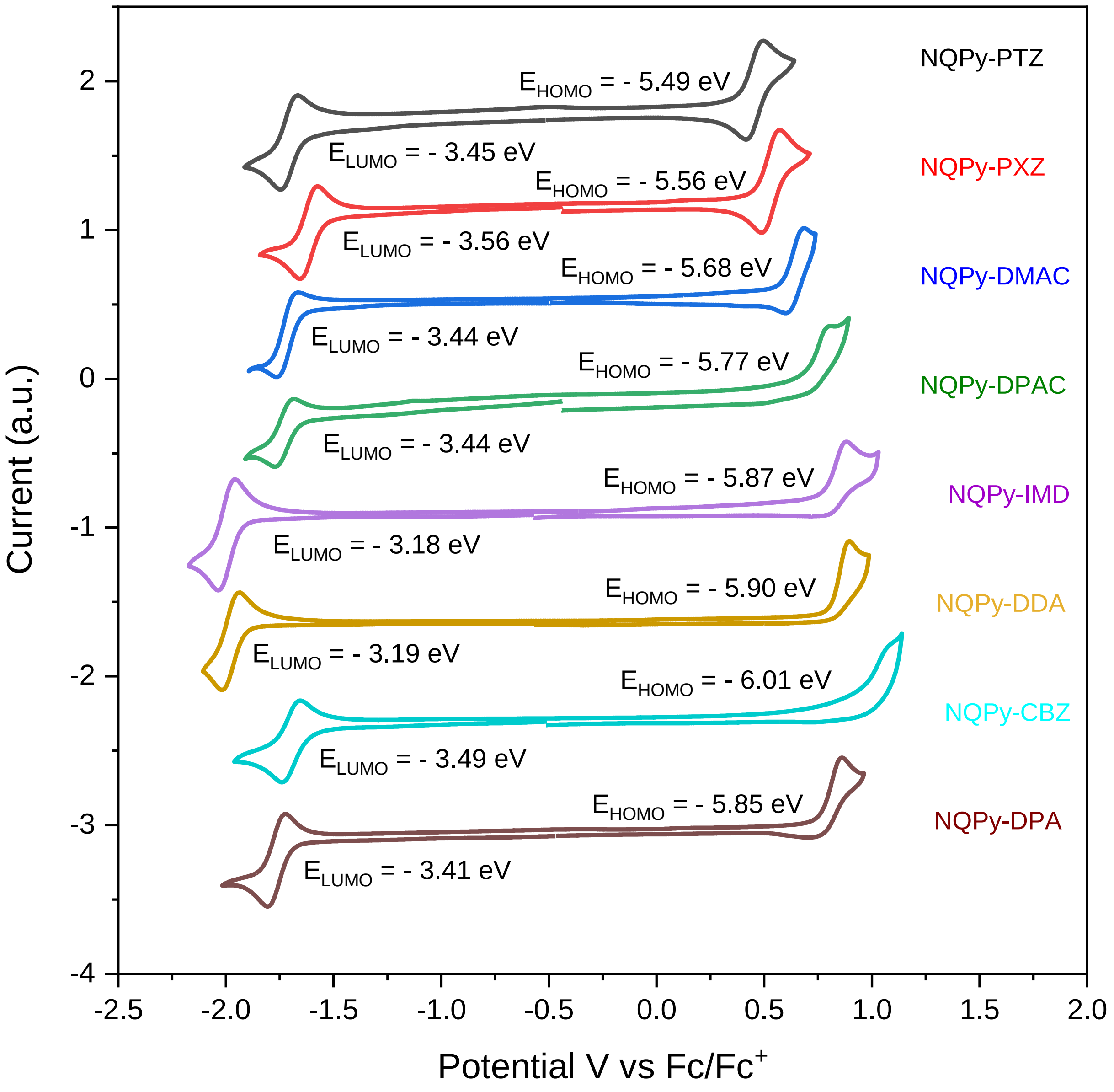

Figure 43. Voltammograms of **NQPy-Donor** molecules recorded with 1 mM of the analyte using tetrabutylammonium tetrafluoroborate 100 mM in CH_2Cl_2 as the supporting electrolyte.

5.2.2. Steady state spectroscopy of NQPy-donor derivatives

The ultraviolet-visible (UV-Vis) absorption in dichloromethane (DCM) and photoluminescence (PL) spectra in DCM and toluene at room temperature are shown in **Figure 44** while the relevant spectroscopic data are summarized in **Table 6**. All the compounds display strong absorption bands at around 290-330 nm which can be attributed to the π→π* LE transitions localized on the acceptor and/or donor moieties.[78–80] Broad bands of lower intensity can be observed from 390 to 510 nm and can be assigned to a CT transition from the donor units to the acceptor.[81] The said CT bands are more intense for **NQPy-DDA**, **NQPy-IMD**, **NQPy-DPA**, and **NQPy-CBZ** where the partial D-A conjugation is more evident, leading to a larger HOMO-LUMO overlap, and less intense for **NQPy-DMAC, NQPy-DPAC**, **NQPy-PXZ**, and **NQPy-PTZ** as the molecules adopt a more twisted conformation, leading to a limited D-A conjugation and smaller HOMO-LUMO overlap.

Table 6. Summary of photophysical characteristics of the studied D-A luminophores.

Compounds	**λ_{abs}/nm [ε/10^{3}M^{-1} cm^{-1}]^a**	**λ_{em} [nm] DCM**	**λ_{em} [nm] Toluene**	**PLQY [%] DCM/TOL**
NQPy-PTZ	322 [30.1], 418 [8.4], 485sh [2.6]	518	476, 656	<1/<1
NQPy-PXZ	322 [63.9], 472 [2.3], 566sh [0.8]	-	638	-/1.7
NQPy-DMAC	322 [80.4], 447 [3.9]	657	580	<1/19.1
NQPy-DPAC	322[14.2], 440 [1.3]	627	557	3.8/26.5
NQPy-DDA	307 [25.1], 348 [16.2], 426 [12.5]	500, 624	473, 545	10.3/31.2
NQPy-IMD	304 [31.2], 345 [21.2], 417 [14.8]	495	472	2.9/11.8
NQPy-CBZ	292[10.4], 317 [19.0], 419 [4.76]	537	485	81.9/43.8
NQPy-DPA	312 [69.7], 351 [24.6], 444 [26.3]	581	529	77.5/99.6

[a] Absorption spectra recorded in DCM solutions.

Were observed photoluminescence for all compounds in toluene and DCM with the exception of **NQPy-PXZ** which is not emissive in the latter. The lack of photoluminescence from **NQPy-PXZ** in the polar DCM is related to a strong stabilization of the ^{1}CT excited state leading to luminescence quenching.[82,83] Majority of the emitters, with the exception of **NQPy-PTZ** and **NQPy-DDA**, display a single CT or CT+LE emission band in solution. The increase of solvent polarity between toluene and DCM induces a redshift in the emission of these luminophores, reflecting the sensitivity towards solvent polarity displayed by luminescent CT singlet states. Noted that the PL spectra of **NQPy-DDA** and **NQPy-IMD** in toluene display a degree of vibrionic resolution, indicating a higher ^{1}LE contribution to the excited state than in the case of the other studied molecules. **NQPy-PTZ** shows dual emission in toluene solution with maxima at λ_{PL} = 476 nm and at λ_{PL} = 656 nm. The longer wavelength band at λ_{PL} = 656 nm then vanishes in DCM, while the band at λ_{PL} = 476 nm displays a redshift. This behaviour is in-line with similar examples reported earlier.[82,84,85] The longer wavelength band is related with the lowest ^{1}CT state which becomes non-emissive in higher polarity solvents, while the shorter wavelength band is attributed to a higher energy ^{1}CT. A similar behaviour can also be observed for **NQPy-DDA**. A potential explanation of this behaviour can be related to the donor assuming two stable conformations: *i.e*. ax and eq, resulting in two distinct CT energies. Such behaviour of the **PTZ** donor has been widely investigated [71,86–89] in the past and one may speculate the **DDA** donor behaves in a similar manner.

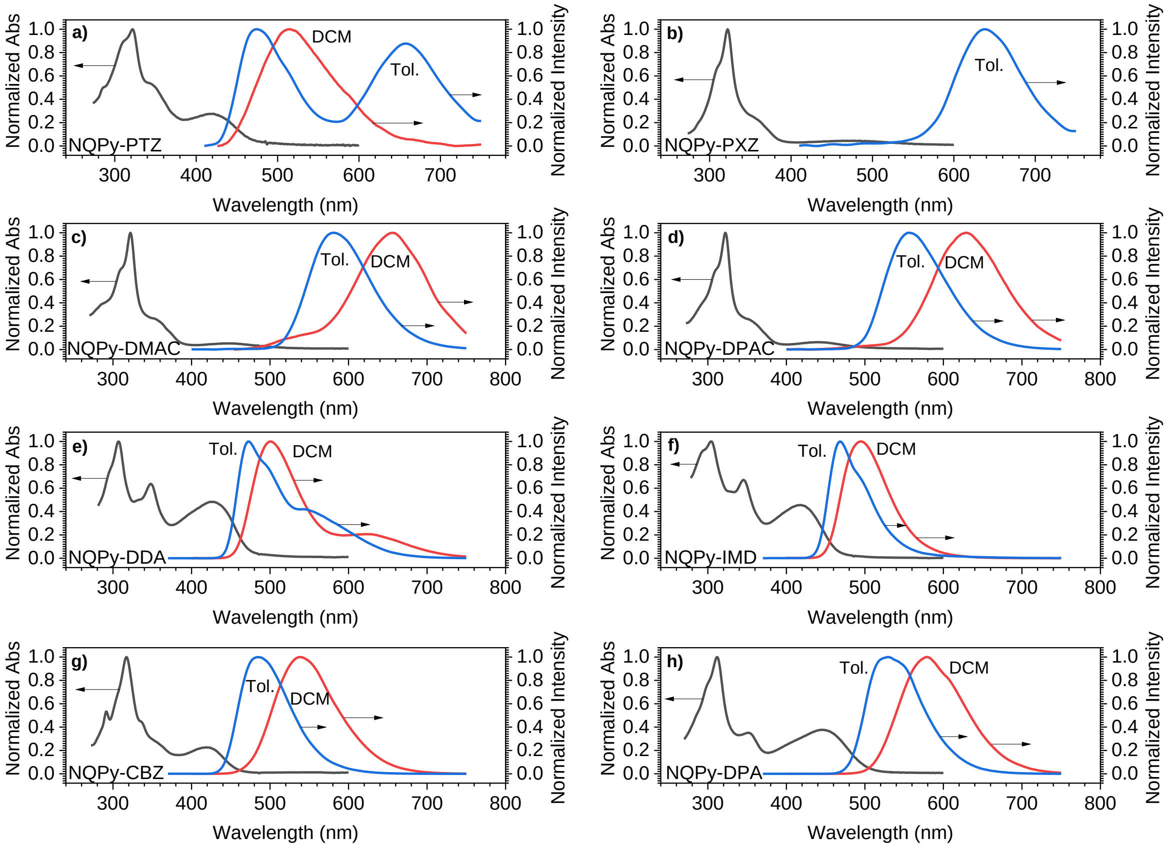

Figure 44. Normalized absorption (DCM only) and photoluminescence spectra in DCM and toluene, c = 10^{-5} M. a) **NQPy-PTZ**; b) **NQPy-PXZ** (not emissive in DCM); c) **NQPy-DMAC**; d) **NQPy-DPAC**; e) **NQPy-DDA**; f) **NQPy-IMD**; g) **NQPy-CBZ**; g) **NQPy-DPA**.

NQPy-PTZ and **NQPy-PXZ** show a negligible PLQY in DCM and toluene solutions. **NQPy-IMD**, **NQPy-DMAC** and **NQPy-DPAC** show a significantly higher PLQY in less polar toluene than in DCM which is related to polarity quenching of ^{1}CT states. The highest PLQY values, > 80 %, were recorded for **NQPy-DPA** and **NQPy-CBZ**.

5.2.3. Aggregation-induced emission (AIE) and aggregation-induced emission enhancement (AIEE)

After the observation that some of these compounds do not show emission in solution but present a bright emission in solid state the AIE and AIEE properties were investigated. To do that a mixture of different proportions of water and THF were used: 0, 20, 40, 60, 80 and 90 % of water (f_w) in THF keeping the same final concentration of compound for all, 100 µM. The experimental photographs of solutions, **Figure 45**, show change in the emission upon increased amounts of water showing a distinct behaviour to the **NQPy** compounds in 0, 80 and 90 % of water.

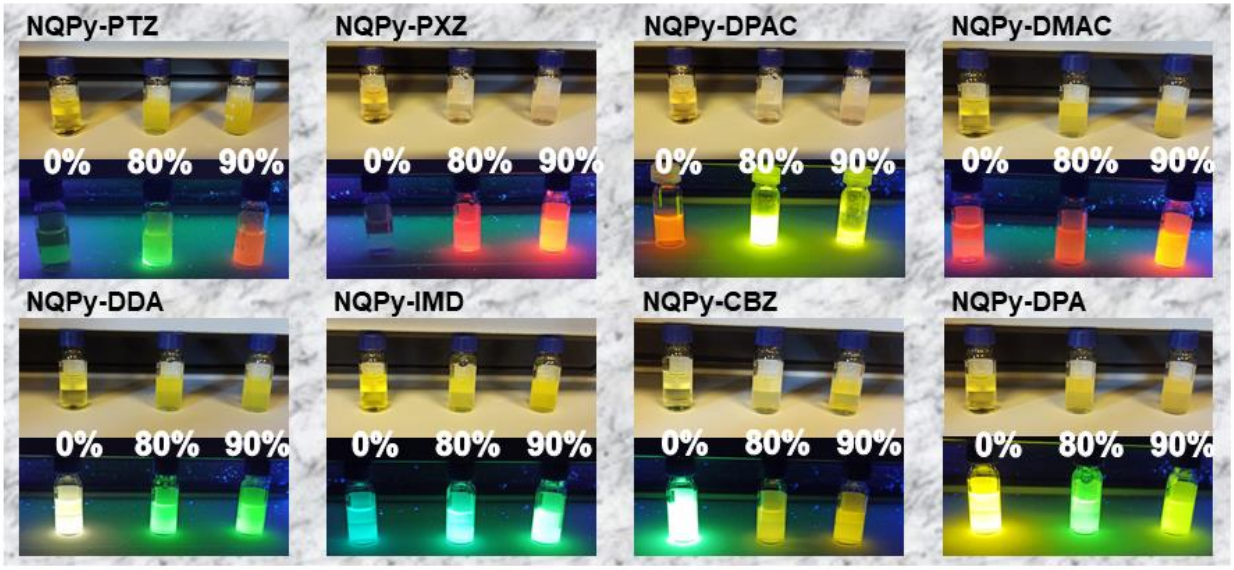

Figure 45. Solutions and dispersions of the D-A compounds in THF (f_w = 0 %) and THF/water mixtures, f_w = 80-90 %. Top images show photographs under ambient light, while the bottom are recorded with UV light illumination.

Photoluminescence spectra of all compounds and relative PL intensity in function of f_w are presented in **Figure 46** and **Figure 47**. The results show compounds **NQPy-PTZ** and **NQPy-PXZ** with a very low emission in pure THF (f_w = 0 %), and increasing emission up to f_w = 90 %, indicating AIEE property. In the case of **NQPy-PXZ** the emission intensity is increasing 50-100 fold in the same experiment, but the PLQY in organic solvents without aggregation is lower than 2 %, which allows to attribute this behaviour to AIE instead of AIEE. **NQPy-DMAC**, **NQPy-DPAC** and **NQPy-DPA** display a relatively strong emission in dry THF and show a significant decrease upon initial addition of water, process that is called polarity reduced emission.[90] This is due to the CT PL quenching induced by increased solvent polarity caused by the addition of water. With further increasing in the water percentage the emission starts to increase in intensity by up to 100-900 fold depending on the compound. This behaviour is not attributed to AIE due to the molecules presenting emission in pure THF and also in non-polar solvents. The AIE in this case is caused by displacing polar solvent molecules from the aggregates, which become more luminescent due to the solvent no longer restricting the luminescent properties of the intramolecular CT state. **NQPy-DDA**, **NQPy-IMD**, and **NQPy-CBZ** display a similar behaviour to **NQPy-DMAC**, **NQPy-DPAC**, and **NQPy-DPA**, however the overall increase in PL intensity upon aggregation ($f_w > 60$ %) is less spectacular. Importantly, for **NQPy-CBZ** we observe PL intensity at high water content to be significantly lower than in dry THF, an effect in line with aggregation-caused quenching (ACQ). Intriguing behaviour occurs when looking at various f_{w}, for example, the blue shifted photoluminescence observed for compounds **NQPy-DMAC** and **NQPy-DPAC** at around 80 % and 90 % f_{w} compared with pure THF solution. This effect can be attributed to the interactions between fluorophores being less strong than the fluorophores with solvent when they are not aggregated and also due to the aggregates having a more rigid environment than the fluorophores diluted in solution what could cause the blue shift in emission.[91–93]

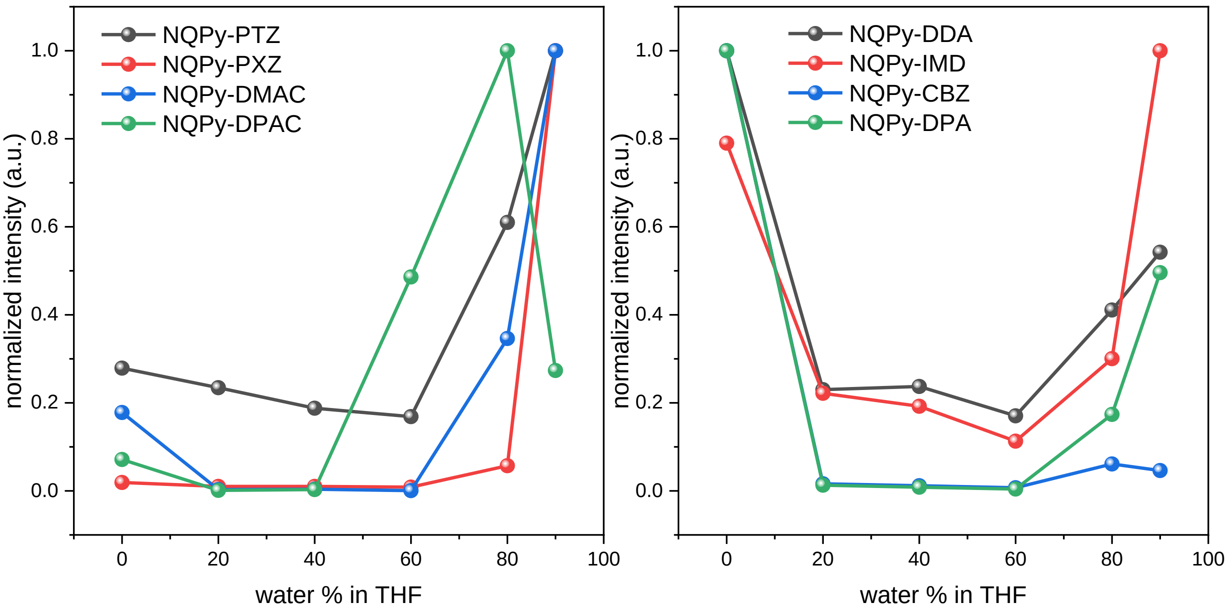

Figure 46. PL intensity in different proportions of water/THF for the **NQPy-Donor** compounds.

The initial THF solutions (f_w = 0 %) and the final suspensions (f_w = 90 %) were examined using the time-correlated single photon counting (TCSPC) technique to identify long-lived luminescence components originating from the aggregates (**Figure 48**). The analysis reveals the emergence of a distinct long decay component in suspension (f_w = 90 %) for **NQPy-DMAC**, **NQPy-DPAC**, **NQPy-PXZ**, **NQPy-PTZ**, and **NQPy-CBZ** that is absent in pure THF. This component can be ascribed to TADF originating from the precipitated particles, at least for **NQPy-DMAC**, **NQPy-DPAC**, **NQPy-PXZ**, and **NQPy-PTZ**. The experiment was conducted under air-equilibrated conditions, and the presence of long-lived photoluminescence indicates restricted access of oxygen molecules to the emitter.[91,94] The aggregates formed in this experiment consist of small solid particles, acting as a barrier that limits oxygen diffusion from the external environment. This protective effect shields the T_1 state of the luminophore from quenching by oxygen.[95]

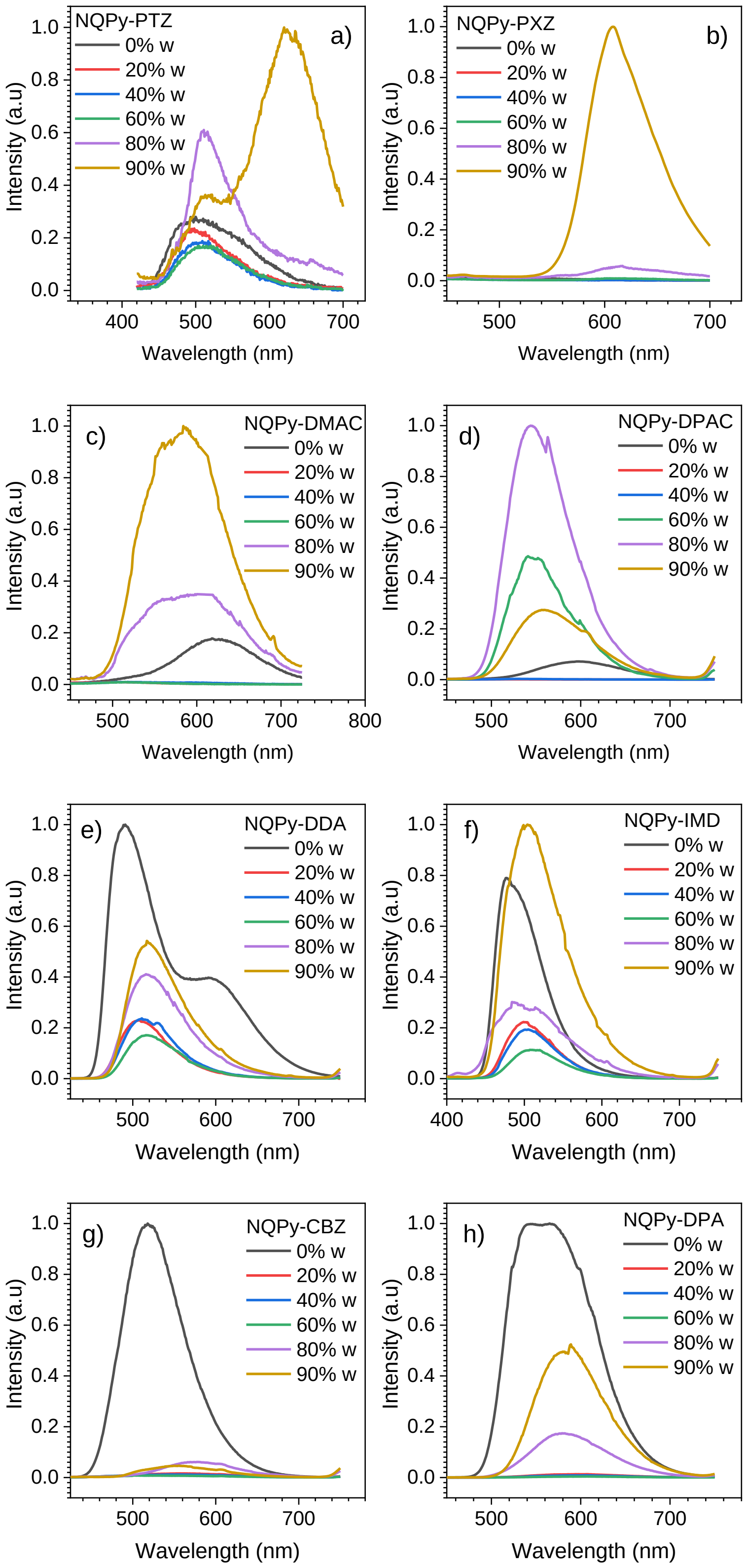

Figure 47. Emission spectra recorded in THF/water mixtures for water fractions f_w = 0-90 %.

Our experiments underscore the need for caution when interpreting results from the "classic AIE experiment," particularly when CT emissive states are involved. Aggregates formed from a nearly non-emissive solution may exhibit photoluminescence due to the expulsion of a polar solvent acting as a quencher, rather than arising from the restriction of intramolecular rotation (RIR). Notably, molecules like **NQPy-DMAC** and **NQPy-DPAC** often display high PLQY in solvents less polar than THF. This prompts a critical question about when to attribute certain luminescent behaviours to the AIE effect. A plethora of D-A luminophores, including those with TADF and RTP, exhibit a common *polarity reduced emission*, but remain highly emissive in non-polar environments. While this behaviour aligns with the conventional AIE concept induced by RIR, interpreting it broadly in the context of D-A luminophores may lead to an overly expansive understanding of the phenomenon.

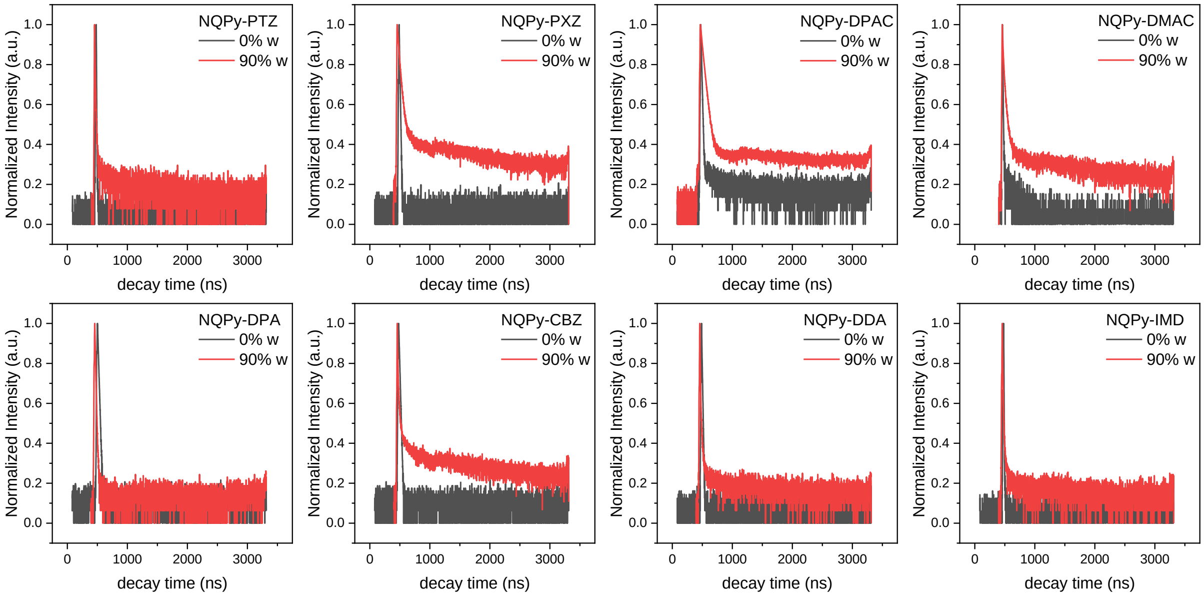

Figure 48. TCSPC traces for f_w = 0 % and 90 % in air-equilibrated solutions.

5.2.4. Time-dependent photoluminescence of NQPy-donor derivatives

To gain insights into the TADF and/or RTP behaviour of the D-A luminophores, it is essential to conduct more detailed photophysical studies utilizing transient photoluminescence spectroscopy. The findings for Zeonex and CBP hosts {4,4’-bis(N-carbazolyl)-1,1’-biphenyl} are illustrated in **Figure 49**, **Figure 50**, **Figure 51**, **Figure 52** and **Figure 53**, and the corresponding photophysical parameters are succinctly presented in **Table 7** and **Table 8**. The examination of these molecules at 1% load in Zeonex enables an exploration of their molecular photophysical properties, while 10% load in CBP mimic their behaviour in OLEDs.

Table 7. Summary classification of the photoluminescent properties of the D-A emitters by the nature of the long-lived decay component, at 300 K.

COMPOUND	ZEONEX	CBP
NQPY-PTZ	**TADF**	**TADF**
NQPY-PXZ	**TADF**	**TADF**
NQPY-DMAC	**TADF**	**TADF**
NQPY-DPAC	**TADF**	**TADF**
NQPY-DDA	**RTP**	**DF/RTP**
NQPY-IMD	**RTP**	**DF/RTP**
NQPY-CBZ	**RTP**	**DF/RTP**
NQPY-DPA	**TADF/RTP**	**DF/RTP**

All compounds display two modes of emission occurring at different delay times: (1) prompt fluorescence (PF) at shorter delay times up to ~200 ns; (2) delayed fluorescence (DF) and/or RTP at delay times > 1 μs. Time-resolved phosphorescence spectra recorded at 10 K and fluorescence spectra were used to determine the ΔE_{ST}. The determination of ΔE_{ST} involved recording time-resolved phosphorescence spectra at 10 K and fluorescence spectra. The emitters can be categorized into two groups: (1) those exhibiting a small ΔE_{ST} with a significant dependency of the intensity and lifetime of the delayed component on temperature; (2) those with a large ΔE_{ST} and minimal temperature dependence in the long-lived component. In group (1), which comprises TADF emitters, there is a distinct similarity between prompt fluorescence and delayed emission at RT. Conversely, in group (2) consisting of RTP emitters, the long-lived luminescence bears resemblance to phosphorescence. At room temperature compounds **NQPy-PTZ**, **NQPy-PXZ**, **NQPy-DMAC** and **NQPy-DPAC**, display typical characteristics of TADF emitters in Zeonex and CBP hosts. In Zeonex, molecules **NQPy-IMD**, **NQPy-DDA**, and **NQPy-CBZ** exhibit the characteristics of RTP emitters. However, in CBP, their behaviour shifts to a mixed delayed fluorescence (DF)/RTP pattern. In Zeonex, **NQPy-DPA** exhibits a blend of RTP and TADF, while in CBP, it demonstrates a combination of DF and RTP. It's noteworthy that the delayed fluorescence component observed in **NQPy-IMD**, **NQPy-DDA**, **NQPy-DPA**, and **NQPy-CBZ** recorded in CBP is not attributed to TADF but instead results from TTA.[96] This issue will be discussed later in the text. Results pertaining to all presented luminophores are shown in Table 8, **Figure 49**, **Figure 50**, **Figure 51**, **Figure 52** and **Figure 53**.

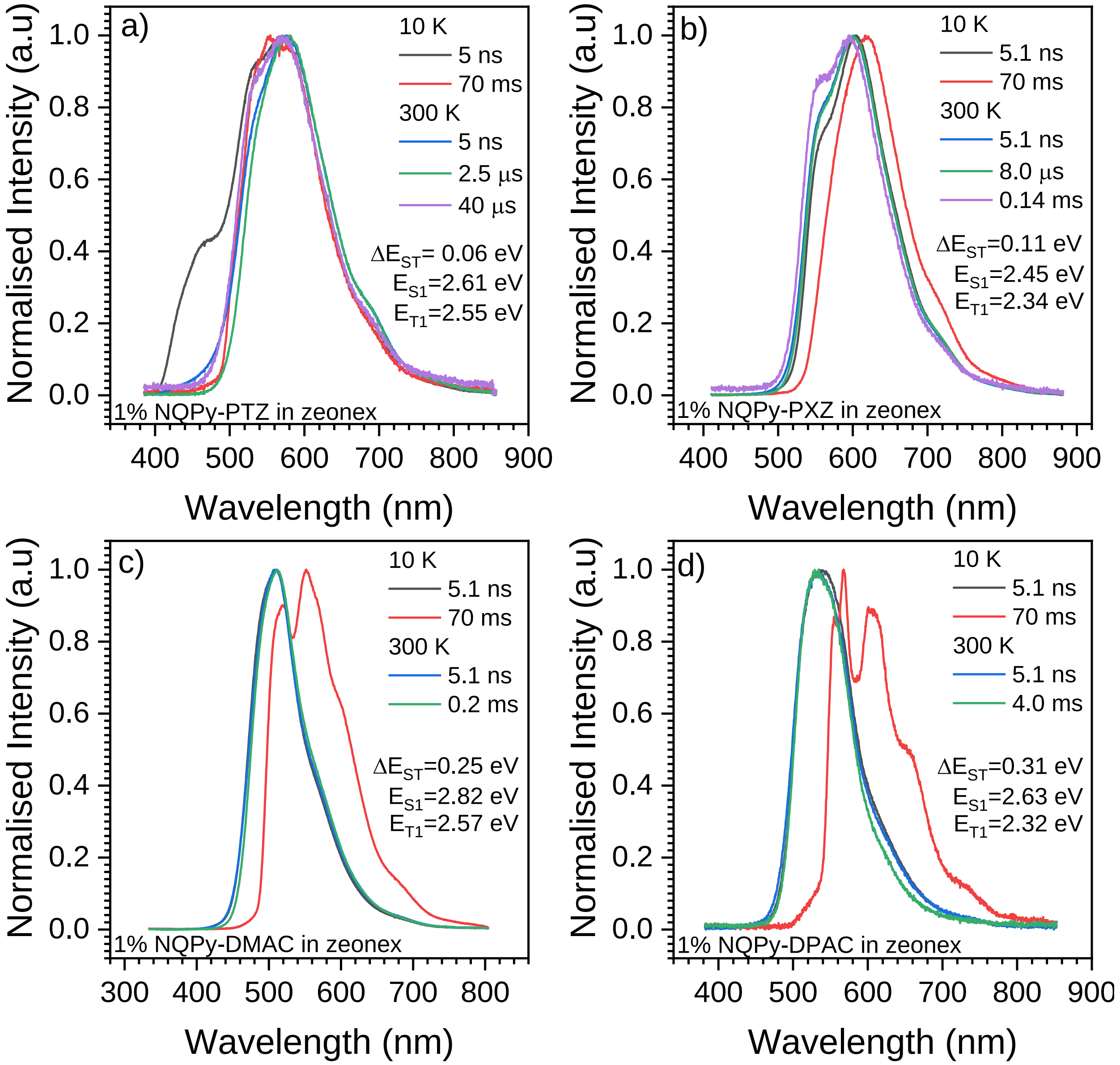

Figure 49. Time-resolved photoluminescence spectra for **NQPy-PTZ**, **NQPy-PXZ**, **NQPy-DPAC**, and **NQPy-DMAC** 1 wt% in Zeonex matrix.

The time-resolved spectra (black and red line in **Figure 49**, **Figure 51**, **Figure 52** and **Figure 53**) at low temperature in Zeonex identify the nature of the T_1 state. With the exception of **NQPy-PTZ** and **NQPy-PXZ**, the phosphorescence spectra of all other molecules exhibit a distinct vibrionic structure, pointing to their pronounced ^{3}LE character. The similarity in vibrionic structure across the spectra of different D-A molecules strongly implies the localization of the ^{3}LE state on the acceptor unit. However, clear ^{3}LE phosphorescence was not observed for **NQPy-PTZ** and **NQPy-PXZ**. It's likely that for these two molecules, the T1 state manifests a ^{3}CT nature, while the ^{3}LE state localized on the acceptor resides energetically above it. Consequently, for **NQPy-PTZ** and **NQPy-PXZ** the $\Delta E_{ST} \approx 0$ eV.[82] Results obtained for all eight emitters in CBP are in agreement with those recorded in Zeonex.

NQPy-PTZ, **NQPy-PXZ**, **NQPy-DMAC**, and **NQPy-DPAC** exhibit a noticeable variation in the TADF component with temperature, a characteristic typical for this type of emitters.[97] To determine the DF/PF ratio, we integrate the prompt fluorescence and TADF components at 300 K. It is observed that in Zeonex, the DF/PF ratio is higher for **NQPy-DMAC** and **NQPy-DPAC** compared to **NQPy-PTZ** and **NQPy-PXZ**. This difference may be attributed to the more favourable ordering of the triplet excited states in the former two, leading to faster ISC and higher triplet formation yields. Generally, the DF/PF ratio in Zeonex exceeds that in CBP, a consequence of the higher emitter concentration, which facilitates triplet-quenching processes.

The behaviour of **NQPy-IMD**, **NQPy-DDA**, **NQPy-DPA**, and **NQPy-CBZ** deviates from that of the other four emitters. In Zeonex, the long-lived luminescent component typically exhibits minimal temperature dependence or an increase in intensity upon cooling. With ΔE_{ST} values exceeding 0.35 eV, these molecules tend to display RTP or RTP+DF behaviour rather than pure TADF. Notably, **NQPy-DPA** demonstrates a mixed TADF+RTP emission in Zeonex (**Figure 54**). In this case, the DF component originates from TADF, as the ratio between the DF and RTP components in the spectrum remains constant with time delay. This constancy indicates that the two bands exhibit identical decay lifetimes, suggesting an equilibrium between the S_1 and T_1 states.[98,99] The situation differs for the long-lived component exhibited by **NQPy-IMD**, **NQPy-DDA**, **NQPy-DPA**, and **NQPy-CBZ** in CBP. In this context, the ΔE_{ST} is comparable to that in Zeonex, precluding TADF. Therefore, the observed delayed fluorescence must be attributed to TTA. The higher emitter concentration in CBP compared to Zeonex promotes triplet-triplet collisions, facilitating TTA. Triplet-triplet annihilation is typically observed at low temperatures, contrasting with the highly thermally assisted TADF,[100] in line with the behaviour of **NQPy-IMD**, **NQPy-DDA**, **NQPy-DPA**, and **NQPy-CBZ** in CBP.

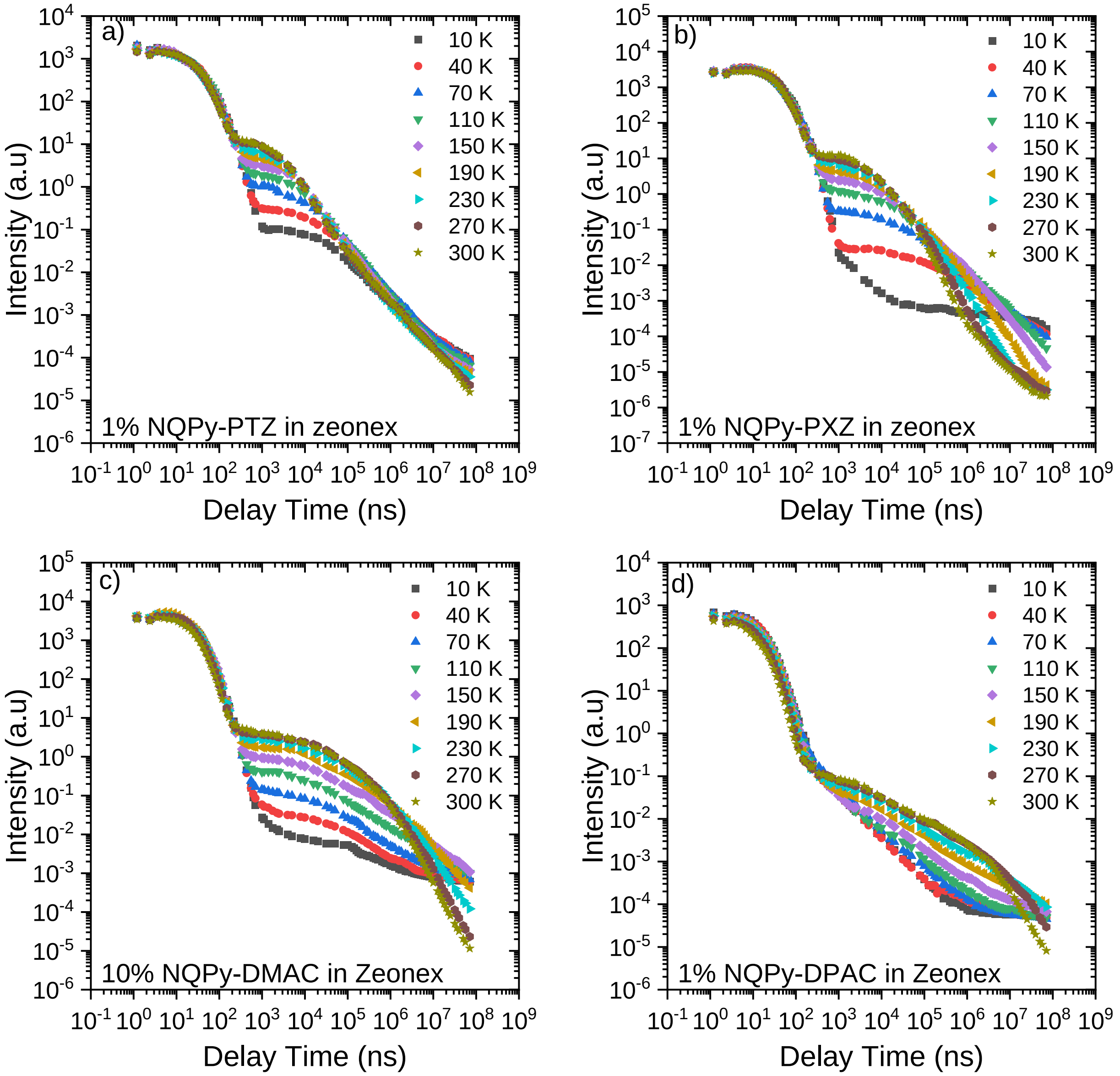

Figure 50. Photoluminescence decay traces for **NQPy-PTZ**, **NQPy-PXZ**, **NQPy-DPAC**, and **NQPy-DMAC** 1 wt% in Zeonex matrix.

Table 8. Photophysical parameters obtained from time-resolved analysis.

COMPOUND	Host	τ_{PF} (ns)[a]	τ_{DF} (μs)[b]	DF/PF[c]	k_{RISC} (s^{-1})[d]	S_1 (eV)[e]	T_1 (eV)[e]	ΔE_{ST} (eV)[f]
NQPY-PTZ	Zeonex	30±0	3±0.5	1.28	4.27×10^{5}	2.61	2.55	0.06
	CBP	17±0	3±0.4*	0.76	2.53×10^{5}	2.51	2.41	0.10
NQPY-PXZ	Zeonex	33±1	14±1*	0.81	5.79×10^{4}	2.45	2.34	0.11
	CBP	14±1	8±0.6*	0.43	5.38×10^{4}	2.39	2.26	0.13
NQPY-DMAC	Zeonex	22±1	116±3*	3.63	3.13×10^{4}	2.82	2.57	0.25
	CBP	19±1	42±0.8*	0.62	1.48×10^{4}	2.67	2.49	0.18
NQPY-DPAC	Zeonex	10±0	200±4*	3.53	1.77×10^{4}	2.63	2.32	0.31
	CBP	18±0	78±9*	1.95	2.50×10^{4}	2.43	2.17	0.26
NQPY-DPA	Zeonex	8±0	$(74\pm5)\times10^{3}$	1.39	1.88×10^{1}	2.79	2.30	0.49
	CBP	9±0	$(112\pm3)\times10^{3}$ *	0.15	1.34×10^{0}	2.56	2.17	0.39
NQPY-CBZ	Zeonex	3±0	$(109\pm5)\times10^{3}$ #*	-	-	3.08	2.54	0.55
	CBP	13±0	$(58\pm6)\times10^{3}$ *	0.46	7.93×10^{0}	2.75	2.23	0.52
NQPY-DDA	Zeonex	10±0	$(116\pm1)\times10^{3}$ #	-	-	2.78	2.28	0.50
	CBP	19±1	$(59\pm0.1)\times10^{3}$ #	-	-	2.81	2.23	0.58
NQPY-IMD	Zeonex	7±1	$(90\pm6)\times10^{3}$ #	-	-	2.95	2.33	0.62
	CBP	5±0	$(4.4\pm0.2)\times10^{3}$ #	-	-	2.87	2.27	0.60

a. Prompt fluorescence lifetime in vacuum CBP/Zeonex® film;
b. Delayed fluorescence lifetime in vacuum CBP/Zeonex® film;
c. Delayed fluorescence (DF) to prompt fluorescence (PF) ratio in each matrix, both obtained from integral areas of the relevant decay traces;
d. k_{RISC} were calculated using the relation between DF/PF and τ_{DF}: $k_{RISC} = \frac{1}{\tau_{DF}}\left(\frac{DF}{PF}\right)$
e. Singlet and triplet energy in each matrix. Error ± 0.03 eV;
f. Singlet-triplet energy splitting in each matrix. Error ± 0.05 eV.

\# Room temperature phosphorescence. *Biexponential fit.

The lifetime of DF or DF+RTP in the solid state typically aligns with the ΔE_{ST} values presented in Table 8, with the shortest observed for **NQPy-PTZ** and **NQPy-PXZ** at 3-15 μs and the longest for **NQPy-DPA**, **NQPy-CBZ**, **NQPy-DDA**, and **NQPy-IMD** at approximately 10-100 ms. In general, the D-A emitters exhibit a quicker decay of the long-lived component in the CBP host compared to Zeonex, except for **NQPy-DPA**, where the two decay lifetimes are comparable. The shorter TADF/RTP lifetimes in the 10 % films in CBP are attributed to the increased emitter load, resulting in a higher occurrence of triplet-quenching phenomena, such as TTA. The polarizability difference between Zeonex and CBP seems to have a minor impact on the emission and is therefore unlikely to be the primary cause of quenching or differences in luminescent properties.

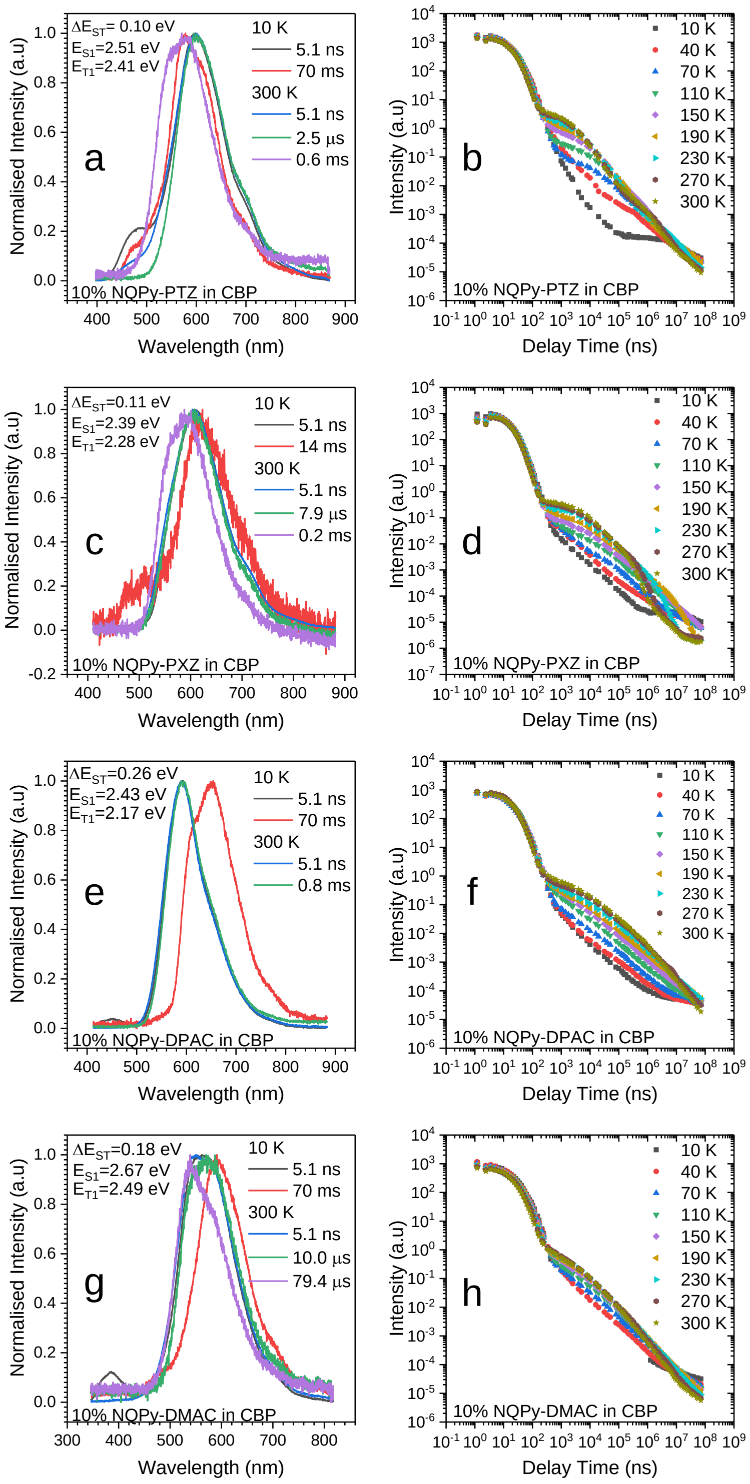

Figure 51. Time-Resolved spectra and the intensity vs. delay time measurements of **NQPy-PTZ**, **NQPy-PXZ**, **NQPy-DPAC** and **NQPy-DMAC** compounds 10 wt% in CBP matrix.

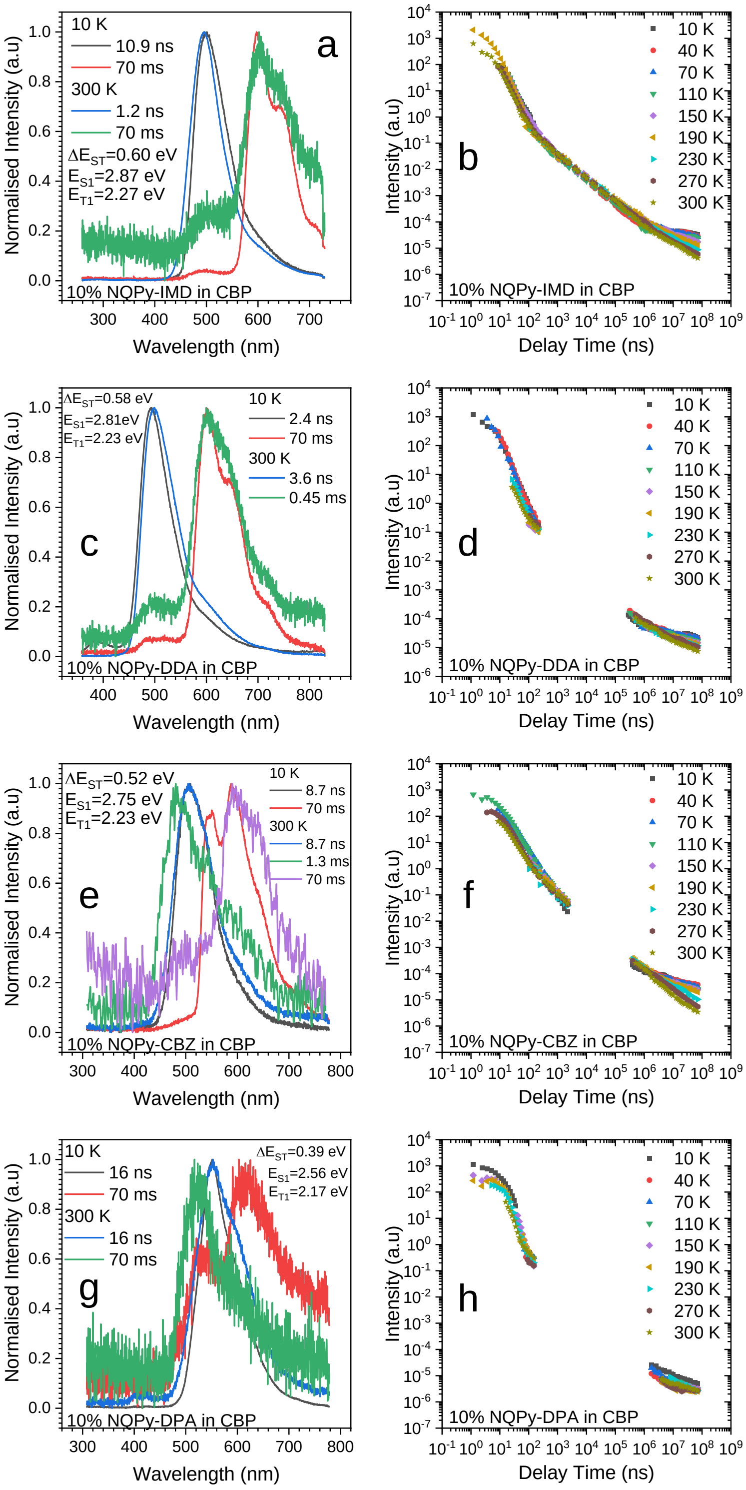

Figure 52. Time-Resolved spectra and the intensity vs. delay time measurements of **NQPy-IMD**, **NQPy-DDA**, **NQPy-CBZ** and **NQPy-DPA** compounds 10 wt% in CBP matrix.

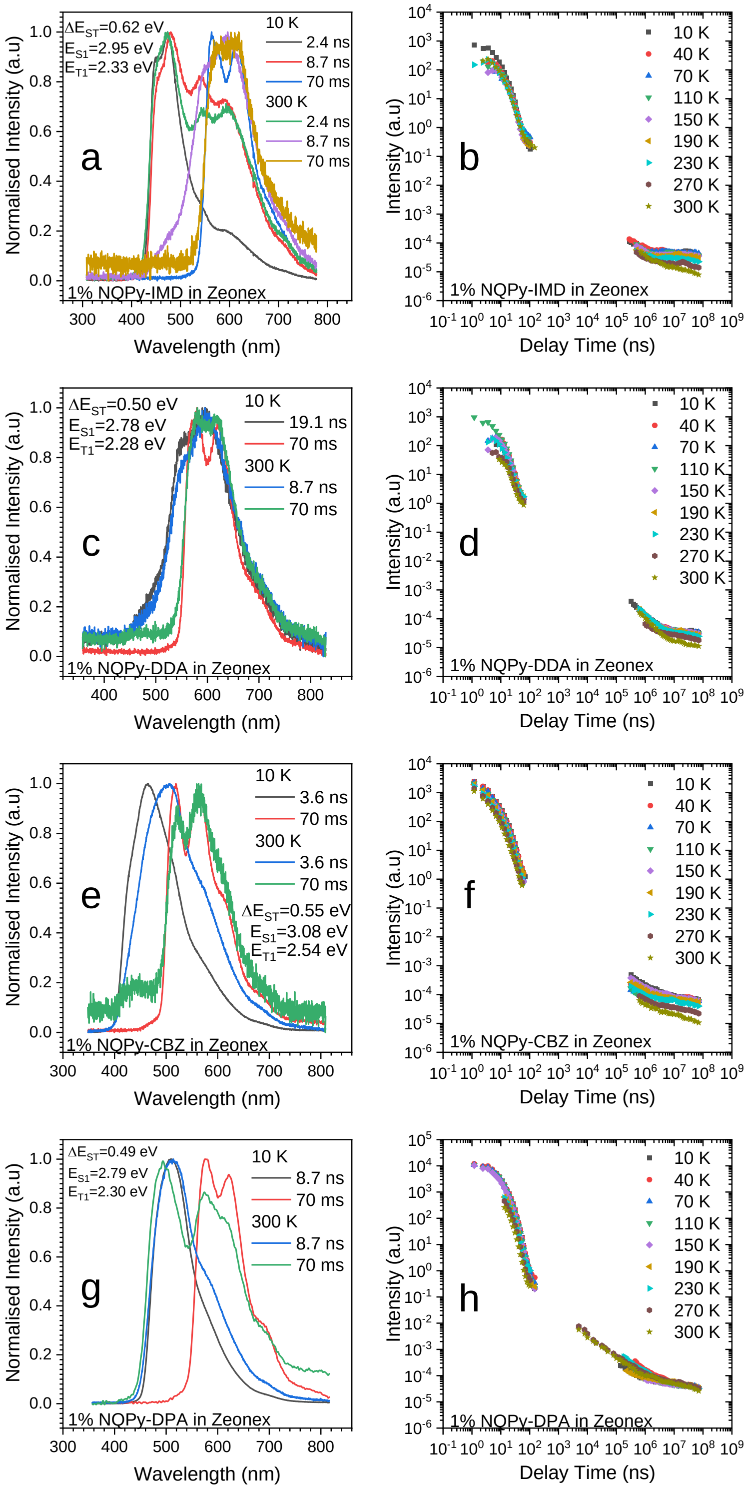

Figure 53. Time-Resolved spectra and the intensity vs. delay time measurements of **NQPy-IMD**, **NQPy-DDA**, **NQPy-CBZ** and **NQPy-DPA** compounds 1 wt% in Zeonex matrix.

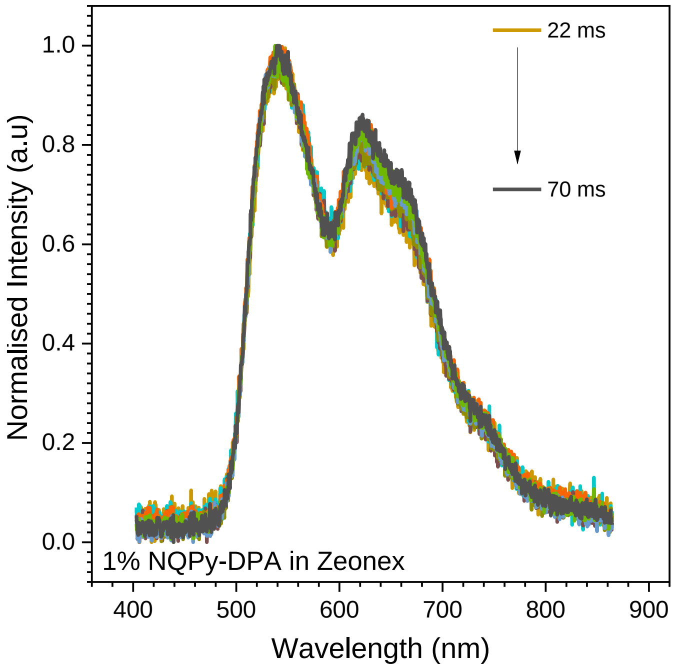

Figure 54. Normalized time resolved spectra at 300 K from 22 ms to 70 ms for 1 % of **NQPy-DPA** in Zeonex matrix.

5.2.5. OLED results for NQPy-donor derivatives

To investigate the applicability of the newly developed materials as TADF OLED emitters, we fabricated solution-processed devices using them as the emissive dopants. The devices 1-8 (**NQPy-PTZ**, **NQPy-PXZ**, **NQPy-DMAC**, **NQPy-DPAC**, **NQPy-DDA**, **NQPy-IMD**, **NQPy-CBZ** and **NQPy-DPA**) are based on a structure ITO / PEDOT:PSS (30 nm) / 10% **NQPy-Donor** + CBP (25 nm) / TPBi (50 nm) / LiF (1 nm) / Al (100 nm). The PEDOT:PSS and the emissive layer were deposited by spin-coating, while the rest using thermal evaporation. The characteristics of the electroluminescent devices are shown in **Figure 55** and summarised in **Table 9**. All devices exhibit a low turn-on voltage, ranging from 4 V to 5 V (**Figure 55c**)**.** The emission colour of the devices varies from red-orange to green, correlating with the strength of the donor moiety attached to the acenaphtopyrido[2,3-b]pyrazine core (**Figure 55d** and **Figure 56**). The slightly bluer and less efficient OLEDs are obtained with emitters displaying slow triplet decay: **NQPy-DDA**, **NQPy-IMD**, **NQPy-CBZ**, and **NQPy-DPA**. The OLEDs displaying redder electroluminescence and higher EQE are made with TADF emitters **NQPy-DMAC**,

NQPy-DPAC, **NQPy-PTZ** and **NQPy-PXZ**. The highest EQE values were obtained for **NQPy-DMAC** and **NQPy-DPAC**, 15.3 % and 8.7 %, respectively. This can be attributed to the most efficient TADF RISC in these compounds in CBP and lesser susceptibility for triplet quenching at higher emitter load. The lower EQE of OLEDs using **NQPy-PTZ** and **NQPy-PXZ** as emitters correlates with the time-resolved photophysics analysis showing lesser TADF efficiency of these two luminophores.

Table 9. Characteristics of OLED devices 1-8.

Device	**Compound**	**EQE$_{max}$ (%)**	**Luminance (cd m^{-2})**	**Turn on (v)**	**Current efficiency (cd A^{-1})**	**FWHM (nm)**	**λ_{em} (nm)**
1	**NQPy-PTZ**	4.6	1461	5.0	5.8	105	596
2	**NQPy-PXZ**	3.5	822	4.0	2.8	125	605
3	**NQPy-DMAC**	15.3	3975	4.2	25.6	79	576
4	**NQPy-DPAC**	8.7	2573	4.2	14.9	83	569
5	**NQPy-DDA**	1.5	655	4.6	2.2	58	489
6	**NQPy-IMD**	0.7	656	4.0	1.2	55	484
7	**NQPy-CBZ**	2.3	971	4.4	3.3	71	492
8	**NQPy-DPA**	1.7	2652	4.3	3.5	87	552

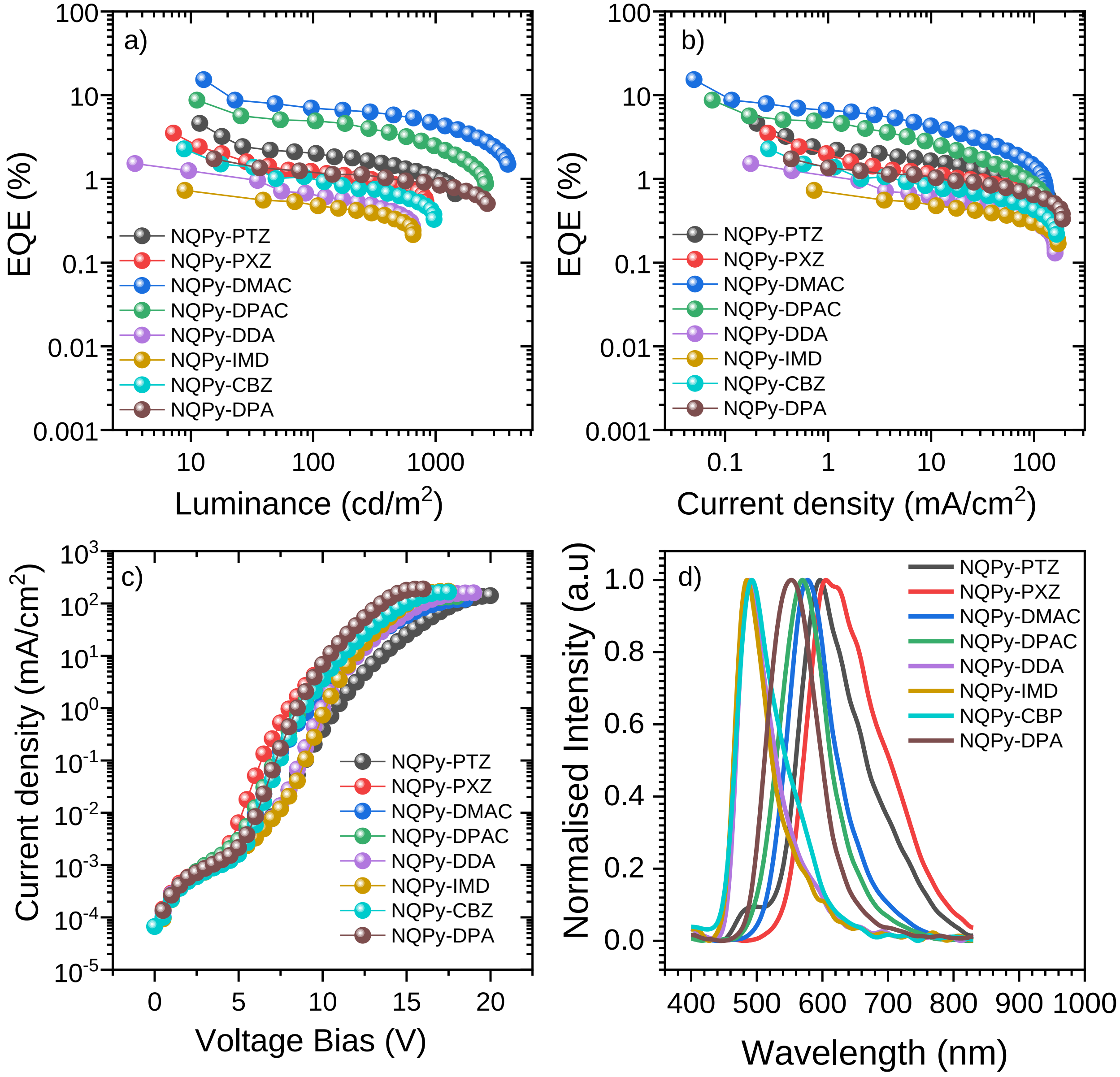

Figure 55. Characteristics of OLED devices: a) EQE vs. luminance. b) EQE vs. current density. c) Current density vs. voltage bias. d) Normalized EL spectra.

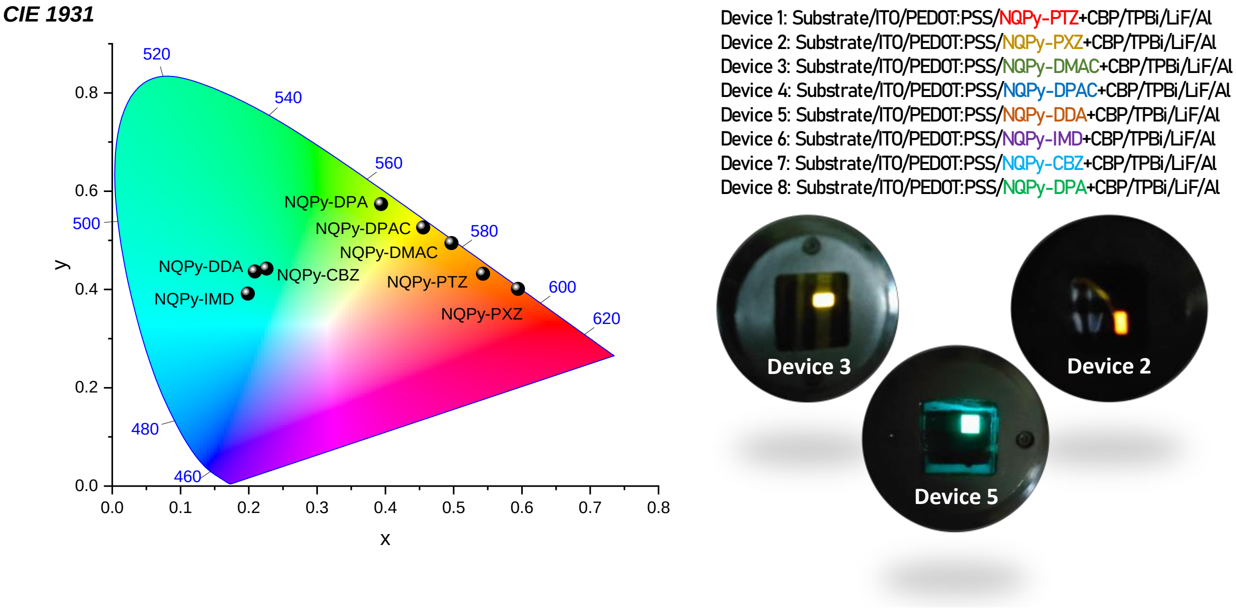

Figure 56. CIE 1931 diagram chromatic coordinates for **NQPy-Donors** electroluminescence in the devices 1-8.

5.2.6. Conclusions

The **NQPy** derivatives were showing multifunctionalities such as TADF, TTA, RTP, AIE and AIEE depending on the donor. The **NQPy-PTZ** and **NQPy-PXZ** compounds were showing a conformers contribution in DF emissions in both matrices. The compounds with **DDA**, **IMD**, **CBZ** and **DPA** showed TTA contributions depending on the matrix and RTP properties. The **NQPy-DPA** was able to present a mix of TADF and RTP emission in Zeonex. The **NQPy-DMAC** and **NQPy-DPAC** were the ones that showed the highest EQE of this series, obtaining impressive 15.9 % and 8.7 %. The emission of the OLEDs varies from 484 nm until 605 nm. These compounds showed better results when compared with the previously published emitters with the same core. This work has contributed to demonstrating versatility of the **NQPy** core and provide good perspectives for these compounds.

5.3. Tris([1,2,4]triazolo)[1,3,5]triazine (TTT) derivatives

The draft of this chapter is under corrections to be submitted in Journal of materials chemistry C. The title of the manuscript is “Multifunctional tris(triazolo)triazine-based emitter with two-TADF, RTP, AIE and AIDF properties”.

A promising strategy is to combine AIE with TADF properties in the same material to create a robust emitter.[101] These materials hold great potential for the development of efficient non-doped OLEDs.[102] Despite their promise and cost-effectiveness, aggregation-induced delayed fluorescence (AIDF) emitters remain relatively scarce in the field.[103,104] Recently, there has been notable interest in the tris([1,2,4]triazolo)[1,3,5]triazine core (**TTT**) due to its planar structure and moderate electron-withdrawing properties, making it a promising acceptor for blue TADF emitters.[105,106] Among the **TTT**-based TADF emitters known, only one has been reported to exhibit green emission. This emitter, referred to as TTT-PXZ,[107] belongs to the D_3A-type category and yields a PLQY of 39.5 %, a small ΔE_{ST} of 0.07 eV, and a delayed fluorescence lifetime of 4.2 µs. When used in an OLED, it achieves an EQE_{max} of 6.2 %. At the same time literature reports demonstrate that phenothiazine (**PTZ**) donor is widely used in the synthesis of luminescent materials and especially those shown to achieve AIE properties.[104]

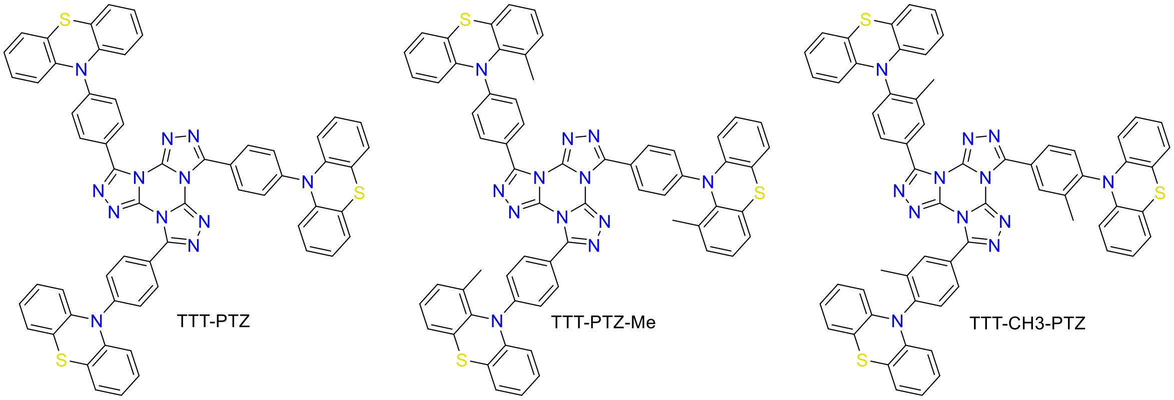

Figure 57. **TTT** derivatives with **PTZ** as donor, **TTT-PTZ**, **TTT-PTZ-Me** and **TTT-CH3-PTZ**

Building on the insights gained from **TTT-PXZ** and the established utility of the **PTZ** donor, the research aims to explore novel avenues in the development of advanced materials with enhanced properties for potential applications in OLEDs and related technologies.

The compounds investigated in this chapter are based on the tris([1,2,4]triazolo)[1,3,5]triazine (**TTT**) acceptor core and phenothiazine as donor. Some of them were modified with a methyl group on either the donor or the phenyl linker part of the structure, see **Figure 57**. The methyl group allows controlling steric hindrance between the donor and the linker (phenyl group), providing more control over the relative configuration between the two units.

Cyclic Voltammetry of TTT derivatives

The voltammograms recorded for these derivatives, **Figure 58**, indicate a low variation in HOMO and LUMO energy between **TTT-PTZ** and **TTT-CH3-PTZ** while the addition of methyl group at the donor affected the HOMO of the compound while the LUMO stayed at a bit lower energy. The values of HOMO and LUMO obtained against the Fc/Fc$^+$ were -5.29 eV and -2.39 eV (**TTT-PTZ**), -5.68 eV and -2.42 eV (**TTT-PTZ-Me**), and -5.27 eV and -2.39 eV (**TTT-CH3-PTZ**). Reduction process was recorded inside of glove box and under argon atmosphere due to the low reduction potential being outside of the electrochemical window for the analysis using dichloromethane with tetrabutylammonium tetrafluoroborate as the supporting electrolyte. The study in the glovebox was done with 100 mM tetrabutylammonium hexafluorophosphate in THF instead. While that the oxidation process was performed with tetrabutylammonium tetrafluoroborate as electrolyte in DCM as solvent. The CV analysis were carried out by Ph.D. Aleksandra Nyga from our research group.

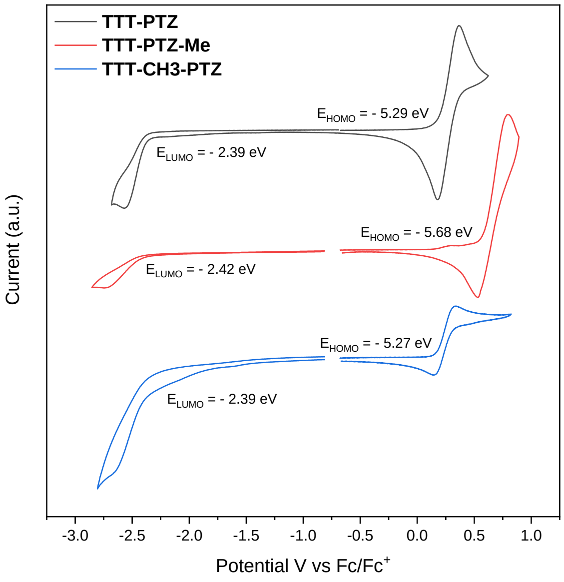

Figure 58. Voltammograms of **TTT-Donor** molecules recorded with 1 mM of the analyte using tetrabutylammonium tetrafluoroborate 100 mM in CH_2Cl_2 as the supporting electrolyte for oxidation. The reduction was performed in 100 mM tetrabutylammonium hexafluoroborate as electrolyte in a glovebox in THF.

5.3.1. Steady State Spectroscopy of TTT derivatives

Absorption spectra of the three derivatives are similar to each other, the energetically highest absorption band at ~245 nm can be assigned to the π-π* LE transition from the longer wavelength band at ~315-330 nm can be attributed to π-π* LE transition of PTZ donor.[108,109] Besides that a weak CT absorption bands can be observed at ~380-480 nm.

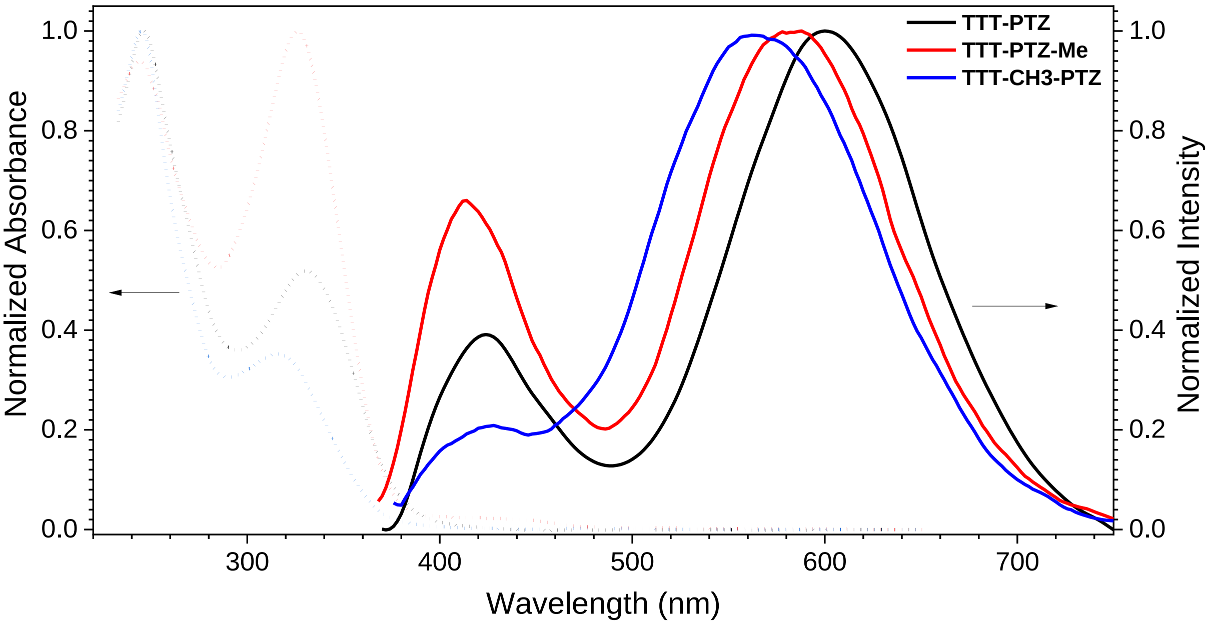

Figure 59. Steady state absorption and emission of compounds **TTT-PTZ**, **TTT-PTZ-Me** and **TTT-CH3-PTZ** in DCM.

Solvatochromism behaviour of the TTT derivatives is shown in **Figure 60**. The results for the compound **TTT-PTZ** presented in **Figure 60a** show the emission turning from a structured emission in MCH to a Gaussian shape already in TOL with appearance of a second, higher energy emission band in THF and DCM. Interestingly, this higher energy emission is present in all investigated solvents for **TTT-PTZ-Me**. In **TTT-CH3-PTZ** the high energy signal occurs only in DCM. A redshift from MCH to DCM can be observed to be 518 – 600 nm (2638 cm^{-1}) for **TTT-PTZ**, 497 – 585 nm (3027 cm^{-1}) for **TTT-PTZ-Me**, and 507 – 593 nm (2860 cm^{-1}) for **TTT-CH3-PTZ**.

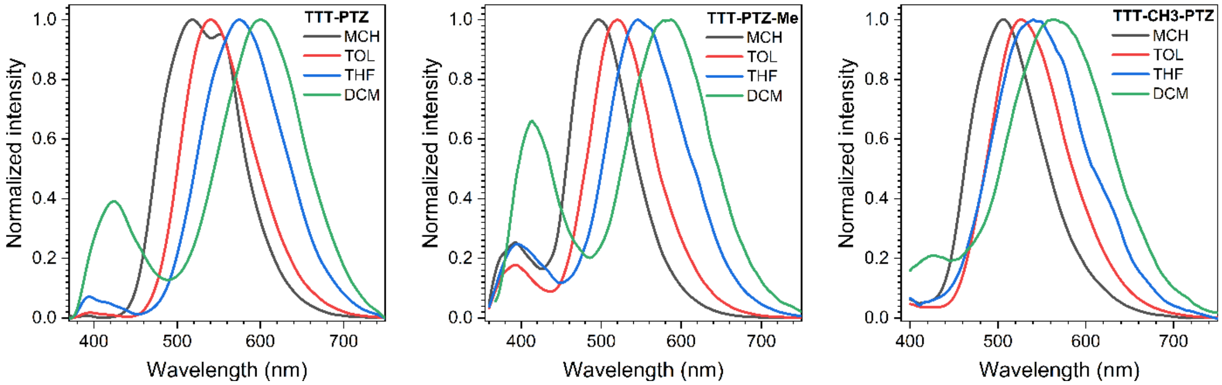

Figure 60. Solvatochromism of (a) **TTT-PTZ**, (b) **TTT-PTZ-Me** and (c) **TTT-CH3-PTZ** in MCH, TOL, THF and DCM.

5.3.2. AIE study of TTT derivatives

The aggregation study of the three luminophores in water/THF mixtures at different concentrations is showed in **Figure 61**. The results confirm aggregation induced enhanced emission properties in **TTT-PTZ** and **TTT-CH3-PTZ**. The molecules are slightly emissive in pure THF, but with the addition of water to 20 % and 40 % one observes a decrease in the emission often called polarity-induced quenching of the CT states. Upon further increase of the water fraction to 60 and 80% (with further increase at f_w = 90 %) it is possible to observe an increase of the PL intensity in relation to lower water fractions. In addition, the PL maximum in **TTT-PTZ** is slightly blue shifted at f_w = 90 % in comparison to pure THF which can be associated with a reduction in degrees of freedom in aggregates compared with the molecules in solution. The change in emission intensity as a function of water content f_w is shown in **Figure 62**. It is possible to observe that for **TTT-PTZ** displays higher relative increase of intensity reaching up to 14.7 fold relative to pure THF. At the same time, for **TTT-CH3-PTZ** the overall change was much less pronounced at only 1.5 fold.

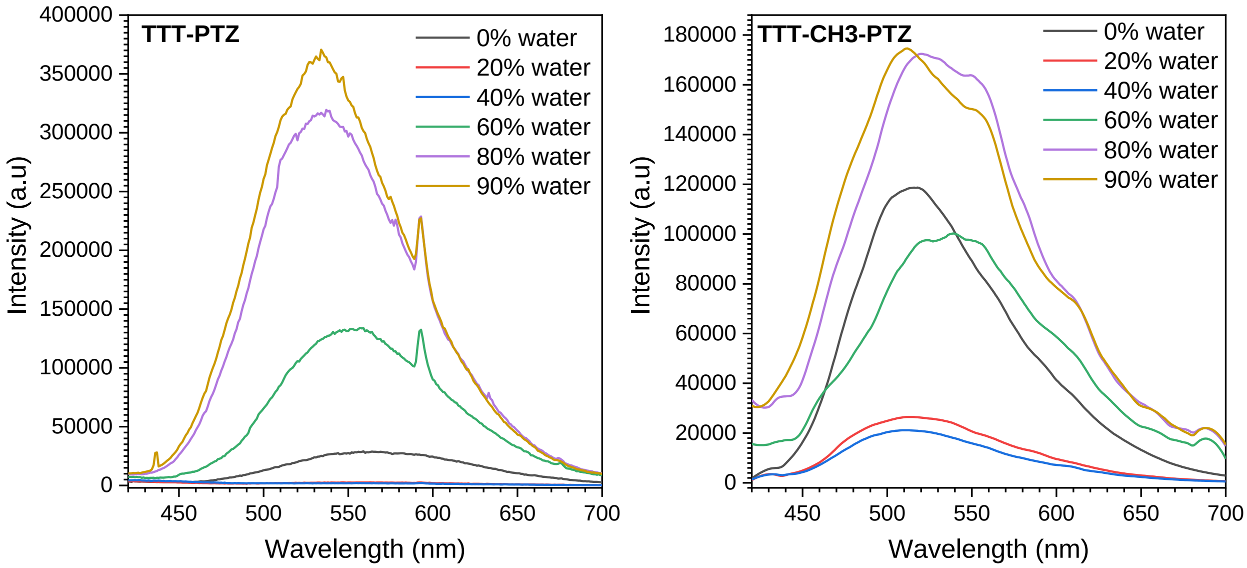

Figure 61. AIE study of compounds **TTT-PTZ** and **TTT-CH3-PTZ** in water/THF solution of 0.1 mM and proportions of 0, 20, 40, 60, 80, 90 % of water.

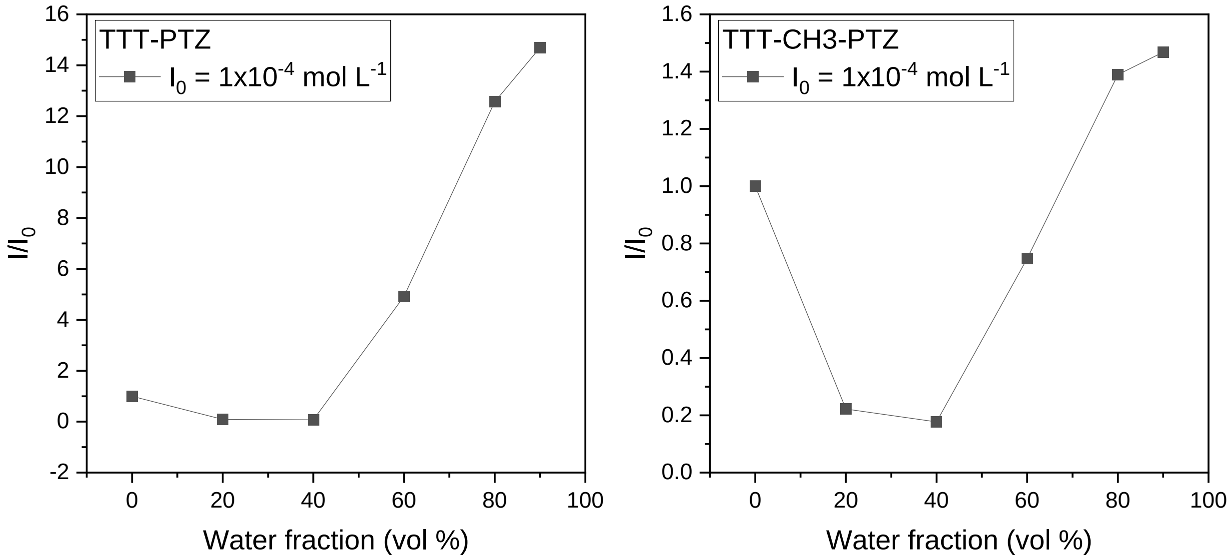

Figure 62. Relative intensity of emission for compounds **TTT-PTZ** and **TTT-CH3-PTZ** in 0, 20, 40, 60, 80 and 90 % of water in THF at 0.1 mM.

5.3.3. Time-resolved photoluminescence in solution

The time-resolved photoluminescence analysis was first performed to study the behaviour of **TTT-PTZ** in aggregated and non-aggregated form in water/THF mixtures. Time-correlated single photon counting (TCSPC) technique was used for this purpose and the results are presented in **Figure 63**. It is possible to observe a clear increase in the intensity of a long-lived component originating from aggregates which is not present in the THF solution. As the experiment is conducted in air-equilibrated conditions and hence one does not expect any long-lived photoluminescence in a solution, yet aggregates as less permeable to oxygen can display strong delayed fluorescence.

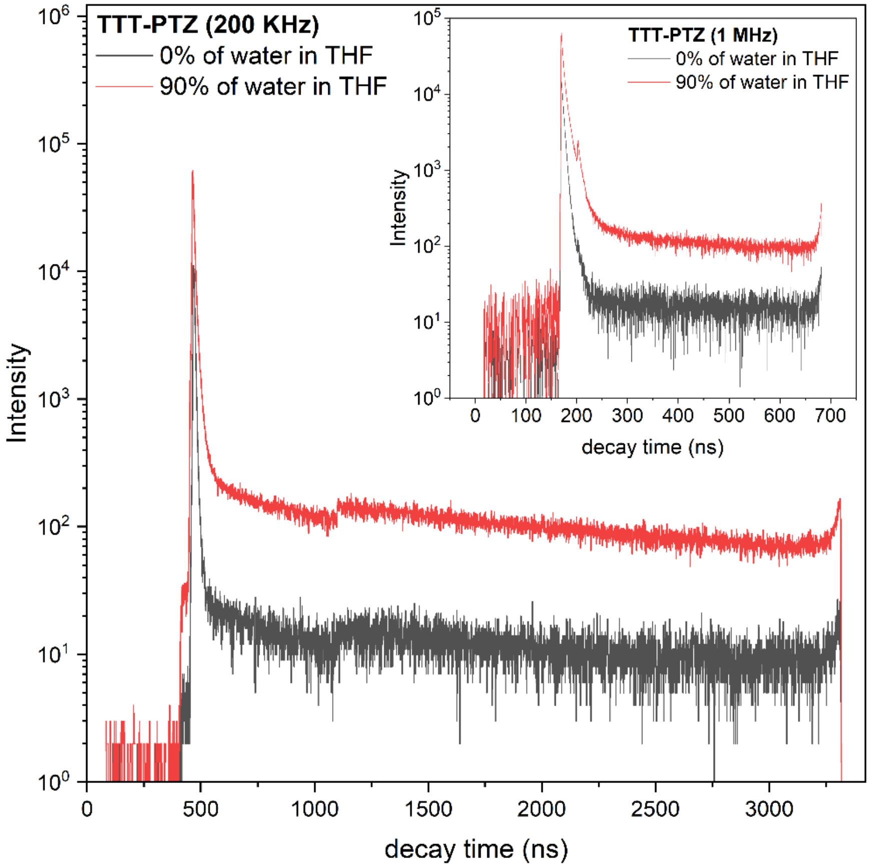

Figure 63. TCSPC analysis of **TTT-PTZ** in 0 and 90% of water in THF at 0.1 mM

5.3.4. Time-resolved photoluminescence in solid

In next step the compounds were analysed in solid films in Zeonex and CBP and the results are presented in

Figure 64, **Figure 65** and **Figure 66**. These results show the presence of a very elaborated luminescence phenomenon and will be discussed in detail in the next paragraph.

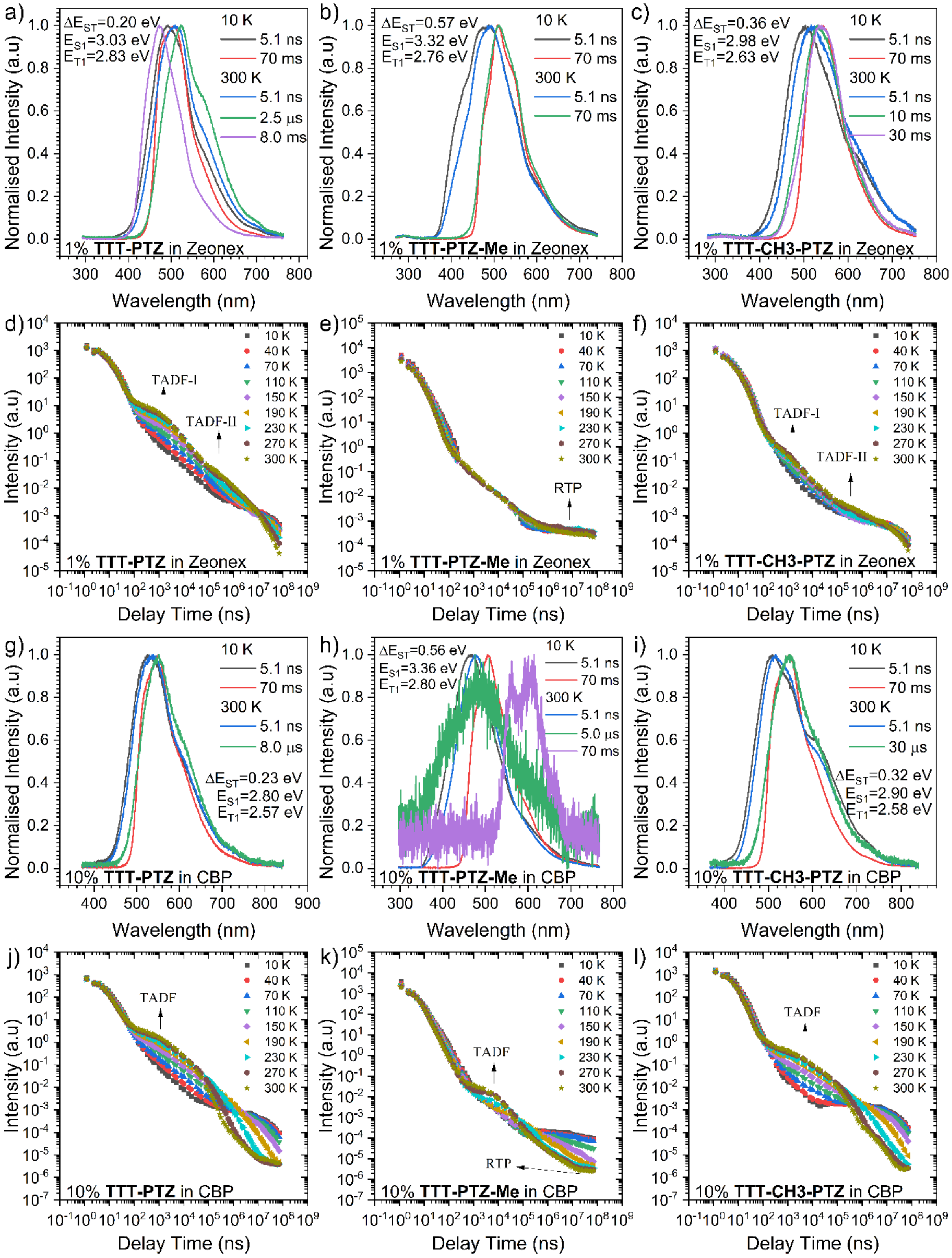

Figure 64. Time-resolved photoluminescence analysis for the compounds **TTT-PTZ**, **TTT-PTZ-Me** and **TTT-CH3-PTZ** in Zeonex and CBP matrix.

Compound **TTT-PTZ** presents a variation in the PF and TADF emission probably due to the presence of three phenothiazine donors connected to the core. It is well described in literature that phenothiazine assumes two conformers: *quasi*-equatorial (eq) and *quasi*-axial (ax) as mentioned before in section 5.1.4.[69,71,74,100] Here, the molecules present three donors, hence there is a possibility of a large variety of conformers present with two possibilities for each donor giving ax-ax-ax, eq-eq-eq, ax-eq-eq and ax-ax-eq conformers and increasing the possibility of a temporal heterogeneity of the. In fact, in a system with three donors there are multiple conformers possibilities. As mentioned before, Data and co-workers showed for a two donor system that eq-eq conformers show lower HOMO-LUMO energy gap, then larger gap is found for eq-ax and then for the ax-ax the gap is the largest.[71]

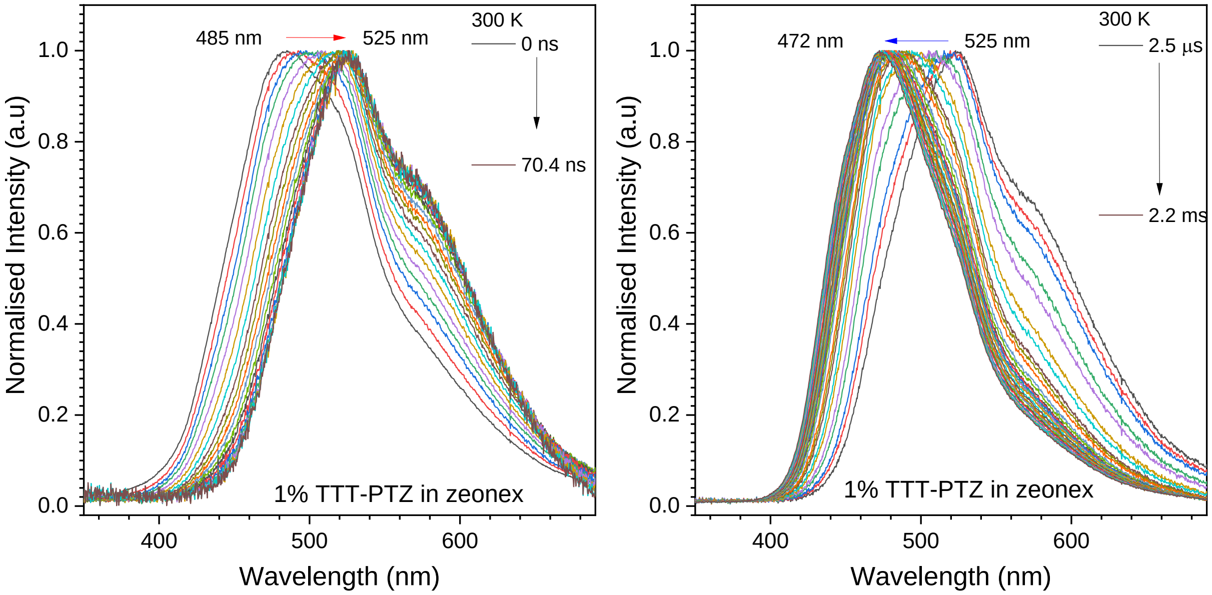

Figure 65. Emission spectrum of 1 % of **TTT-PTZ** in Zeonex matrix at different delay times obtained by ICCD camera device. (a) from 0 to 70.4 ns, referent to the prompt fluorescence emission. (b) from 2.5 µs to 2.2 ms attributed to the TADF emission.

Indeed, for the compound **TTT-PTZ**, the variation in the emission was observed as a red shift in the PF emission, around 40 nm (1539 cm^{-1}) in this case, **Figure 65**. Same behaviour was observed in the TADF emission from 2.5 µs to 2.2 ms but with the blue shift in the emission maximum also around 40 nm (1539 cm^{-1}).[110] Looking into

Figure 64**d** it is possible to observe the change of intensity with temperature in the microsecond to milisecond range which can be attributed to an emission that is clearly dependent of temperature, being indicative of TADF. All numerical data is compiled in the **Table** 10. In addition, the DF/PF for this compound was 9.3 in Zeonex. Analyzing the same compound in CBP matrix it is possible to observe the same behaviour with the graph of intensity vs. delay time, **Figure 64j**, showing a clear temperature dependence of the emission in the microsecond range. In this case there is no shift in the DF spectra in **Figure 66** while the PF emission is redshifted, suggesting a preferential formation of DF from a specific conformer while the PF originates from a mix of conformers. Looking back into the

Figure 64, for the **TTT-PTZ** in CBP it is possible to attribute the emission between 116.9 ns and 79.4 µs as TADF emission. The compound displays a DF/PF ratio of 4.1 and a τ_{DF} of 7.1 µs,

Table 10.

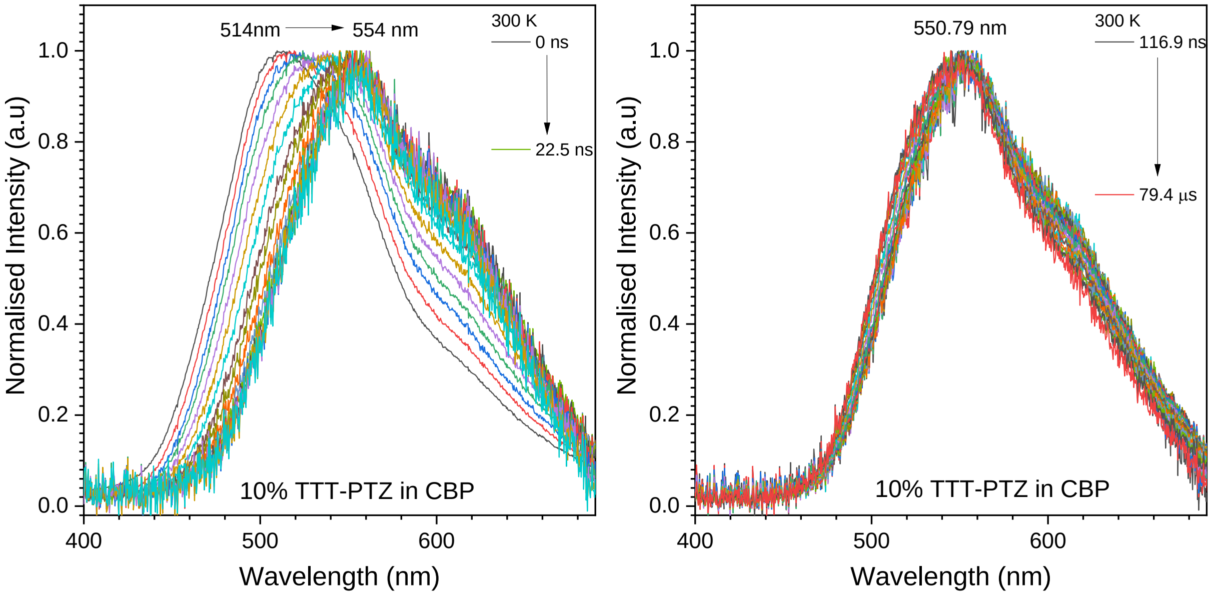

Figure 66. Emission spectrum of 10 % of **TTT-PTZ** in CBP matrix at different delay times obtained with iCCD camera. (a) From 0 ns to 22.5 ns referent to the PF emission. (b) from 116.9 ns to 79.4 µs attributed to the TADF emission.

The compound **TTT-PTZ-Me** presents a different behaviour compared to **TTT-PTZ**, the presence of the methyl group at the position 1 of the donor PTZ affects the planarity between the donor and the acceptor. The TADF properties in Zeonex matrix were not observed as observed in

Figure 64. In **Figure 67a**, it is possible to observe the PF emission showing contributions from different conformers as seen for **TTT-PTZ**, but looking into the milisecond range at **Figure 67b** it is possible to observe that the emission is not changing, suggesting a single emission type from just one conformer. In addition, the emission in the milisecond region displays the same maximum (511 nm) as the most redshifted PF, but the onset of this emission is at lower energy than the PF, matching the characteristics of RTP emission. With this small modification it was possible to achieve RTP properties for this molecule in Zeonex matrix obtaining emission with a τ of 109.6 ms,

Table 10. In addition, the ΔE_{ST} for this compound was much higher than for **TTT-PTZ**, at 0.57 eV and 0.56 eV in Zeonex and CBP matrix, respectively.

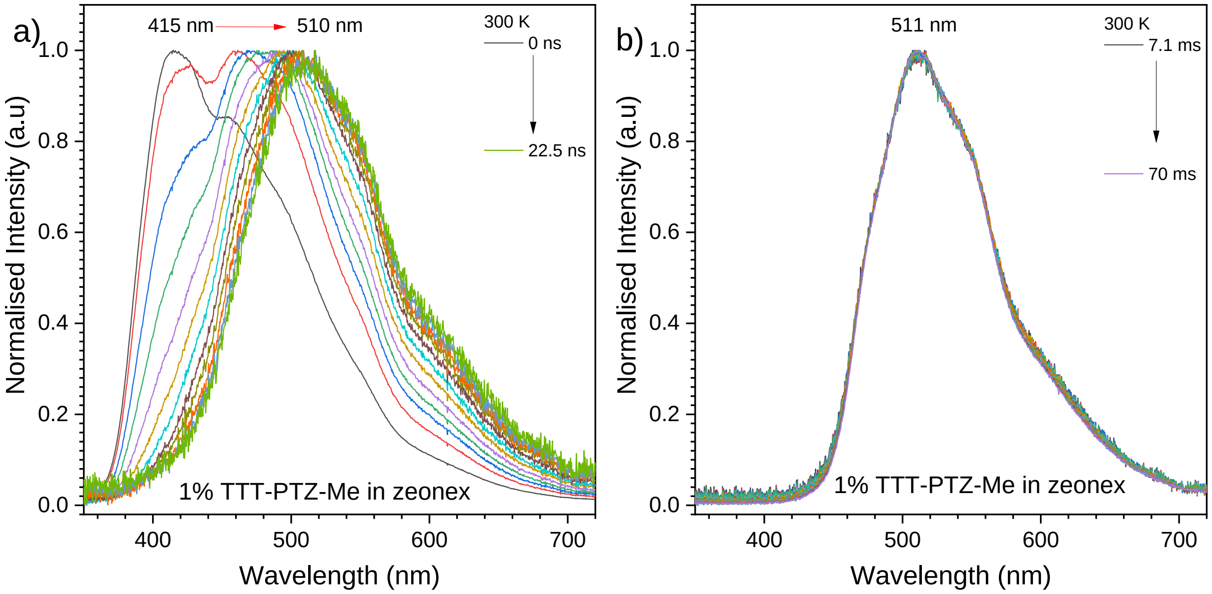

Figure 67. Emission spectrum of 1 % of **TTT-PTZ-Me** in Zeonex matrix at different delay times of PF and DF obtained using iCCD camera. (a) from 0 to 22.5 ns, referent to the PF emission. (b) from 7.1 ms to 70 ms to the TADF emission.

A different observation was made in CBP matrix, **Figure 68**, for **TTT-PTZ-Me** with a faster DF decay and a higher CT state energy than the observed for phosphorescence at 10 K, suggesting the presence of a DF emission but with very low intensity. In the same way the RTP contribution was much less intense in the CBP matrix showing a vibronic spectrum (LE), **Figure 64h**, at lower energy phosphorescence observed at 10 K and, also, with a very low emission intensity. It may suggest a presence of another conformer with lower energetic triplet state, but also may be an indication that the emission from the T_1 state is susceptible to rigidochromic effects. Addition of the methyl group to the donor appears to be detrimental to the TADF properties in both matrices.

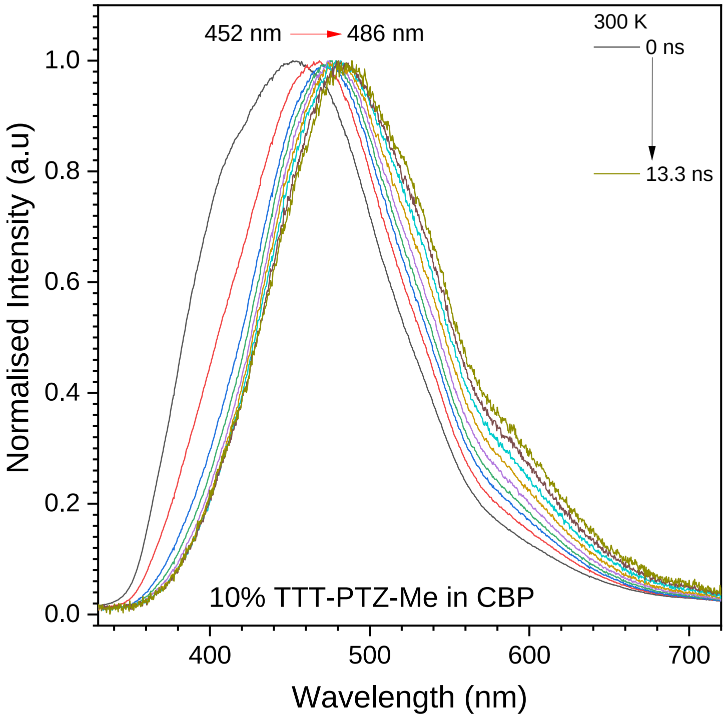

Figure 68. Emission spectra of 10% of **TTT-PTZ-Me** in CBP matrix at different delay times recorded using iCCD camera at timescales from 0 to 13.3 ns.

The next compound, **TTT-CH3-PTZ**, shows the methyl group connected not to the donor but to the phenyl linker at the ortho position in respect to the donor, causing a steric hindrance between the donor and the phenyl ring but lower compared to the methyl group as in **TTT-PTZ-Me**. This modification of the position of the methyl group gives a larger contribution of the DF emission than that observed for **TTT-PTZ-Me**. **TTT-CH3-PTZ** achieves the TADF emission in both matrices as seen in **Figure 69** and **Figure 70**. The redshift observed in the onset values of the emission spectra suggests a similar heterogeneity of the emission energy as observed in **TTT-PTZ** and attributed to the presence of multiple conformers of phenothiazine. These results also suggest a smaller distribution of conformers than that observed for **TTT-PTZ** with much more subtle changes in the time-resolved emission spectra for **TTT-CH3-PTZ**, suggesting that the methyl group affects the distribution of conformers.

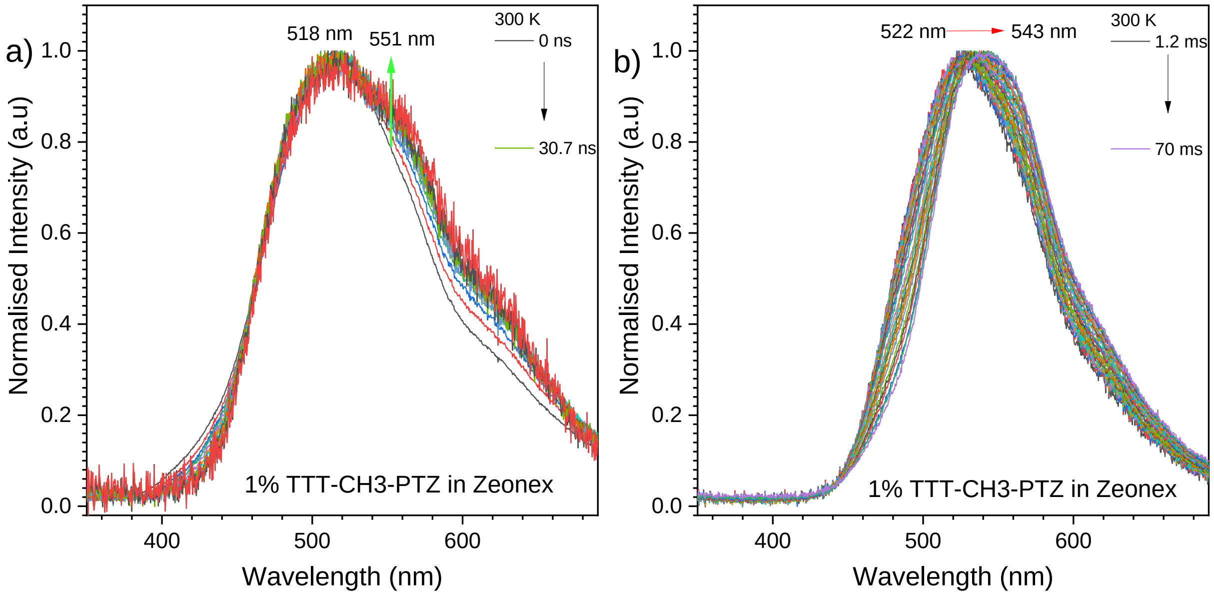

Figure 69. Emission spectrum of 1% of **TTT-CH3-PTZ** in Zeonex matrix at different delay times obtained with an iCCD camera. (a) PF emission from 0 ns to 30.7 ns. (b) TADF emission from 1.2 ms to 70 ms.

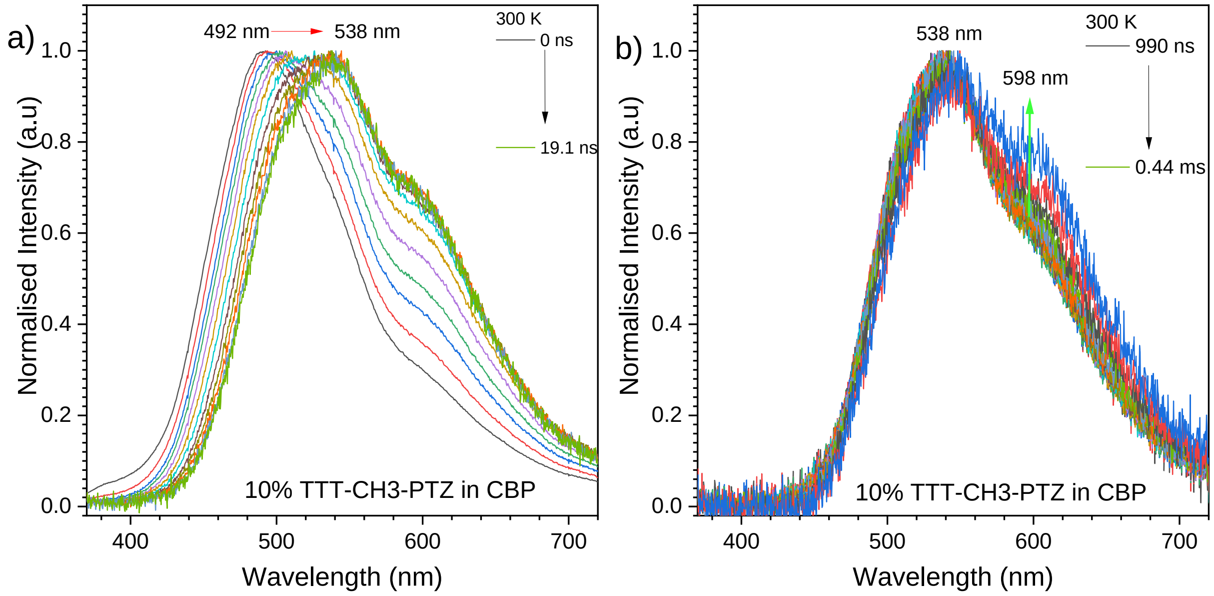

Figure 70. Emission spectrum of 10 % of **TTT-CH3-PTZ** in CBP matrix at different delay times obtained with an iCCD camera. . (a) PF emission from 0 ns to 19.1 ns. (b) TADF emission from 990 ns to 0.44 ms.

The results for the **TTT-CH3-PTZ**, **Figure 70**, in CBP matrix is showing similar behaviour but in oposite way that observed in Zeonex. The PF emission showed at **Figure 70a** a much more pronunced redshift than in DF emission at **Figure 70b**, from 492 nm to 538 nm, a difference of 1738 cm^{-1}. While that, the DF emission remains virtually invariant with delay time. Such observation suggests that the DF emission originates from a single conformer contribution due to the presence of the methyl group and the polar matrix.

Table 10. Photophysical parameters obtained from time-resolved analysis of compounds **TTT-PTZ**, **TTT-PTZ-Me**, and **TTT-CH3-PTZ**.

	λ_{em} [nm][a]	Film[b]	$PLQY_{air}$ [%][c]	τ_{PF} [ns][d]	τ_{DF}[μs][e]	DF/PF or RTP/PF[f]	S_1 [eV][g]	T_1 [eV][g]	ΔE_{ST} [eV][h]	k_{rISC} [s^{-1}]
TTT-PTZ	510	Zeonex	27.1	8.3 ± 0.5	1.4±0.1	9.33	3.03	2.83	0.20	6×10^{6}
	538	CBP	5.3	6.0 ± 0.5	7.1±0.2	4.11	2.80	2.57	0.23	6×10^{5}
	528	Neat	8.9	-	-					-
TTT-PTZ-Me	493	Zeonex	8.9	4.7 ± 0.2	$(1.1\pm0.1)\times10^{5}$*	5.19	3.32	2.76	0.57	-
	476	CBP	14.9	4.4 ± 0.2	4.8±0.5	0.11	3.36	2.80	0.56	2×10^{4}
	478	Neat	5.9	-	-					-
TTT-CH3-PTZ	517	Zeonex	1.7	7.7 ± 0.3	2.6±0.4	4.71	2.98	2.63	0.36	2×10^{6}
	514	CBP	1.9	5.2 ± 0.3	40±1	1.41	2.90	2.58	0.32	4×10^{4}
	504	Neat	1.0	-	-					-

[a] Photoluminescence maximum. [b] Doped ratio Zeonex: 1 wt%, CBP: 10 wt%. [c] Photoluminescence quantum yield. [d] Prompt fluorescence lifetime in the host, monoexponential decay. [e] Delayed emission lifetime in the host, mono or biexponential decay. [f] Delayed fluorescence (DF) or room temperature phosphorescence (RTP) to prompt fluorescence (PF) ratio in the host. [g] Singlet and triplet energy in host. Error ± 0.03 eV. [h] Singlet-triplet energy gap. Error ± 0.05 eV. *RTP emission

5.3.5. OLED results for TTT derivatives

OLED devices were prepared using the CBP matrix with 10 % of **TTT** compounds as the emitting layer which was deposited by spin coating. First PEDOT:PSS was deposited by spin coating on top of the ITO/glass substrate which followed with the emitting layer. The next layers were deposited by evaporation: TPBi, LiF, and Aluminium. The structure of devices 1-3 was: ITO / PEDOT:PSS (30 nm) / 10 % **TTT derivatives** + CBP (25 nm) / TPBi (50 nm) / LiF (1 nm) / Al (100 nm). Hence produced devices 1, 2 and 3 use emitters **TTT-PTZ**, **TTT-PTZ-Me**, and **TTT-CH3-PTZ**, respectively. While, structure of device 4 was ITO / PEDOT:PSS (30 nm) / **TTT-PTZ** (25 nm) / TPBi (50 nm) / LiF (1 nm) / Al (100 nm). The results are showed in **Figure 71** and compiled in **Table 11**. The device 1 in comparison to the device 4 showed better results achieving maximum EQE of 12.4 % vs.

3.0 % for the neat **TTT-PTZ** film (device 4). Addition of a methyl group in the donor affected the EQE decreasing it to 1.7% (**TTT-PTZ-Me**) while the modification in the phenyl spacer gave 7.4 % (**TTT-CH3-PTZ**). All devices showed an electroluminescence FWHM above 100 nm. The devices 1 and 4 showed the highest luminance of 3350 cd m^{-2} and 1549 cd m^{-2}, respectively.

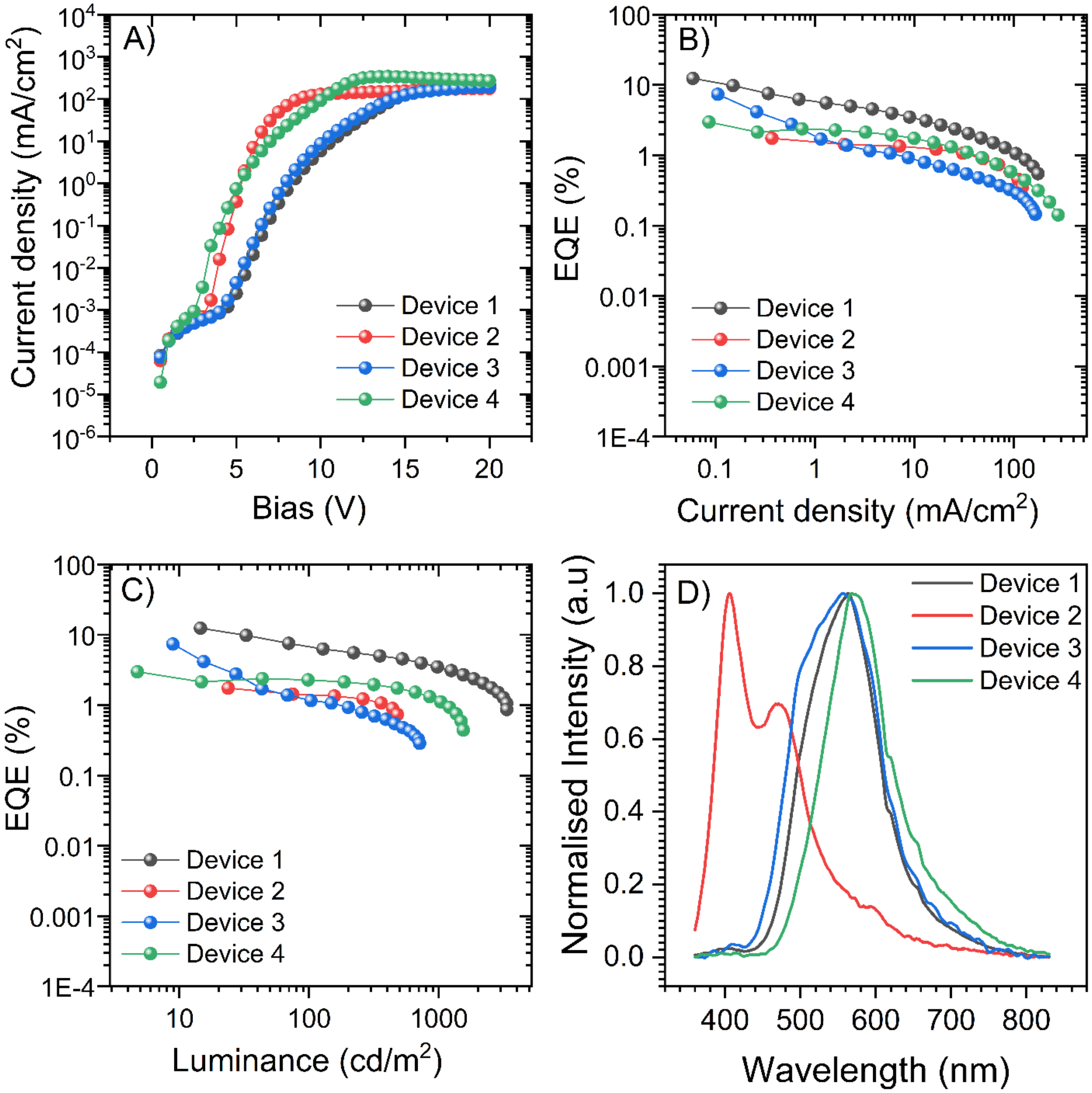

Figure 71. Electroluminescent characteristics of OLED devices 1-4. a) Current density *vs.* bias. b) EQE vs. Current density. c) EQE vs. Luminance. d) Normalized electroluminescence spectra.

Table 11. Characteristics of OLED devices 1-4.

Device	Compound	Host	EQE$_{max}$ (%)	Luminance (cd m^{-2})	Turn on (V)	Current efficiency (cd A^{-1})	FWHM (nm)	λ$_{emiss}$ (nm)
1	**TTT-PTZ**	CBP	12.4	3350	4.2	24.5	112	564
2	**TTT-PTZ-Me**	CBP	1.7	479	3.0	6.4	116	406
3	**TTT-CH3-PTZ**	CBP	7.4	711	3.9	8.4	131	556
4	**TTT-PTZ**	-	3.0	1549	2.5	5.5	100	568

5.3.6. Conclusions

In this study, was presented an investigation of a multifunctional emitter exhibiting AIEE, two TADF processes, AIDF, and RTP characteristics. The introduction of methyl groups into the donor or in the phenyl spacer of the emitters significantly influenced their TADF, RTP, and AIE properties. It demonstrates another approach for fine-tuning the luminescent behaviour by switching between RTP and TADF. In addition, the **PTZ** conformers were observed in all compounds and the methyl group added in **TTT-PTZ-Me** and in **TTT-CH3-PTZ** restricted the formation of conformers depending of the matrix. Furthermore, to the best of my knowledge, **TTT-PTZ** represents the first example of a **TTT**-based emitter combining TADF, AIEE, and AIDF properties within a single compound. These target emitters were employed in solution-processed OLEDs, resulting in EQE values of 12.4 %, 1.7 %, 7.4 %, and 3.0 % for **TTT-PTZ**, **TTT-PTZ-Me**, **TTT-CH3-PTZ** doped in CBP and non-doped **TTT-PTZ**-based devices, respectively. This investigation clearly opens new possibilities for the design of highly efficient organic TADF-active multifunctional emitters in the future.

5.4. Dibenzo[a,j]phenazine (JAP-Si derivatives)

The results presented in this chapter have been published as:

T. Hosono, **N. O. Decarli**, P. Z. Crocomo, T. Goya, L. E. de Sousa, N. Tohnai, S. Minakata, P. de Silva, P. Data and Y. Takeda.

"The regioisomeric effect on the excited-state fate leading to room-temperature phosphorescence or thermally activated delayed fluorescence in a dibenzo[a,j]phenazine -cored donor-acceptor-donor system."

J. Mater. Chem. C, **2022**,10, 4905-4913 **doi:10.1039/d1tc05730h**

Compounds without transition metals are being more and more explored for use as TADF and RTP emitters.[111,112] TADF and RTP properties can be understood as competitive processes as both rely on the same excited triplet state.[113] Materials that show ΔE_{ST} between 0.3 eV and 0.6 eV can usually show both emissions.[114] Dual emissive molecules may be used in different types of applications, such as emitters of white OLEDs where they cover a broad area of the visible spectrum.[115] Said that, the exploration of positional substituted organic compounds have gained attention due to the possibility to increase desirable properties and improve the EQE in OLED.[116]

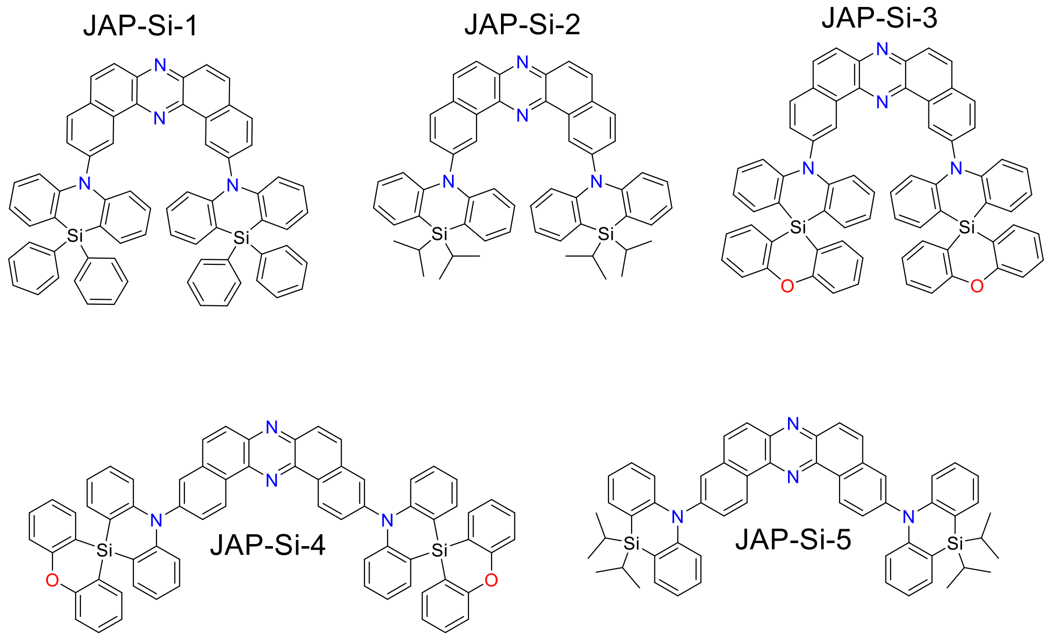
JAP-Si-1
JAP-Si-2
JAP-Si-3
JAP-Si-4
JAP-Si-5

Figure 72. Dibenzo[a,j]phenazine derivatives synthesized by Takeda's research group.

In case of emitters the changes in steric hindrance can affect the luminescent properties with fine tuning between TADF and RTP behaviour being possible.[117] The regioisomeric compounds shown in **Figure 72**, were studied in this chapter.

5.4.1. Cyclic Voltammetry of JAP derivatives

Figure 73 show the cyclic voltammograms for **JAP-Si** compounds. The results can be better understood when separated into groups by structural similarity. The compounds **JAP-Si-1**, **JAP-Si-2** and **JAP-Si-3** are substituted at the innermost positions (2,12) of the acceptor but with different donors. Compounds **JAP-Si-4** and **JAP-Si-5** are substituted in the outer position (3,11), but with two different donors. It is possible to compare the effect of substitution between isomeric **JAP-Si-3** and **JAP-Si-4** compounds, for example. The results show an increase in the LUMO energies in order **JAP-Si-1** < **JAP-Si-2** < **JAP-Si-3** with change of the donor. The same behaviour is observed for the **JAP-Si-4** and **JAP-Si-5**, with the compound with SDAO showing the higher LUMO. In addition substitution at position 2,12 (**JAP-Si-3**) increases the energy of HOMO and LUMO by a factor of 0.1 eV in comparison to the position 3,11 (**JAP-Si-4**) when the donor 5*H*-spiro[dibenzo[b,e][1,4]azasiline-10,10'-dibenzo[b,e][1,4]oxasiline] (**SDAO**) is used. An opposite effect was observed for the donor containing isopropyl as substitution in positions 3,11 (**JAP-Si-5**) showed a higher HOMO and LUMO by around 0.2 eV in relation to the 2,12 (**JAP-Si-2**) positions. These effects are contradictory due to the first case involving a spatially large donor thus the vicinity of the two donors in positions 2,12 produces a significant steric hindrance. While the surrounding of donors in position 3,11 is much less crowded. In the second case, the less voluminous donor does not experience significant steric hindrance effects, and the electronic conjugation between the donors and each of the heterocyclic nitrogen atoms is different in each case. For the derivative substituted at 2,12 positions the conjugation is more effective with the upper nitrogen atom, while for positions 3,11, the conjugation is more effective with the lower nitrogen atom (as they appear in the figure above). **JAP-Si-3** and **JAP-Si-4** show the largest energy gap (2.39 eV), followed by **JAP-Si-1** (2.34 eV), **JAP-Si-5** (2.32 eV), and **JAP-Si-2** (2.27 eV).

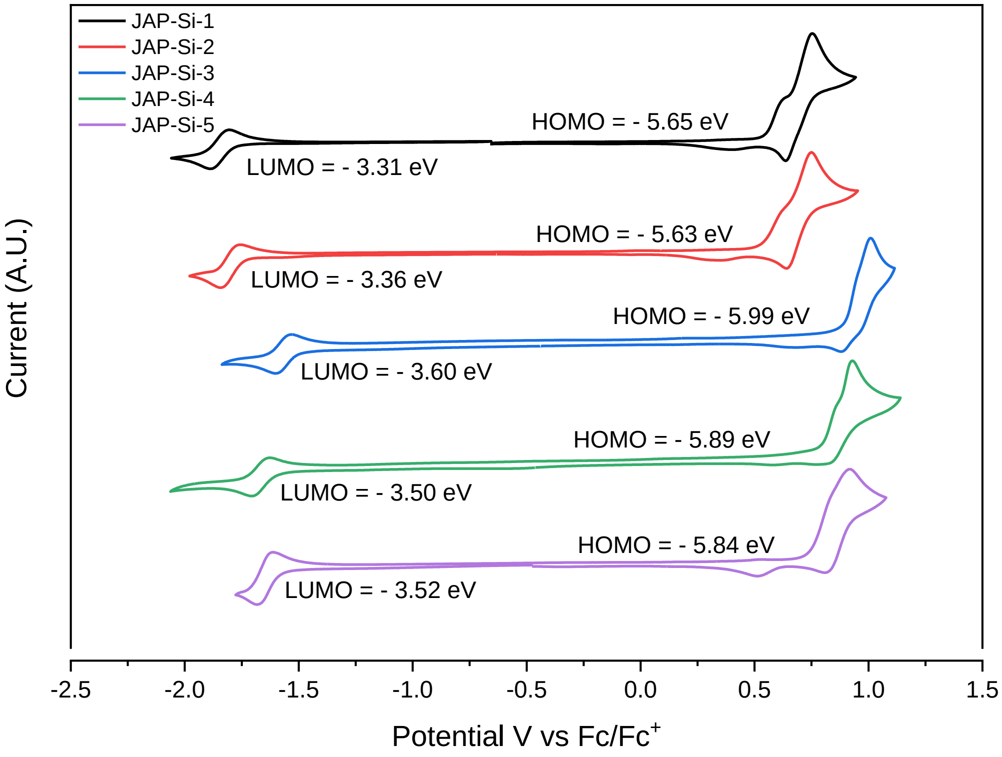

Figure 73. CV with 1 mM of **JAP-Si** compounds in 100 mM tetrabutylammonium tetrafluoroborate.

5.4.2. Steady state spectroscopy of JAP derivatives

The steady state absorption and photoluminescence results are presented in **Figure 74**. They show a redshift from toluene through THF to DCM indicating a CT character of the excited state. The extent of the positive solvatochromic shift can be observed in the following order: **JAP-Si-5** > **JAP-Si-4** > **JAP-Si-2** > **JAP-Si-3** > **JAP-Si-1** indicating a higher influence of polarity on the 3,11 substituted acceptor than in the case of 2,12 substitution. PLQY of these molecules was measured in all three solvents indicated above in air-equilibrated conditions. The highest PLQY values were obtained for toluene solutions with exception of **JAP-Si-5** which gives a higher PLQY in THF solution. A different observation was made about **JAP-Si-3** which showed a higher PLQY in TOL in comparison with the positions isomer **JAP-Si-4**. All that information is compiled in **Table 12.** Steady state emission properties for the **JAP-Si-X** compounds in different solvents.

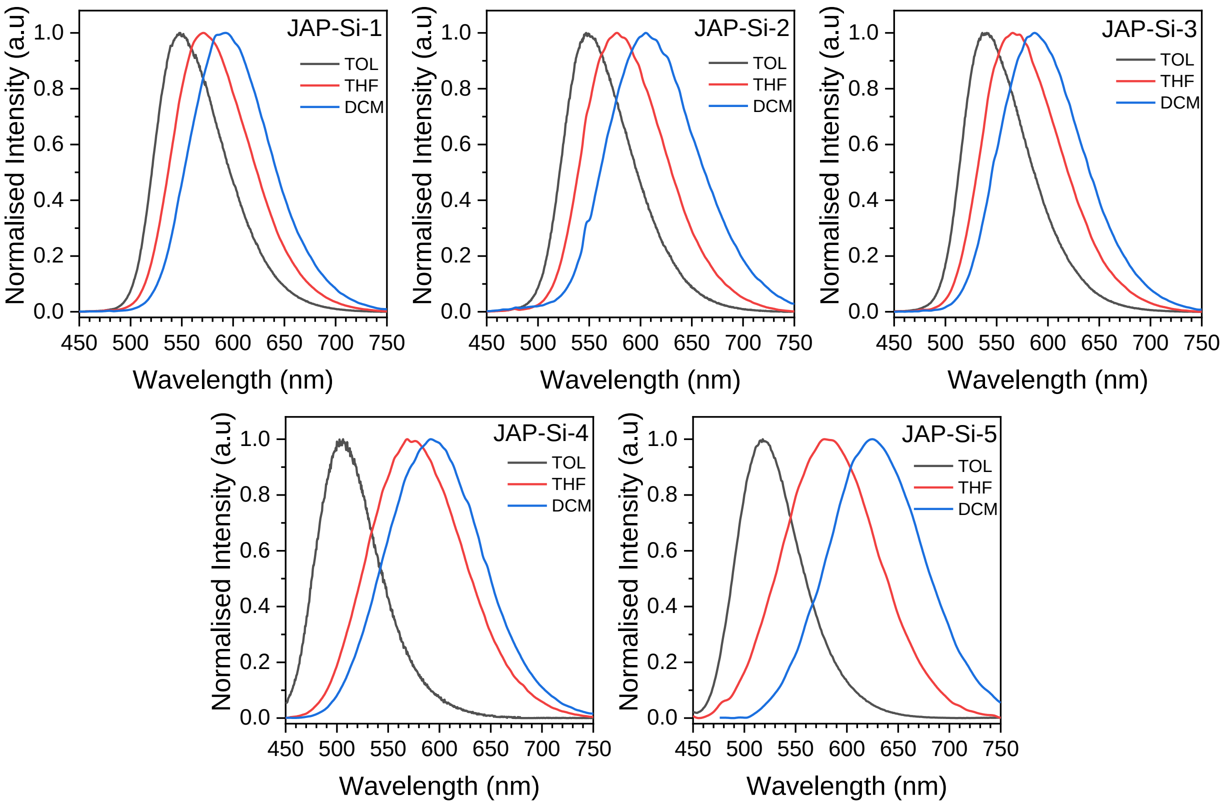

Figure 74. Emission spectra for **JAP-Si-X** derivatives in DCM, THF and Toluene, respectively.

Table 12. Steady state emission properties for the **JAP-Si-X** compounds in different solvents.

	Emission (nm)			**red shift (cm^{-1})**		**PLQY (%)$_{air}$**		
Compound	**DCM**	**THF**	**TOL**	**TOL → DCM**	**THF → DCM**	**DCM**	**THF**	**TOL**
JAP-Si-1	593	571	548	1385	650	6.9	12.4	23.3
JAP-Si-2	605	577	548	1719	802	3.4	6.2	7.4
JAP-Si-3	587	566	541	1449	632	3.4	6.4	18.8
JAP-Si-4	592	568	505	2910	714	4.8	7.4	16.6
JAP-Si-5	625	578	518	3305	1301	5.9	12.4	10.7

The PLQY and emission spectra in the film were recorded using 1 % of **JAP-Si-X** derivatives doped in Zeonex or 10 % in CBP. The PLQYs were measured under ambient conditions, and a comparison with the vacuum emission results allowed for estimating the PLQY in a vacuum. This estimation was achieved by multiplying the PLQY by the ratio of degassed emission to emission under ambient conditions. The results are summarized in Table 13.

Table 13. Emission maximum for the derivatives in the three matrix and their PLQY in air and vacuum conditions.

Comp.	λ em (nm)	HOTS	$\phi_{air}/\phi_{vac.}$#
JAP-Si-1	536	Zeonex	27.4/30.7
	559	CBP	38.7/43.9
JAP-Si-2	525	Zeonex	6.3/11.8
	554	CBP	32.5/35.4
JAP-Si-3	533	Zeonex	9.3/10.3
	535	CBP	25.8/27.8
JAP-Si-4	477	Zeonex	6.5/7.2
	505	CBP	15.3/16.8
JAP-Si-5	483	Zeonex	6.5/9.8
	523	CBP	18.6/37.2

the vacuum PLQY was estimated by the PLQY in air multiplied by the ratio between emission in air and at vacuum.

The emission maximum has shifted with an increase in matrix polarity, mirroring the solvatochromism observed in liquid solutions. In all derivatives, the vacuum emission exceeded the emission under ambient conditions, indicating an influence of oxygen that quenches the emission, with a contribution from the triplet excited state, as discussed previously. Consequently, time-dependent analyses were conducted to gain a better understanding of the phenomena occurring in each compound.

5.4.3. Time dependence analyses of JAP-Si derivatives

With time-resolved photoluminescence analyses it is possible to understand the photophysical properties of each of the compounds. The data are compiled in **Table 14** and the results are shown in **Figure 75**, **Figure 76**, **Figure 77**, **Figure 78**, and **Figure 79**. These results will be showed in groups of emitters showing similar properties. Starting with the analyses of **JAP-Si-5** in the three matrixes it is possible to observe two different behaviours. In Zeonex matrix, **Figure 75a**, the behaviour is showing a TADF process that mixes with RTP at longer delay times as it is possible to observe by the presence of shoulders in the delayed fluorescence which appear in the same position as phosphorescence at low temperature. While in CBP matrix, **Figure 75b**, the compound shows a purely TADF behaviour with lower ΔE_{ST} in this matrix. The shoulders that were present in the Zeonex matrix are not present in CBP, indicating that the emission is purely coming from the S_1.

Table 14. Photophysical parameters obtained from time-resolved analyses.

Compound	Host	τ_{PF} (ns)	τ_{DF} (μs)	τ_{PH} (μs)	DF/PF	S_1 (eV)	T_1 (eV)	ΔE_{ST} (eV)
JAP-Si-1	Zeonex	14.4±0.5	29.1±1.0	-	0.75	2.55	2.28	0.16
	CBP	13.7±0.6	2.0±0.2	-	0.54	2.70	2.37	0.33
JAP-Si-2	Zeonex	13.2±0.6	4.0±0.4	-	1.21	2.65	2.44	0.20
	CBP	12.3±0.6	8.6±0.9	-	1.7	2.46	2.32	0.13
JAP-Si-3	Zeonex	10.2±0.6	33.5±5.9	12138.6± 391.2	1.27	2.47	2.38	0.09
	CBP	8.3±0.2	2.9±0.3	1914.3± 59.7	1.55	2.53	2.41	0.12
JAP-Si-4	Zeonex	6.5±0.2	26.4±1.7	227107.8± 2322.1	1.11	2.81	2.38	0.43
	CBP	5.8±0.2	6.0±0.6	-	0.87	2.74	2.42	0.31
JAP-Si-5	Zeonex	6.9±0.3	7.8±0.3	-	2.31	2.84	2.44	0.40
	CBP	6.8±0.2	1.5±0.1	-	3.80	2.61	2.36	0.25

The results pertaining to **JAP-Si-4** are presented in **Figure 76**. The behaviour of **JAP-Si-4** in both matrixes is very similar to that in **JAP-Si-5**, showing a presence of an equilibrium between TADF and RTP, with dominance of TADF at lower delay times and RTP at longer delay times in Zeonex matrix. In CBP the presence of RTP was not observed. The polar matrix CBP presented a lower ΔE_{ST} as expected in relation to Zeonex due to the stabilization of CT emissions in more polar environments. The ΔE_{ST} in both cases (**JAP-Si-5** and **JAP-Si-4**) in CBP were lower than in Zeonex matrix. The **JAP-Si-5** showed a higher DF/PF ratio than **JAP-Si-4** in both matrices showing more promising properties thinking about OLED applications. These aspects presented show an optimistic view of the donor 10,10-diisopropyl-5,10-dihydrodibenzo[b,e][1,4]azasiline (DDS) containing the silicon with isopropyl chains (DDS) and the donor SDAO, but, in comparison, the first one showed better properties and has a better prospect to be used in further applications.

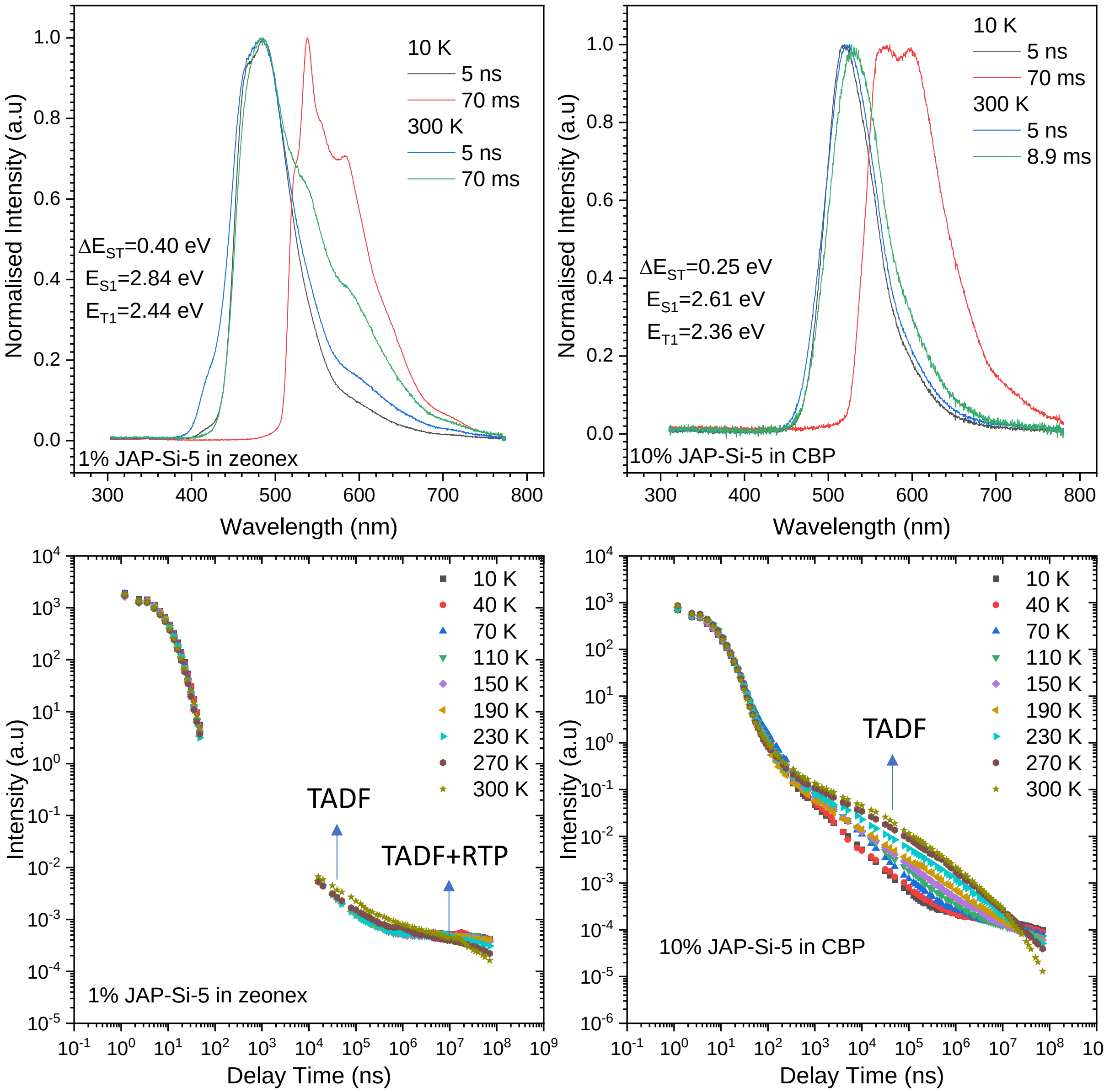

Figure 75. Time-resolved spectra of compound **JAP-Si-5** in different matrices obtained during the intensity vs. delay time measurements The energies corresponding to the emission onsets. a) 1 % in Zeonex and b) 10 % in CBP.

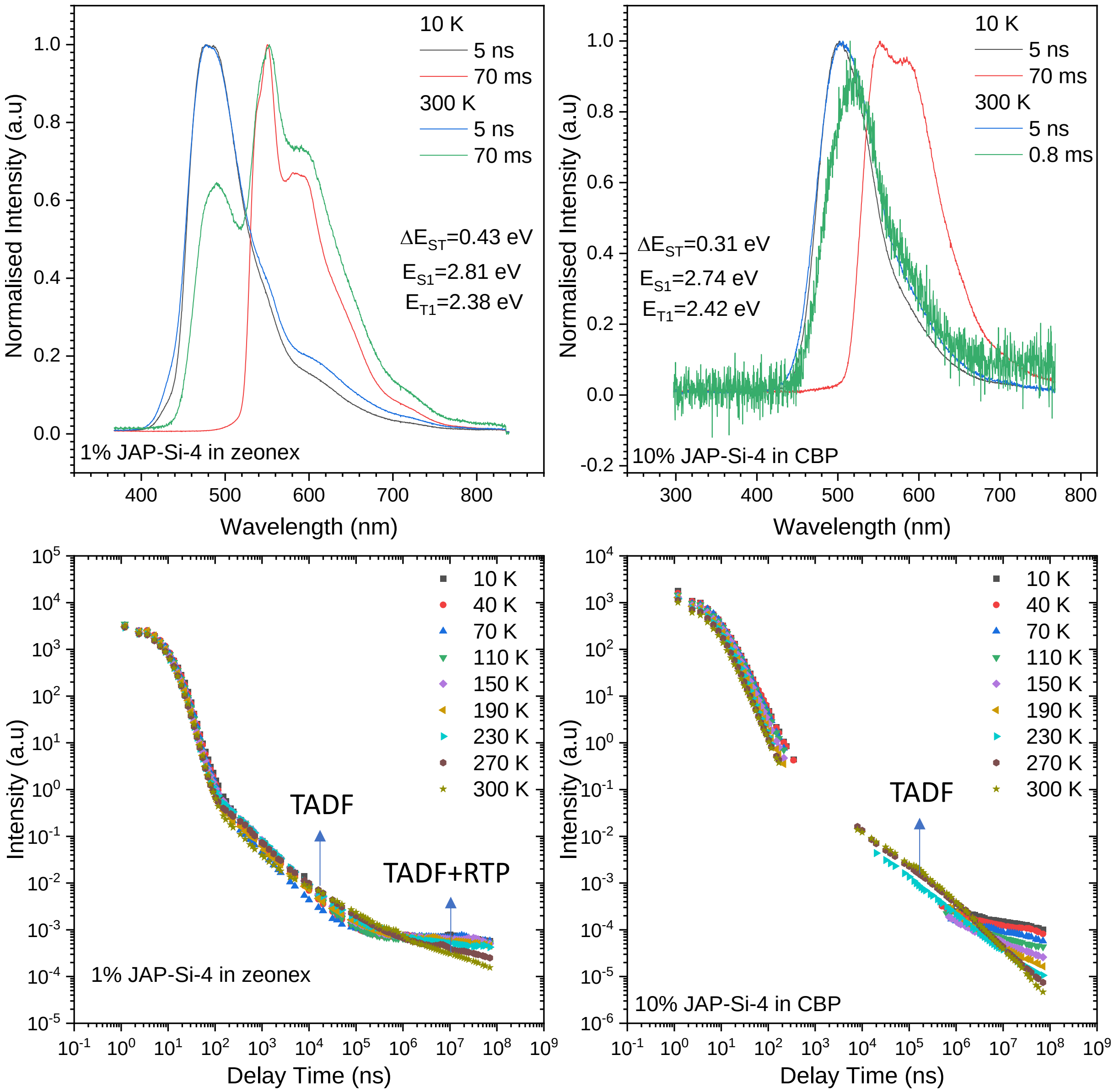

Figure 76. Time-resolved spectra of compound **JAP-Si-4** in different matrices obtained using an iCCD camera. The energies corresponding to the emission onsets. a) 1 % in Zeonex and b) 10 % in CBP.

For **JAP-Si-1** with 2,12 substitution, the results are shown in **Figure 77**. This compound presents a different behaviour than the other two presented so far, showing in Zeonex, **Figure 77a**, a purely TADF emission with a lower ΔE_{ST} (0.16 eV) when compared with **JAP-Si-5** and **JAP-Si-4**. This is a result of a closer location of the donors producing a more crowded structure. The behaviour is similar in the CBP matrix, **Figure 77b**, with a pure TADF emission and no RTP but with higher ΔE_{ST}.

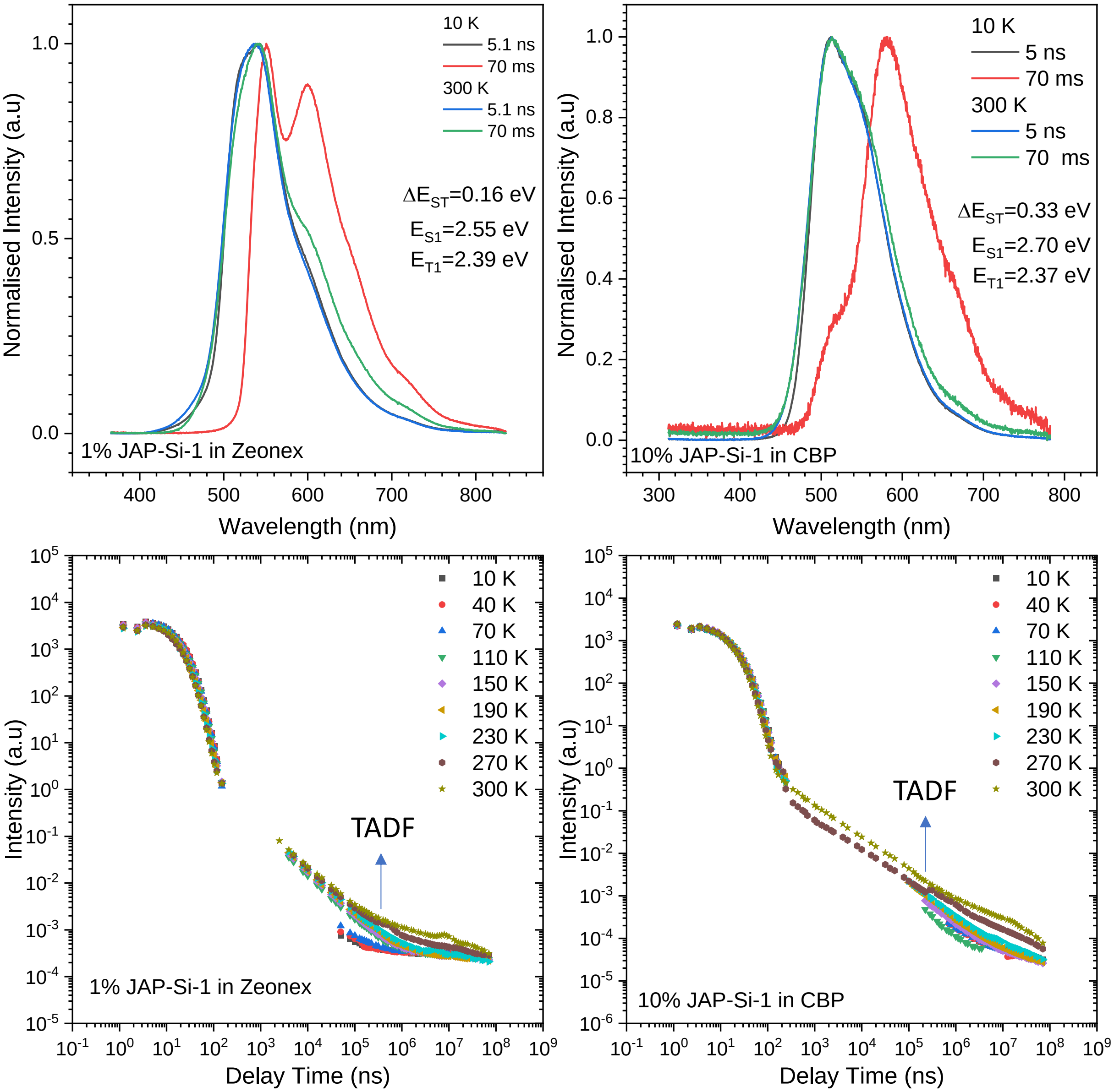

Figure 77. Time-resolved spectra of compound **JAP-Si-1** in different matrices obtained using an iCCD camera. The energies corresponding to the emission onsets. a) 1% in Zeonex and b) 10% in CBP.

The results for compound **JAP-Si-2** are presented in **Figure 78**. The properties of this compound are similar with those observed for **JAP-Si-1** showing a purely TADF emission in Zeonex and CBP. Results for compound **JAP-Si-3** are presented in **Figure 79**. The emitter shows a different behaviour to the previously discussed luminophores with RTP emission in both studied matrices. Comparing the results of these three compounds it is possible to observe the influence of the donor on the isomeric structures. One may note that the **JAP-Si-1** is displays shorter DF lifetime in CBP than **JAP-Si-2** but in Zeonex the relation is opposite.

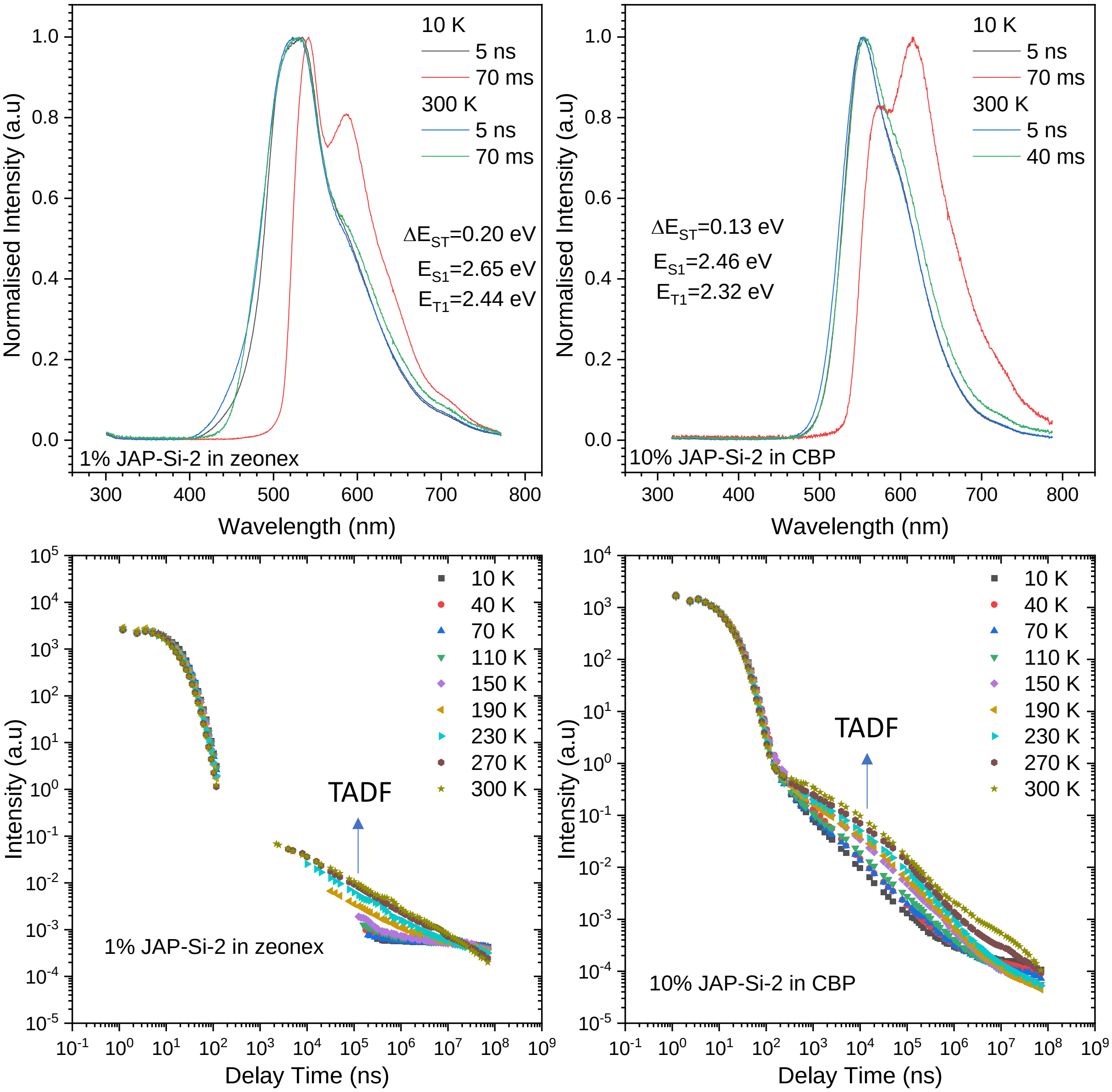

Figure 78. Time-resolved spectra of compound **JAP-Si-2** in different matrices obtained with an iCCD camera. The energies corresponding to the emission onsets. a) 1 % in Zeonex and b) 10 % in CBP.

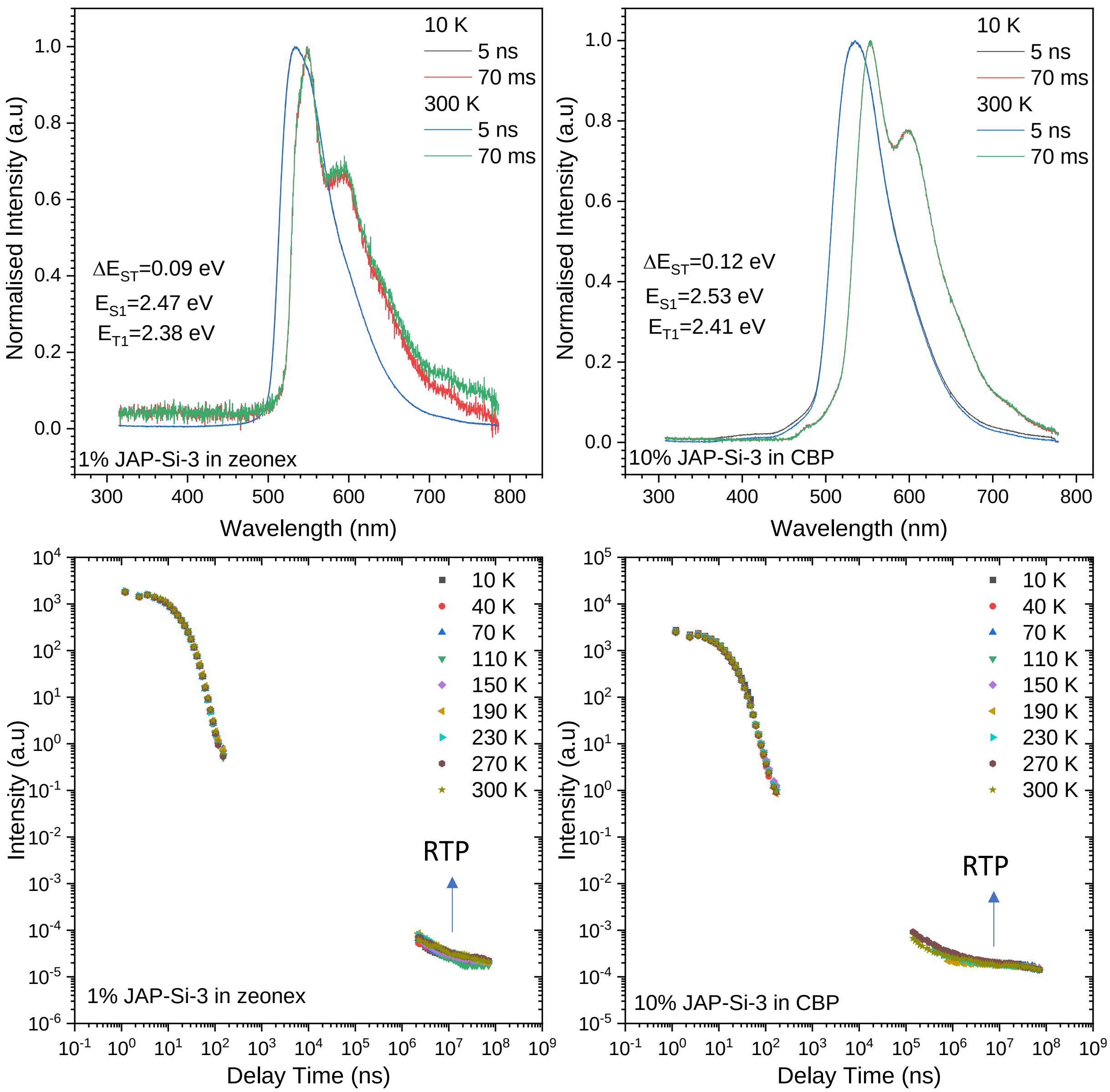

Figure 79. Time-resolved spectra of compound **JAP-Si-3** in different matrices obtained with an iCCD camera. The energies corresponding to the emission onsets. a) 1 % in Zeonex and b) 10 % in CBP

Comparison between **JAP-Si-2** and **JAP-Si-5** as well as **JAP-Si-3** with **JAP-Si-4**, shows that the ΔE_{ST} is visibly smaller for the 2,12 structure. The triplet energies do not significantly differ while the singlet excited state energies reduce by a factor of 0.2 to 0.3 eV in the 2,12 structure. The DF/PF ratio for **JAP-Si-2** in both matrices is lower than in **JAP-Si-5** while for the **JAP-Si-3** it is larger than in **JAP-Si-4** in both matrices. OLEDs of using these compounds were fabricated by our partners, achieving EQE up to 12.6% in CBP for **JAP-Si-5**. More details can be found in the publication.[113]

5.4.4. Conclusions

The effect of differently substituting the acceptor core isomeric effect was successfully studied in this chapter of the thesis. Two substitution patterns were explored with different donors: 2,12 and 3,11. The two possibilities to substitute the dibenzo[a,j]phenazine acceptor have contributed to the development of compounds with different steric hindrance being larger for the 2,12 substitution than for 3,11. This affects directly the photophysical properties of these materials as shown above. The materials presented presenting TADF, TADF+RTP or RTP properties depending on the donor, substitution mode, and matrix. Finally, OLEDs were fabricated giving up to 12.6 % of EQE for the compound **JAP-Si-2**.

6. Conclusions

Throughout this thesis, the primary objective was to establish a relationship between the structural features of compounds and the properties they exhibit. I aimed to demonstrate how even small modifications could result in entirely new properties. In essence, I designed, analyzed, and applied 25 molecules with diverse donor-acceptor structures and various molecular configurations. These molecules included single D-A compounds, D-A-D compounds, and D$_3$-A compounds. In this thesis, I explored numerous relationships, such as comparisons between donors within the same core, the same donor in different cores, donors in the same cores but at different positions, and the influence of minor group modifications. In summary, out of the 25 compounds analysed, 18 displayed TADF properties, 10 showed contributions from conformers in PF and/or DF emission, 4 exhibited TTA and 11 displayed RTP. Moreover, 10 of the compounds demonstrated AIE or AIEE, while 6 were found to be capable of generating SO. It is worth noting that not all compounds were tested for all these properties.

Table 15. Properties of all derivatives presented in this thesis.

Compound	TADF$_1$	TTA	RTP	Conformers	AIE or AIEE	SO
PyBTA-1-DPA	-		X#	-	?	?
PyBTA-2-DPA	-		X#	-	?	?
PyBTA-3-DPA	-		X#	-	?	?
PyBTA-1-PXZ	X		-	-	?	?
PyBTA-2-PXZ	X		-	X	?	?
PyBTA-3-PXZ	X		-	X	?	?
PyBTA-1-PTZ	X		-	X	?	?
PyBTA-2-PTZ	X		-	X	?	?
PyBTA-3-PTZ	X		-	X	?	?
NQPY-PTZ	X		-	X	X	-
NQPY-PXZ	X		-	X#	X	-
NQPY-DMAC	X		-	-	X	X
NQPY-DPAC	X		-	-	X	X
NQPY-DDA	-	X#	X	X	X	X
NQPY-IMD	-	X#	X	X	X	X
NQPY-CBZ	-	X#	X	-	X	X
NQPY-DPA	X#	X#	X	-	X	X
TTT-PTZ	X		-	X	X	?
TTT-PTZ-Me	X#		X#	X	-	?
TTT-CH3-PTZ	X		-	X	X	?
JAP-Si-1	X		-	-	?	?
JAP-Si-2	X		-	-	?	?
JAP-Si-3	-		X	-	?	?
JAP-Si-4	X		X#	-	?	?
JAP-Si-5	X		X#	-	?	?

properties depending on the matrix/solvent.

The **PyBTA** derivatives demonstrated how small changes in the core structure can affect material properties. Using the subtle changes in the position of the methyl group which allowed tuning the TADF properties. Additionally, emission heterogeneity due to the different conformations of **PTZ** and **PXZ** donors was observed. Promising results were achieved for **PTZ** and **PXZ**-containing compounds for use in OLED devices, with **PyBTA-2-PTZ** and **PyBTA-1-PXZ** leading to EQE values of 15.9 % and 14.9 %.

In the case of **NQPy** derivatives, they exhibited multifunctional characteristics, including TADF, TTA, RTP, AIE, and AIEE, depending on the donor. **NQPy-PTZ** and **NQPy-PXZ** compounds displayed conformer contributions to DF emissions in both matrices. The donors such as **DDA**, **IMD**, **CBZ**, and **DPA** in **NQPy** core resulted in TTA contributions and RTP properties. Notably, **NQPy-DPA** demonstrated a mix of TADF and RTP emission in Zeonex. **NQPy-DMAC** and **NQPy-DPAC** had the highest EQE values in this series, reaching 15.9 % and 8.7 %.

TTT acceptor was introduced to study the effect methyl groups introduced in two different parts of the molecule and their influence on the luminescent behaviour, fine tuning the TADF, RTP, and AIE properties. The study demonstrated the ability to switch between RTP and TADF behaviours by selecting suitable host materials and thus controlling ΔE_{ST}. Conformers were observed in **PTZ** donors in all compounds, with the methyl group influencing conformer formation. Notably, **TTT-PTZ** represented the first example of a **TTT**-based emitter with TADF emission, AIEE, and AIDF properties in a single compound. These emitters were used in solution-processed OLEDs, resulting in EQE values of up to 12.4 %.

Finally, the **JAP-Si-X** study successfully examined the regioisomeric effect through donor position changes. Different donors were explored at positions 2,12 and 3,11 of the acceptor, revealing how donor positions affect photoluminescent properties through varying steric hindrance. Position 2,12 exhibited a larger steric hindrance effect and larger torsion angles between the donors and the core compared to position 3,11, directly impacting the photophysical properties of these materials. The compounds displayed TADF, TADF+RTP, or RTP properties depending on the donor, isomer, and matrix. OLEDs were fabricated, with the compound **JAP-Si-2** achieving an EQE of up to 12.6 %.

When comparing the studies, several similarities become evident. For instance, compounds containing **PTZ** and **PXZ** displayed contributions from different conformers, specifically, from eq and ax conformers in their PF and DF emissions. However, in the case of **PyBTA-x-PTZ**, **PyBTA-x-PXZ**, **NQPy-PXZ** and **NQPy-PTZ**, with a single donor moiety they exhibited two possible conformers. In contrast, **TTT** derivatives offered a more complex scenario with 3 donors and numerous conformer possibilities, resulting in intricate decay processes. The influence of matrix polarity in some cases, such as the isomers in **PyBTA-x-PTZ** and **PyBTA-x-PXZ** derivatives, and the presence of methyl groups in **TTT** derivatives, played crucial roles in controlling the distribution of conformers. This effectively constrained the molecule to preferentially form one conformer over the other.

7. References

1 X. Song, J. Liu, T. Zhang and L. Chen, *Sci. China Chem.*, 2020, **63**, 1391–1401.

2 A. D. Scaccabarozzi, A. Basu, F. Aniés, J. Liu, O. Zapata-Arteaga, R. Warren, Y. Firdaus, M. I. Nugraha, Y. Lin, M. Campoy-Quiles, N. Koch, C. Müller, L. Tsetseris, M. Heeney and T. D. Anthopoulos, *Chem. Rev.*, 2022, **122**, 4420–4492.

3 H. Bronstein, C. B. Nielsen, B. C. Schroeder and I. McCulloch, *Nat. Rev. Chem.*, 2020, **4**, 66–77.

4 C. W. Tang and S. A. VanSlyke, *Appl. Phys. Lett.*, 1987, **51**, 913–915.

5 E. L. Hsiang, Z. Yang, Q. Yang, Y. F. Lan and S. T. Wu, *J. Soc. Inf. Disp.*, 2021, **29**, 446–465.

6 F. B. Dias, T. J. Penfold and A. P. Monkman, *Methods Appl. Fluoresc.*, 2017, **5**, 012001.

7 C. W. Tang, S. A. Vanslyke and C. H. Chen, *J. Appl. Phys.*, 1989, **65**, 3610–3616.

8 C. Adachi, T. Tsutsui and S. Saito, *Appl. Phys. Lett.*, 1990, **56**, 799–801.

9 C. J. Zheng, W. M. Zhao, Z. Q. Wang, D. Huang, J. Ye, X. M. Ou, X. H. Zhang, C. S. Lee and S. T. Lee, *J. Mater. Chem.*, 2010, **20**, 1560–1566.

10 P. Data and Y. Takeda, *Chem. - An Asian J.*, 2019, **14**, 1613–1636.

11 C. Chen, R. Huang, A. S. Batsanov, P. Pander, Y.-T. Hsu, Z. Chi, F. B. Dias and M. R. Bryce, *Angew. Chemie*, 2018, **130**, 16645–16649.

12 K. Premasiri and X. P. A. Gao, *J. Phys. Condens. Matter*, 2019, **31**, 193001.

13 K. Klimes, Z. Zhu and J. Li, *Adv. Funct. Mater.*, 2019, **29**, 1903068.

14 K. H. Kim, C. K. Moon, J. H. Lee, S. Y. Kim and J. J. Kim, *Adv. Mater.*, 2014, **26**, 3844–3847.

15 M. A. Baldo, S. Lamansky, P. E. Burrows, M. E. Thompson and S. R. Forrest, *Appl. Phys. Lett.*, 1999, **75**, 4–6.

16 S. Lamansky, P. Djurovich, D. Murphy, F. Abdel-Razzaq, H. E. Lee, C. Adachi, P. E. Burrows, S. R. Forrest and M. E. Thompson, *J. Am. Chem. Soc.*, 2001, **123**,

4304–4312.

17 C. Adachi, M. A. Baldo, M. E. Thompson and S. R. Forrest, *J. Appl. Phys.*, 2001, **90**, 5048–5051.

18 X. Yang, H. Guo, B. Liu, J. Zhao, G. Zhou, Z. Wu and W. Y. Wong, *Adv. Sci.*, 2018, **5**, 1–7.

19 H. Shin, Y. H. Ha, H. G. Kim, R. Kim, S. K. Kwon, Y. H. Kim and J. J. Kim, *Adv. Mater.*, 2019, **31**, 1–6.

20 C. Ou, Y. C. Qiu, C. Cao, H. Zhang, J. Qin, Z. L. Tu, J. Shi and Z. G. Wu, *Inorg. Chem. Front.*, 2022, **10**, 1018–1026.

21 M. Cocchi, J. Kalinowski, D. Virgili and J. A. G. Williams, *Appl. Phys. Lett.*, 2008, **92**, 113302.

22 K. Tuong Ly, R.-W. Chen-Cheng, H.-W. Lin, Y.-J. Shiau, S.-H. Liu, P.-T. Chou, C.-S. Tsao, Y.-C. Huang and Y. Chi, *Nat. Photonics*, 2017, **11**, 63–68.

23 P. K. Chow, G. Cheng, G. S. M. T. Ong, W. P. To, W. L. Kwong, C. C. Kowk, C. Ma and C. M. Che, *Angew. Chemie - Int. Ed.*, 2015, **54**, 2084–2089.

24 T. Fleetham, G. Li, L. Wen and J. Li, *Adv. Mater.*, 2014, **26**, 7116–7121.

25 L. Wang, J. Miao, Y. Zhang, C. Wu, H. Huang, X. Wang and C. Yang, *Adv. Mater.*, 2023, **35**, 1–5.

26 M. Hashimoto, S. Igawa, M. Yashima, I. Kawata, M. Hoshino and M. Osawa, *J. Am. Chem. Soc.*, 2011, **133**, 10348–10351.

27 N. Kandasamy, N. Keerthi and J. Jeyasekaran, *ACS Appl. Electron. Mater.*, 2023, **5**, 4805–4815.

28 H. Nakanotani, Y. Tsuchiya and C. Adachi, *Chem. Lett.*, 2021, **50**, 938–948.

29 A. Endo, K. Sato, K. Yoshimura, T. Kai, A. Kawada, H. Miyazaki and C. Adachi, *Appl. Phys. Lett.*, 2011, **98**, 2–5.

30 C. L. Yi, C. Y. Lin, Y. Tang, C. Y. Wang, C. W. Huang, X. Gong, S. Gong, C. C. Wu and K. T. Wong, *Adv. Opt. Mater.*, , DOI:10.1002/adom.202101791.

31 H. Uoyama, K. Goushi, K. Shizu, H. Nomura and C. Adachi, *Nature*, 2012, **492**, 234–238.

32 T. L. Wu, M. J. Huang, C. C. Lin, P. Y. Huang, T. Y. Chou, R. W. Chen-Cheng, H. W. Lin, R. S. Liu and C. H. Cheng, *Nat. Photonics*, 2018, **12**, 235–240.

33 W. Zeng, H. Y. Lai, W. K. Lee, M. Jiao, Y. J. Shiu, C. Zhong, S. Gong, T. Zhou, G. Xie, M. Sarma, K. T. Wong, C. C. Wu and C. Yang, *Adv. Mater.*, 2018, **30**, 1–8.

34 W. L. Tsai, M. H. Huang, W. K. Lee, Y. J. Hsu, K. C. Pan, Y. H. Huang, H. C. Ting, M. Sarma, Y. Y. Ho, H. C. Hu, C. C. Chen, M. T. Lee, K. T. Wong and C. C. Wu, *Chem. Commun.*, 2015, **51**, 13662–13665.

35 T. A. Lin, T. Chatterjee, W. L. Tsai, W. K. Lee, M. J. Wu, M. Jiao, K. C. Pan, C. L. Yi, C. L. Chung, K. T. Wong and C. C. Wu, *Adv. Mater.*, 2016, **28**, 6976–6983.

36 J. Jayakumar, T.-L. Wu, M.-J. Huang, P.-Y. Huang, T.-Y. Chou, H.-W. Lin and C.-H. Cheng, *ACS Appl. Mater. Interfaces*, 2019, **11**, 21042–21048.

37 W. Derkowski, D. Kumar, T. Gryber, J. Wagner, M. Morawiak, M. A. Kochman, A. Kubas, P. Data and M. Lindner, *Chem. Commun.*, 2023, **59**, 2815–2818.

38 H. Xie, Z. Huang, N. Li, T. Hua, J. Miao and C. Yang, *J. Mater. Chem. C*, 2022, **10**, 11239–11245.

39 T. Kasahara, S. Matsunami, T. Edura, R. Ishimatsu, J. Oshima, M. Tsuwaki, T. Imato, S. Shoji, C. Adachi and J. Mizuno, *Sensors Actuators, A Phys.*, 2014, **214**, 225–229.

40 S. Negi, P. Mittal and B. Kumar, *Microsyst. Technol.*, 2018, **24**, 4981–4989.

41 J. S. Kang, T. R. Hong, H. J. Kim, Y. H. Son, R. Lampande, B. Y. Kang, C. Lee, J. K. Bin, B. S. Lee, J. H. Yang, J. Kim, S. Park, M. J. Cho, J. H. Kwon and D. H. Choi, *J. Mater. Chem. C*, 2016, **4**, 4512–4520.

42 S. Schott, E. R. McNellis, C. B. Nielsen, H. Y. Chen, S. Watanabe, H. Tanaka, I. McCulloch, K. Takimiya, J. Sinova and H. Sirringhaus, *Nat. Commun.*, 2017, **8**, 1–10.

43 X. Zhang, D. Wang, Y. Lei, M. Liu, Z. Cai, H. Wu, G. Shen, X. Huang and Y. Dong,

Chem. Commun., 2022, **58**, 1179–1182.

44 Q. Jia, X. Yan, B. Wang, J. Li, W. Xu, Z. Shen, C. Bo, Y. Li and L. Chen, *Nat. Commun.*, 2023, **14**, 4164.

45 P. She, Y. Yu, Y. Qin, Y. Zhang, F. Li, Y. Ma, S. Liu, W. Huang and Q. Zhao, *Adv. Opt. Mater.*, 2020, **8**, 1901437.

46 W. Zhao, Z. He and B. Z. Tang, *Nat. Rev. Mater.*, 2020, **5**, 869–885.

47 H. Wu, Y. Z. Shi, K. Wang, J. Yu and X. H. Zhang, *Phys. Chem. Chem. Phys.*, 2022, **25**, 2729–2741.

48 S. K. Pathak, G. Li, C. Zhou, Z. Wang and H. Liu, *J. Mater. Chem. C*, 2023, **11**, 6685–6694.

49 P. K. Samanta, D. Kim, V. Coropceanu and J. L. Brédas, *J. Am. Chem. Soc.*, 2017, **139**, 4042–4051.

50 B. Li, Z. Li, Q. Xia, X. Song, D. Chen, F. Guo, S. Gao, Y. Wang and Y. Zhang, *J. Mater. Chem. C*, 2022, **10**, 16064–16069.

51 X. Tang, C. A. M. Senevirathne, T. Matsushima, A. S. D. Sandanayaka and C. Adachi, *Adv. Mater.*, 2023, **202211873**, 1–25.

52 Y. Z. Shi, H. Wu, K. Wang, J. Yu, X. M. Ou and X. H. Zhang, *Chem. Sci.*, 2022, **13**, 3625–3651.

53 B. T. Lim, S. Okajima, A. K. Chandra and E. C. Lim, *Chem. Phys. Lett.*, 1981, **79**, 22–27.

54 P. Jiang, J. Miao, X. Cao, H. Xia, K. Pan, T. Hua, X. Lv, Z. Huang, Y. Zou and C. Yang, *Adv. Mater.*, 2022, **34**, 1–7.

55 A. Sidat, F. J. Hernández, L. Stojanović, A. J. Misquitta and R. Crespo-Otero, *Phys. Chem. Chem. Phys.*, 2022, **24**, 29437–29450.

56 J. Eng and T. J. Penfold, *Commun. Chem.*, 2021, **4**, 21–24.

57 X. K. Chen, D. Kim and J. L. Brédas, *Acc. Chem. Res.*, 2018, **51**, 2215–2224.

58 T. Cardeynaels, S. Paredis, A. Danos, D. Vanderzande, A. P. Monkman, B.

Champagne and W. Maes, *Dye. Pigment.*, 2021, **186**, 109022.

59 X. Cai, X. Li, G. Xie, Z. He, K. Gao, K. Liu, D. Chen, Y. Cao and S. J. Su, *Chem. Sci.*, 2016, **7**, 4264–4275.

60 F. B. Dias, *Philos. Trans. R. Soc. A Math. Phys. Eng. Sci.*, 2015, **373**, 20140447.

61 Y. Long, M. Mamada, C. Li, P. L. Dos Santos, M. Colella, A. Danos, C. Adachi and A. Monkman, *J. Phys. Chem. Lett.*, 2020, **11**, 3305–3312.

62 P. Tinnefeld, J. Hofkens, D. P. Herten, S. Masuo, T. Vosch, M. Cotlet, S. Habuchi, K. Müllen, F. C. De Schryver and M. Sauer, *ChemPhysChem*, 2004, **5**, 1786–1790.

63 I. G. Scheblykin, A. Yartsev, T. Pullerits, V. Gulbinas and V. Sundström, *J. Phys. Chem. B*, 2007, **111**, 6303–6321.

64 R. Schmidt, C. Tanielian, R. Dunsbach and C. Wolff, *J. Photochem. Photobiol. A Chem.*, 1994, **79**, 11–17.

65 R. Motyka, K. Nastula, P. Pander, D. Honisz, M. Tomczyk, K. Erfurt and A. Blacha-Grzechnik, *Materials (Basel).*, 2023, **16**, 2605.

66 T. Goya, P. Zimmermann Crocomo, T. Hosono, S. Minakata, L. E. de Sousa, P. de Silva, P. Data and Y. Takeda, *Asian J. Org. Chem.*, 2022, **11**, 1–7.

67 B. Sk, S. Sharma, A. James, S. Kundu and A. Patra, *J. Mater. Chem. C*, 2020, **8**, 12943–12950.

68 A. Casey, S. D. Dimitrov, P. Shakya-Tuladhar, Z. Fei, M. Nguyen, Y. Han, T. D. Anthopoulos, J. R. Durrant and M. Heeney, *Chem. Mater.*, 2016, **28**, 5110–5120.

69 H. Tanaka, K. Shizu, H. Nakanotani and C. Adachi, *J. Phys. Chem. C*, 2014, **118**, 15985–15994.

70 R. S. Nobuyasu, J. S. Ward, J. Gibson, B. A. Laidlaw, Z. Ren, P. Data, A. S. Batsanov, T. J. Penfold, M. R. Bryce and F. B. Dias, *J. Mater. Chem. C*, 2019, **7**, 6672–6684.

71 M. Okazaki, Y. Takeda, P. Data, P. Pander, H. Higginbotham, A. P. Monkman and S. Minakata, *Chem. Sci.*, 2017, **8**, 2677–2686.

72 M. Gao, Y. Tian, J. Yang, X. Li, M. Fang and Z. Li, *J. Mater. Chem. C*, 2021, **9**, 15375–15380.

73 W. de Pontes Silva, N. Oliveira Decarli, L. Espindola, K. Erfurt, A. Blacha-Grzechnik, P. H. Pander, M. Lapkowski and P. Data, *J. Mater. Chem. C*, 2023, **1**, 3777.

74 J. S. Ward, R. S. Nobuyasu, M. A. Fox, A. S. Batsanov, J. Santos, F. B. Dias and M. R. Bryce, *J. Org. Chem.*, 2018, **83**, 14431–14442.

75 K. Wang, C. J. Zheng, W. Liu, K. Liang, Y. Z. Shi, S. L. Tao, C. S. Lee, X. M. Ou and X. H. Zhang, *Adv. Mater.*, 2017, **29**, 1–9.

76 M. M. Islam, Z. Hu, Q. Wang, C. Redshaw and X. Feng, *Mater. Chem. Front.*, 2019, **3**, 762–781.

77 X. Chen, L. Kong, J. A. A. Mehrez, C. Fan, W. Quan, Y. Zhang, M. Zeng, J. Yang, N. Hu, Y. Su, H. Wei and Z. Yang, *Nano-Micro Lett.*, 2023, **15**, 1–16.

78 S. Kothavale, W. J. Chung and J. Y. Lee, *J. Mater. Chem. C*, 2020, **8**, 7059–7066.

79 J.-X. Chen, K. Wang, C.-J. Zheng, M. Zhang, Y.-Z. Shi, S.-L. Tao, H. Lin, W. Liu, W.-W. Tao, X.-M. Ou and X.-H. Zhang, *Adv. Sci.*, 2018, **5**, 1800436.

80 G. Hong, C. Si, A. K. Gupta, C. Bizzarri, M. Nieger, I. D. W. Samuel, E. Zysman-Colman and S. Bräse, *J. Mater. Chem. C*, 2022, **10**, 4757–4766.

81 J. X. Chen, W. W. Tao, Y. F. Xiao, K. Wang, M. Zhang, X. C. Fan, W. C. Chen, J. Yu, S. Li, F. X. Geng, X. H. Zhang and C. S. Lee, *ACS Appl. Mater. Interfaces*, 2019, **11**, 29086–29093.

82 M. Urban, P. H. Marek-Urban, K. Durka, S. Luliński, P. Pander and A. P. Monkman, *Angew. Chemie Int. Ed.*, 2023, **62**, e202217530.

83 P. Data, P. Pander, M. Okazaki, Y. Takeda, S. Minakata and A. P. Monkman, *Angew. Chemie - Int. Ed.*, 2016, **55**, 5739–5744.

84 A. Klimash, P. Pander, W. T. Klooster, S. J. Coles, P. Data, F. B. Dias and P. J. Skabara, *J. Mater. Chem. C*, 2018, **6**, 10557–10568.

85 A. Maggiore, Y. Qu, R. Guillot, P. Pander, M. Vasylieva, P. Data, F. B. Dias, P. Audebert, G. Clavier and F. Miomandre, *J. Phys. Chem. B*, 2022, **126**, 2740–2753.

86 M. K. Etherington, F. Franchello, J. Gibson, T. Northey, J. Santos, J. S. Ward, H. F. Higginbotham, P. Data, A. Kurowska, P. L. Dos Santos, D. R. Graves, A. S. Batsanov, F. B. Dias, M. R. Bryce, T. J. Penfold and A. P. Monkman, *Nat. Commun.*, 2017, **8**, 14987.

87 J. Zhang, M. Zhu, Y. Lu, X. Zhang, S. Xiao, H. Lan and T. Yi, *Chem. – A Eur. J.*, 2022, **28**, e202200458.

88 S. Xiang, R. Guo, Z. Huang, X. Lv, S. Sun, H. Chen, Q. Zhang and L. Wang, *Dye. Pigment.*, 2019, **170**, 107636.

89 I. Marghad, F. Bencheikh, C. Wang, S. Manolikakes, A. Rérat, C. Gosmini, D. H. Kim, J.-C. Ribierre and C. Adachi, *RSC Adv.*, 2019, **9**, 4336–4343.

90 Y. Hong, J. W. Y. Lam and B. Z. Tang, *Chem. Commun.*, 2009, 4332.

91 M. Cekaviciute, A. Petrauskaite, S. Nasiri, J. Simokaitiene, D. Volyniuk, G. Sych, R. Budreckiene and J. V. Grazulevicius, *Molecules*, 2020, **25**, 445.

92 D. Zhang, X. Xu, X. Huang, Z. Shi, Z. Wang, Z. Liu, R. Hu, J. Liu and M. Zhu, *J. Mater. Chem. A*, 2020, **8**, 18043–18054.

93 F. Paquin, J. Rivnay, A. Salleo, N. Stingelin and C. Silva, *J. Mater. Chem. C*, 2015, **3**, 10715–10722.

94 P. Pander, A. Swist, R. Turczyn, S. Pouget, D. Djurado, A. Lazauskas, R. Pashazadeh, J. V. Grazulevicius, R. Motyka, A. Klimash, P. J. Skabara, P. Data, J. Soloducho and F. B. Dias, *J. Phys. Chem. C*, 2018, **122**, 24958–24966.

95 Y. Liu, W. Hou, L. Xia, C. Cui, S. Wan, Y. Jiang, Y. Yang, Q. Wu, L. Qiu and W. Tan, *Chem. Sci.*, 2018, **9**, 7505–7509.

96 L. G. Franca, P. L. dos Santos, P. Pander, M. G. B. Cabral, R. Cristiano, T. Cazati, A. P. Monkman, H. Bock and J. Eccher, *ACS Appl. Electron. Mater.*, 2022, **4**, 3486–3494.

97 F. B. Dias, K. N. Bourdakos, V. Jankus, K. C. Moss, K. T. Kamtekar, V. Bhalla, J.

Santos, M. R. Bryce and A. P. Monkman, *Adv. Mater.*, 2013, **25**, 3707–3714.

98 V. Gold, Ed., *The IUPAC Compendium of Chemical Terminology*, International Union of Pure and Applied Chemistry (IUPAC), Research Triangle Park, NC, 2019.

99 P. Pander, A. V. Zaytsev, A. Sil, J. A. G. Williams, P.-H. Lanoe, V. N. Kozhevnikov and F. B. Dias, *J. Mater. Chem. C*, 2021, **9**, 10276–10287.

100 P. Pander, A. Swist, R. Motyka, J. Soloducho, F. B. Dias and P. Data, *J. Mater. Chem. C*, 2018, **6**, 5434–5443.

101 G. R. Suman, M. Pandey and A. S. J. Chakravarthy, *Mater. Chem. Front.*, 2021, **5**, 1541–1584.

102 J. Wang, Y. Yang, C. Yao, J. Zhang, P. Xu and X. Xi, *J. Lumin.*, 2023, **259**, 119829.

103 Y. Wu, F. Ni, Z. Chen, W. Yang, Y. Xiang, S. Gong, X. Cao and C. Yang, *Adv. Opt. Mater.*, 2023, **11**, 2300186.

104 B. Huang, W. C. Chen, Z. Li, J. Zhang, W. Zhao, Y. Feng, B. Z. Tang and C. S. Lee, *Angew. Chemie - Int. Ed.*, 2018, **57**, 12473–12477.

105 S. Zeng, C. Xiao, J. Zhou, Q. Dong, Q. Li, J. Lim, H. Ma, J. Y. Lee, W. Zhu and Y. Wang, *Adv. Funct. Mater.*, 2022, **32**, 2113183.

106 Z. Fang, S. Wang, J. Liao, X. Chen, Y. Zhu, W. Zhu and Y. Wang, *J. Mater. Chem. C*, 2022, **10**, 4837–4844.

107 S. K. Pathak, Y. Xiang, M. Huang, T. Huang, X. Cao, H. Liu, G. Xie and C. Yang, *RSC Adv.*, 2020, **10**, 15523–15529.

108 F. Hundemer, E. Crovini, Y. Wada, H. Kaji, S. Bräse and E. Zysman-Colman, *Mater. Adv.*, 2020, **1**, 2862–2871.

109 H. Marchi Luciano, G. Farias, C. M. Salla, L. G. Franca, S. Kuila, A. P. Monkman, F. Durola, I. H. Bechtold, H. Bock and H. Gallardo, *Chem. – A Eur. J.*, 2023, **29**, e202203800.

110 T. Chatterjee and K. T. Wong, *Adv. Opt. Mater.*, 2019, **7**, 1–34.

111 Q. Wei, Z. Ge and B. Voit, *Macromol. Rapid Commun.*, 2019, **40**, 1–19.

112 Z. Zhou, X. Xie, Z. Sun, X. Wang, Z. An and W. Huang, *J. Mater. Chem. C*, 2023, **11**, 3143–3161.

113 T. Hosono, N. O. Decarli, P. Z. Crocomo, T. Goya, L. E. de Sousa, N. Tohnai, S. Minakata, P. de Silva, P. Data and Y. Takeda, *J. Mater. Chem. C*, 2022, **10**, 4905–4913.

114 Y. Takeda, T. Kaihara, M. Okazaki, H. Higginbotham, P. Data, N. Tohnai and S. Minakata, *Chem. Commun.*, 2018, **54**, 6847–6850.

115 N. A. Kukhta and M. R. Bryce, *Mater. Horizons*, 2021, **8**, 33–55.

116 D. Thakur, M. R. Nagar, A. Tomar, D. K. Dubey, S. Kumar, S. S. Swayamprabha, S. Banik, J. H. Jou and S. Ghosh, *ACS Appl. Electron. Mater.*, 2021, **3**, 2317–2332.

117 L. Zhan, Z. Chen, S. Gong, Y. Xiang, F. Ni, X. Zeng, G. Xie and C. Yang, *Angew. Chemie*, 2019, **131**, 17815–17819.